University of Science and Technology of China

Hefei, CHINA

Measurements of high-p_T identified hadron spectra in p+p and Au+Au collisions at RHIC

A dissertation submitted

for the degree of

Doctor of Philosophy in Physics

by

Yichun Xu

Co-supervisors: Ziping Zhang, Zhangbu Xu

2009

Dedicated to my dear family

谨献给我亲爱的父母

摘要

相对论重离子碰撞物理研究至今，人们相信一种新的物质形态（夸克胶子等离子体）可以在相对论重离子碰撞中产生。高横动量喷注碎裂的压低是重要特征之一。在高横动量区域，强子主要由高横动量喷注碎裂产生。微扰量子色动力学的模型预言：高能部分子穿越夸克胶子等离子介质会损失能量，也就是喷注淬灭现象。这一特点为探测夸克胶子等离子体的特性提供了极好的途径：测量喷注淬灭效应相关的高横动量强子。RHIC 上的两个实验， STAR 和 PHENIX，通过核修正因子(R_{AA})的测量都已经观察到了重离子碰撞中强子产额相对于质子质子碰撞产额有所压低。此外，依赖于色动力学的色荷因子的能量损失使得胶子比夸克丢失的能量更多。这会引起（反）质子产额的压低比 pion 和 kaon 产额的压低都要大。然而，我们从 STAR 实验观测到： pion 和质子产额在比较大的误差有着相似的压低，而这似乎与模型预期是相反的。喷注色味转变机制(jet conversion) 试图解释这一现象。在喷注色味转变机制中，喷注中的部分子和夸克胶子等离子体中热化的部分子强烈作用，例如： d,u→s or u,d→g ，使得出射粒子的味道转变。基于此假设，在 $p_T > 5$ GeV/c, $R_{AA}(K)$ 的预期值大约是0.4。

为了进一步研究喷注组分的演变和喷注色味转换现象，我们不但需要核核碰撞中的各种强子谱的测量，而且需要质子质子碰撞中相应的谱。质子质子碰撞中的强子产额可以为高横动量区域的高阶微扰量子色动力学计算提供很好的检验。基于微扰量子色动力学的模型，单举过程中每个强子的产额都可以由部分子分布函数，部分子相互作用，以及碎裂函数共同描述。然而，对于可鉴别的强子谱的碎裂函数， e^+e^- 和其他实验未能很好地限制他们的参数。质子质子碰撞中的强子谱的测量可以为这些部分子碎裂模型提供更好的限制，并且提高他们参数的准确性。因此，质子质碰撞中的粒子产额的测量是至关重要的，并且可以作为金金碰撞中的参考。

本论文工作在数据分析方面有两个技术性的创新：1）重新刻度时间投影室的能量损失，进而改善强子的鉴别; 2）把 BEMC 当作带电强子触发器去获取携带高横动量强子的事例。这些方法不仅适用于 STAR 探测器, 也可为LHC上的实验和其他实验提供一个很好的方法。本论文还把 200GeV 质子质子碰撞中的 $\pi^{\pm}$, $K^{\pm,0}$, p 和 $\bar{p}$ 不变截面

测量扩展到p_T = 15GeV/c。一些高阶的微扰量子色动力学计算很好地描述π的横动量谱，比如：Albino-Kniehl-Kramer (AKK) 和DeFlorian-Sassot-Stratmann (DSS) 计算。然而，他们却不能够描述我们高横动量区域的$p(\overline{p})$ 和$K^{\pm}$ 谱。基于质子质子碰撞中测量的扩展，金金碰撞中核修正因子的测量也能够延伸到更高的横动量区域。因此本论文也做了金金中心碰撞中的$R_{AA}(\pi^{\pm})$, $R_{AA}(K^{\pm})$, $R_{AA}(p,\overline{p})$, 并且与$R_{AA}(\rho)$作比较。我们的结果显示$R_{AA}(\pi) \sim R_{AA}(\rho)$，这表明轻夸克之间是没有质量效应的。相反地，$R_{AA}(p)$和$R_{AA}(K)$ 测量值系统地高于$R_{AA}(\pi)$。这些特性和喷注色味转换机制的预言相符合。在本论文中，我们还把测量结果与其他一些模型进行比较，并讨论将来的RHIC 和LHC上更精确的测量和喷注化学成分的研究。

关键词： 夸克胶子等离子体, 电离能损, 核修正因子, Jet转换。

ABSTRACT

Many exciting signals from RHIC experiments have indicated the existence of the new matter created in heavy ion collisions, through jet suppression at high p_T *etc.*. All pQCD models predict that energetic partons lose energy when traversing a QGP medium: the jet quenching phenomenon. The effect is experimentally observable through hadrons at high transverse momentum from jet fragmentation. This offers an excellent tool to probe the QGP properties by measuring the outgoing high-p_T hadrons associated with the jet quenching effect. Both STAR and PHENIX Collaborations at RHIC have observed a suppression of hadron production at high p_T in central heavy ion collisions. The result was obtained using the nuclear modification factor (R_{AA}), which is the hadron yield at high p_T in central Au+Au collisions divided by that in p+p collisions properly scaled by the underlying number of the nucleon-nucleon binary collisions. Furthermore, the energy loss is expected to depend on the QCD color charge factor: gluons lose more energy than quarks. The consequence of this mechanism is that the suppression for antiprotons and protons is expected to be more severe than the pions and kaons. However, we observed similar suppression for pion and proton with large uncertainties from STAR, which is contrast to model expectation. A jet conversion mechanism was proposed, in which the incident jet parton interacts violently with a thermal parton in the QGP matter and consequently produces an outgoing energetic parton with different flavor (*i.e.* d,u→s or u,d→g). Based on the jet conversion, $R_{AA}(K)$ are predicted to be ~ 0.4 at $p_T > 5.0$ GeV/c.

To further study the evolution of jet chemistry and the jet conversion phenomenon, we need identified hadron spectra in nucleus-nucleus collisions as well as in p+p collisions. The identified hadron production in p+p collisions also provides a good test to Next-to-Leading Order (NLO) perturbative-QCD (pQCD) calculations at high p_T range. In the framework of models based on pQCD, the inclusive production of single hadron is described by the convolution of parton distribution functions (PDFs), parton interaction

cross-sections and fragmentation functions (FFs). However, the flavor-separated fragmentation functions of identified hadrons at high Z are not well constrained by the e^+e^- and other experiments. These measurements of identified hadron at high p_T in p+p collisions can also provide better constraint on the parton fragmentation model and improve the precisions of their parameters.

In this thesis, two new techniques are developed to improve the hadron identification by re-calibrating the Time Projection Chamber (TPC) measured dE/dx and to enhance the high-p_T hadron yields in the data set using the Barrel Electromagnetic Calorimeter (BEMC) as trigger detector for the charged hadrons. This new method significantly extend measurements of the identified hadrons cross-section to higher p_T at STAR. These techniques are not only applicable to STAR detector, but also provide an useful tool for experiments at LHC and other facilities. We measured invariant differential cross-sections of charged π, K, p ($\overline{p}$) and neutral kaon up to 15 GeV/c in p + p collisions at $\sqrt{s_{NN}}$ = 200 GeV. The p_T spectra of π can be described by NLO pQCD calculations very well, such as Albino-Kniehl-Kramer (AKK) and DeFlorian-Sassot-Stratmann (DSS) calculations. However, they fail to describe our proton and kaon spectra at high p_T. Based on the high p_T extension of p+p measurements, the nuclear modification factors in Au + Au collisions can also be extended to higher p_T. We present R_{AA} for $\pi^{\pm}$, $K^{\pm}$ and $p(\overline{p})$, compared with ρ measurements in central Au + Au collisions. Our measurements show that $R_{AA}(\pi) \sim R_{AA}(\rho)$, which indicates that there is no mass effect on light hadrons from quark fragmentations. On the contrary, the R_{AA} of $\bar{p}$ (p) and kaons are systematically above that of pions. These features are qualitatively consistent with a jet conversion picture. In this thesis, we also compare the results to other models, and discuss future measurements with improved precisions and further jet chemistry study at RHIC and LHC.

Key word: quark-gluon plasma, nuclear modification factor (R_{AA}), jet conversion

Table of Contents

List of Figures

List of Tables

CHAPTER 1

Introductions: Physics and experimental measurements

People realize the nature by two directions. One is the way to macro world by kinds of telescopes, the other is to search micro matter by microscopes, through developing systems for micro particles, accelerators and detectors. The ultimate goal of high energy physics is to explore the fundamental particles and discover the universal rules for describing nature and our universe.

There are four forces in the nature: Gravity, electro-magnetic, weak and strong forces. To unify these forces together using a simple rule, people must know each of them very well first. For strong force between quarks and gluons, Quantum Chromodynamics (QCD) is a basic gauge field theory to describe their strong interactions. In Lattice QCD (LQCD) calculations, a phase transition from hadronic phase to a de-confined quark and gluons, Quark-Gluon-Plasma (QGP), is predicted to exist under in the condition of high temperature and high net baryon density. The QGP is also believed to exist in the early stage of universe formation, a few micro seconds after big bang. Therefore, exploration for the QGP is fundamental to nuclear physics, and helpful to reveal the source of our universe.

In this chapter, we introduce the fundamental components of the prevalent theories, predictions and corresponding observable measurements that can provide good test and constraints to current theory.

1.1 Quantum ChromoDynamics

1.1.1 QCD running coupling constant and asymptotic freedom

The gauge theory, Quantum Electro-Dynamics (QED) describes the electro-magnetic interactions by photons successfully. The effective coupling between electrons is given by following functions.

$$\alpha_{QED}(Q^2) = \frac{\alpha_0}{1 - (\alpha_0/\pi) ln(Q^2/m_e^2)}, \tag{1.1}$$

where m_e is the electron mass and Q is the momentum transfer between the two electrons. At large distances the value of the effective coupling is small due to the effect of charge screening and reaches its asymptotical value of $\alpha_0 = \frac{1}{137}$.

Similarly, the QCD [FG72] is introduced by Gell-Mann and Fritzschto to describe the strong forces among quarks through the mediator, gluons. Different from photon, gluon carries color by itself, and has eight active gluon states ($3^2 - 1 = 8$, where 1 is the color-singlet). Therefore, it not only couples between quarks, but also couples to other gluons. Experimentally, lifetime for $\Sigma^0(1192) \to \Lambda\gamma$ and $\Sigma^0(1385) \to \Lambda\pi^0$ are measured to be $\sim 10^{-19}$s and $\sim 10^{-23}$s, respectively, and then the coupling of strong interactions is estimated $\sim$100 larger than the electro-magnetic interactions, by $\frac{\alpha_s}{\alpha_{QED}} \sim \frac{\sqrt{10^{-19}}}{\sqrt{10^{-23}}} \sim 100$, where $\alpha_{QED} = e^2/4\pi \sim 1/137$, and $\alpha_s = g_s^2/4\pi \sim 1$. Here, g_s is defined as the strong charge of the constituent quarks. This is why we call it strong interaction. The QCD coupling is given by:

$$\alpha_s(Q^2) = \frac{4\pi}{\beta_0 \times ln(\mu^2/\Lambda_{QCD}^2)} \tag{1.2}$$

, where $\beta_0 = (11 - \frac{2}{3}n_f)$ is a constant dependent on the number of quarks flavors (n_f), and Λ_{QCD} is an important perturbative scale variable which has to be determined experimentally, and now is assumed to be around 200 MeV. When $\mu = \Lambda_{QCD}$, or equivalently at large distances, the effective coupling becomes infinite, the theory is un-calculable. On the other hand, at very large values of μ^2, or small distances, the coupling tends to zero and quarks appear to move freely. In this case, QCD can be calculated perturbatively. This unique phenomena of the strong force between quarks and gluons at large

distances and asymptotic freedom at short distance are the two remarkable features of QCD, called *asymptotic freedom*, discovered by Gross, Politzer and Wilczek in 1973, who were awarded with the Nobel price at 2004. According to the behavior of short distance and large distance, the static QCD potential can be described as:

$$V_s = -\frac{4}{3} \times \frac{\alpha_s}{r} + k \times r, \tag{1.3}$$

where the first term dominating at small, arises from single-gluon exchange, similar to the Coulomb potential between two charges in QED, while the second term is presumably linked with the confinement of quarks and gluons inside hadrons. Fig. 1.1 shows the experimental data and theoretical calculations of the running coupling versus different momentum transfer, μ. [Ams08].

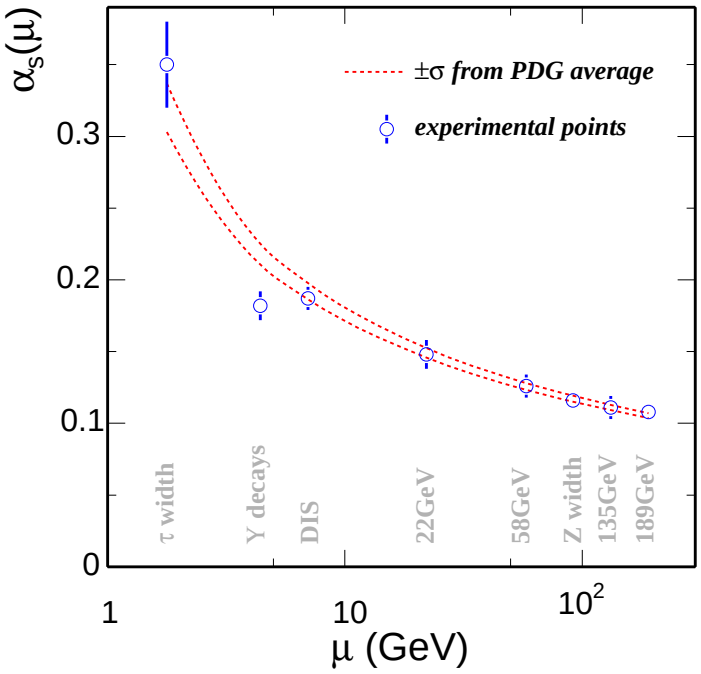

Figure 1.1: Measured QCD running coupling constant α_s from different experiments compared with Lattice QCD calculations.

At low momentum transfer region, $\alpha_s \sim 1$ results in lots of contributions from α_s^2, α_s^3, ...α_s^n. Therefore, *Lattice QCD* [Gup98] is introduced to calculate these interactions. At high momentum transfer, the $\alpha_s \ll 1$, the first order contribute a lot, and high-order

interactions can be neglected, and *perturbative QCD (pQCD)* calculation is introduced to describe single-gluon exchange approximately. With power n = 0, 1, 2..., the calculations are named Leading Order (LO), Next-to-Leading Order, Next-to-Next-to-Leading Order, ... respectively. Due to higher order terms usually have smaller contribution and involves more complicated diagrams, the NLO pQCD calculations are sufficient to describe mostly current experimental data.

1.1.2 Pertubative QCD

pQCD is the efficient way to describe the strong force at larger momentum transfer or short distance between two quarks. Since quarks are un-observable, the final confined status of quarks (hadrons), can be described by the *pQCD*, such as hadrons cross section. (In general, a meson consists of a quark and an anti-quark, while a baryon is constituent of three quarks, and quarks are un-observable in experiments.) These high Q^2 parton interactions, also referred to as hard-scatterings, produce hadron jets with large transverse momentum. The inclusive hadron cross section can be written as a convolution of three independent parts: *parton distribution functions (PDFs)*, parton cross section and *fragmentation functions (FF)* as following.

$$d\sigma(x, Q^2, m^2) = \prod_{h,h'} \sum_{i,f} f_{i/h}(x, \mu^2) \otimes d\hat{\sigma}_{i\to f}(x, Q^2, m^2, \mu_r^2, \mu_F^2) \otimes D_{h'/f}(x, \mu^2) + \mathcal{O}(\Lambda/Q), \tag{1.4}$$

where the factor $f_{i/h}$ stands for the *PDFs* of the parton i inside the hadron h present in the initial state, and x represents the fraction momentum within the incoming hadron. The parton distributions depend on the factorization/renormalization scale μ^2. The second factor $d\hat{\sigma}_{i\to f}$, also known as the (Wilson) coefficient function, represents the partonic hard scattering cross section for the reaction $i \to f$ that depends on the un-physical re-normalization and factorization scales μ_r^2 and μ_F^2, the masses of the quarks m^2 and momentum transfer Q^2. The last factor D is the so called *FFs*. It contains the information

for the hadronization of the hard parton f (that is produced in the hard process described by the partonic cross-section $d\hat{\sigma}$) into an observed hadron h'. Both the PDF's and the FF are non-perturbative objects and thus have to be determined experimentally. Since the concepts of parton distributions and hadronization are only for the initial and final states of hadrons, lepton-nucleon *Deep Inelastic Scattering* (DIS) and high energy e^+e^- collisions are performed to measure *PDFs* and *FFs*, respectively.

1.1.3 Lattice QCD and phase transition in LQCD

LQCD as a non-pQCD approach is a popular way to study strong force at low momentum transfer or large distance. In Lattice QCD, space-time is separated as crystalline lattices. Vertices of lattice occupied by quarks, and gluons can only travel along lines between vertices. As the lattice is sufficiently small ($\rightarrow 0$), the space-time are presented continuous approximately, then the LQCD approach continuum QCD. Due to limits of computation, LQCD calculations often involved analysis at different lattice spacing to determine the lattice-spacing dependence, which can then be extrapolated to the continuum (lattice spacing $\rightarrow 0$). This technique is only applicable in the domain of low density and high temperature. At higher densities, the fermion sign problem renders the results useless.

QCD phase transition in LQCD Quarks are un-observable, and confined by color force as hadrons, meson and baryon. Under extreme conditions of high temperature or high net baryon density, energy density is high enough, then the force among quarks and gluons may be greatly reduced. Therefore, quarks and gluons are de-confined or thermalized from hadrons to the QGP matter.

The phase transition from the confined hadronic matter to the de-confined QGP matter results in a rapid increase in entropy density, which increases new (color) degrees of freedom at T_c, in energy density and pressure and leads to a consequent change in the equation of state (EOS). In the limit where the de-confined quarks and gluons are non-interacting, and the quarks are massless, the Stefan-Boltzmann pressure P_{SB} of this

partonic state, as a function of temperature T at zero chemical potential (*i.e.*, zero net quark density), would be simply determined by the number of degrees of freedom [Ada05a]:

$$\frac{P_{SB}}{T^4} = [2(N_c^2 - 1) + \frac{7}{2} N_c N_f] \frac{\pi^2}{90} \tag{1.5}$$

, where N_c is the number of colors, N_f is the number of quark flavors, the temperature is measured in energy units. The two terms on the right in Eq. 1.5 represent the gluon and quark contributions, respectively. With the constraint of computing cost, LQCD calculations for pressure are shown on the Fig. 1.2. There are some features of the LQCD calculations: critical temperature of this phase transition, $T_c \sim$ 150 - 180 MeV; the energy density at the critical point is $\epsilon_c(T_c)$ $\sim$1 - 3 GeV/fm^3 ($\sim$ 0.17 GeV/fm^3 for nuclear matter) [Kar02a, Kar02b]; The pressure divided by T^4 rises rapidly above T_c, then begins to saturate by about $2T_c$. The nature of the transition from hadronic to QGP phase is highly sensitive to the number of dynamic quarks flavors and quark masses, as shown on the Fig. 1.2 [FP00], 2 flavors (massless u and d), 3 flavors (massless u, d and s), and 2+1 flavors with strangeness mass. All values are substantially below the Stefan-Boltzmann (SB) limits shown as arrows on the Fig. 1.2. The deviation from SB limit indicates substantial remaining interactions among the quarks and gluons in the QGP phase. Therefore, various heavy ion experiments are designed to create the new phase matter, and explore its features.

1.1.4 De-confinement and experiments in laboratory

Hadrons can be melted into the QGP matter with sufficiently high temperature or baryon density. The phase transition from hadron gas to the de-confined QGP can be described in Fig. 1.3 [Das09].

To create this new kind of matter in laboratory and explore its novel properties, a large amount of energy needs to be packed into a limited space volume by colliding heavy ions. The heavy ion collisions have been proposed as a more effective way, because the initial energy density increases as a power law function with the atomic number while only

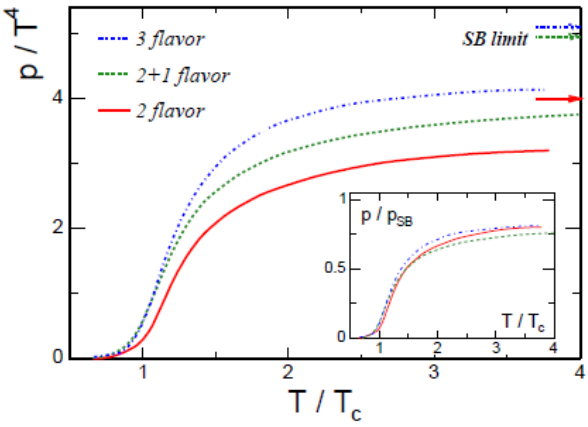

Figure 1.2: The evolution of p/T^4 with the increase of temperature T for 3 different flavor configurations. The arrows indicate the SB limits for each case. The insert panel shows the ratio of p/p_{SB} with function of T [FP00]

.

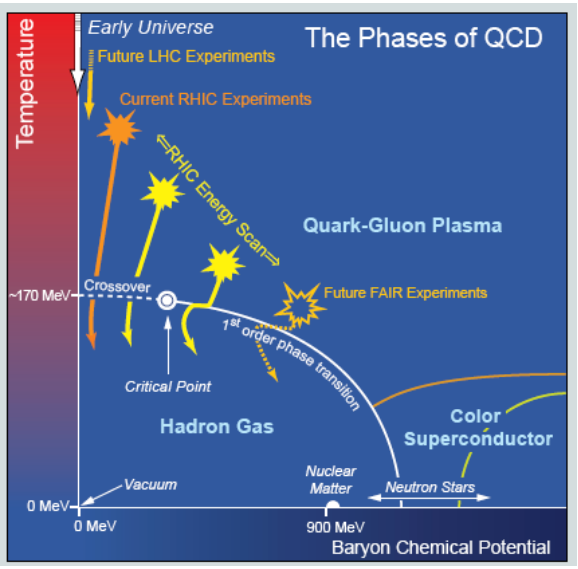

Figure 1.3: Phase diagram of hadronic and partonic matter [Das09]

logarithmically with collision energy [Don]. Therefore, physicists have been making efforts on heavy ion colliders to explore and cross the phase transition boundary in laboratory, since the 1970' s, from BEVALAC at LBL, SIS at GSI, AGS at BNL, SPS at CERN, RHIC at BNL and the coming LHC at CERN, etc [Sto04].

1.2 Relativistic Heavy Ion Collider (RHIC)

Relativistic Heavy Ion Collider (RHIC) at Brookhaven National Laboratory (BNL) was built to create new phase matter by colliding heavy ions. It has successfully run in past eight years, and performed various ion collisions at different energy for our physics goals, such as Au + Au collisions at $\sqrt{s_{\rm NN}}$ = 62, 130 and 200 GeV, Cu + Cu collisions at $\sqrt{s_{\rm NN}}$ = 62 and 200 GeV, d + Au and p + p collisions at 200 GeV, and some test runs for low energy collisions, *i.e.* Au + Au at 9.2 and 19.6 GeV and Cu + Cu collisions at 22 GeV. From these runs, plenty of exciting physics results reveal that the matter created at RHIC is quite different from what we observed before: It cannot be described by hadronic degrees of freedom and demonstrates many of the signatures from a QGP scenario. These measurements provide strong hints for the discovery of QGP [al02], and some of the key measurements will be discussed in the following sections.

1.2.1 Heavy ion collisions

With sufficiently high temperature or net baryon density, energy density is high enough in a bulk system to form the new QGP matter. Fig. 1.4 shows the space-time evolution of a heavy ion collision. In this 2-dimensional sketch, time flows from bottom to top and the spatial expansion is on the x-axis. About 1 fm/c after the beams collision, the QGP is formed, and the QCD system begin to expand, due to high energy density and pressure gradients accompanying cool-down. At this time, energy density of the system is estimated $\sim$ 1 GeV/fm^3 by the Bjorken [Bjo83]. At $T_c \sim$ 170 MeV, the critical temperature, the phase transition to a hadron gas is believed to occur, then at the chemical freeze-out temperature (T_{ch}), the in-elastic collisions stop, and chemical

composition cease to change. Finally, at T_{fo} or thermal/kinetic freeze-out temperature, the elastic scattering will stop, and momentum distribution of the particles are fixed. We have tried to determine appropriate observations to measure each one of these stages and study the properties of the QGP in a heavy ion collision. From past runs, a large amount of evidence for the existence of QGP have been obtained, although the final proof remains open [Ada05a] and more direct signature need to be found out. In following text, we would discuss some observations from previous runs.

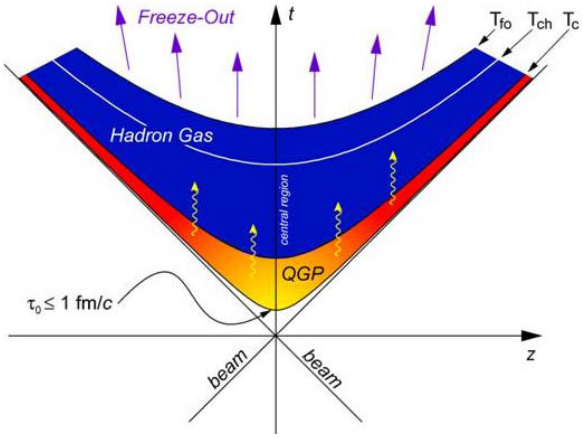

Figure 1.4: Space-time evolution of a heavy ion collision, assuming the formation of QGP.

Definition of centralities is introduced first, because it is believed that central heavy ion collisions more possibly create the new phase of matter, due to high density of partons between head-on ions and sufficient interactions of the partons. The two relativistic heavy ions can be taken as two thin disks in laboratory, due to the lorentz contraction in the moving direction. The impact parameter (b), is the distance between the perpendicular bisectors along the colliding direction of the two ions. When $b \rightarrow 0$, a central collision happens, while a peripheral collision occurs at $b \rightarrow$ radius of ion. In experiments, we do not know the real b value, then the Glauber Model related to the b, is used to simulate the produced particle multiplicities distribution, and gives people variables of centrality. Fig. 1.5 shows multiplicity density distributions of measured charged particles in the TPC within $|\eta| < 0.5$ in Au + Au collisions at 62.4 and 200 GeV, respectively [Abe09]. Nine centrality bins are shown, 0 - 5%, 5 - 10%, 10 - 20%, 20 - 30%, 30 - 40%, 40 - 50%, 50

- 60%, 60 - 70%, and 70 - 80%, and corresponding to the fraction of the measured total cross section from central to peripheral collisions. The 80 - 100% centrality is usually not used in STAR analysis because of its significant trigger bias due to vertex inefficiency at low multiplicities and the contamination from electromagnetic interactions.

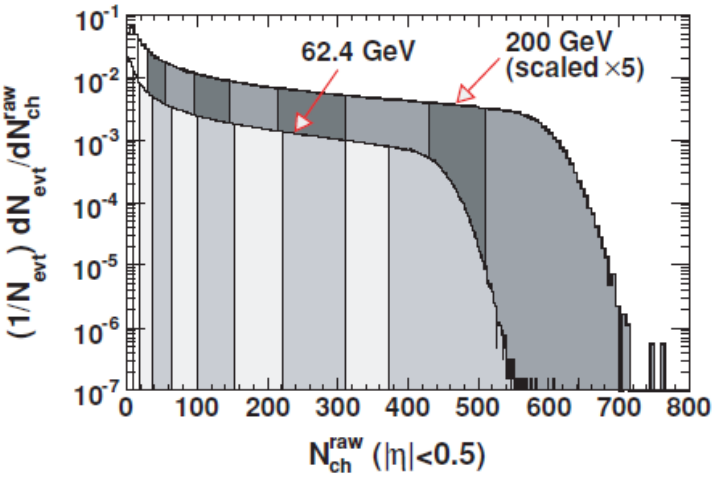

Figure 1.5: Definition of centralities for Au+Au collisions at $\sqrt{s_{\rm NN}}$= 62.4 and 200 GeV.

Hadronic spectra and Collective motion If the QGP system is created in an instant after collision, and then expanded and cooled down, final state hadrons suffer different effect at different stage. Therefore, studying hadron spectra is an unique way to explore properties of the bulk system, and specific particles can be used to probe different stages after heavy ion collisions. For example, hadron productions are measured and compared to some statistical models, which have successfully described particles production in different collisions systems, such as $e^+ + e^-$, p + p and nuclear collisions [FR01, PS99]. The models assume that all hadrons originate from a hadron gas fireball in full thermal equilibrium, and then decouple from the fireball at a given freeze-out temperature T_{ch}. After decoupling there are no more in-elastic interactions between the particles and the hadron abundances are fixed. Some models allow for partial chemical equilibrium of the system in introducing an additional free parameter γ_s, which is the non-equilibrium parameter for strange sector [Hei].

Fig. 1.6 shows comparison of particle ratios from statistical model fits (short lines)

and STAR measurements (circles) of integrated hadron yeilds ratios at low p_T for central Au + Au collisions. The fits are excellently consistent with ratios on the left side of the Fig. 1.6, with $T_{ch} = 163 \pm 4\ MeV$, $\mu_B = 24 \pm 4\ MeV$, $\gamma_s = 0.99 \pm 0.07$ [JA04, Bar04]. However, some short-lived resonances, $\Lambda^\star$ and $K^\star$ near the right side of the Fig. 1.6 deviate from the statistic model fits, presumably due to hadronic re-scattering after the chemical freeze-out. The inset of the Fig. 1.6 shows variation of γ_s with centrality, from ~ 0.75 in peripheral Au+Au collisions to $\sim$ unit for central Au+Au collisions.

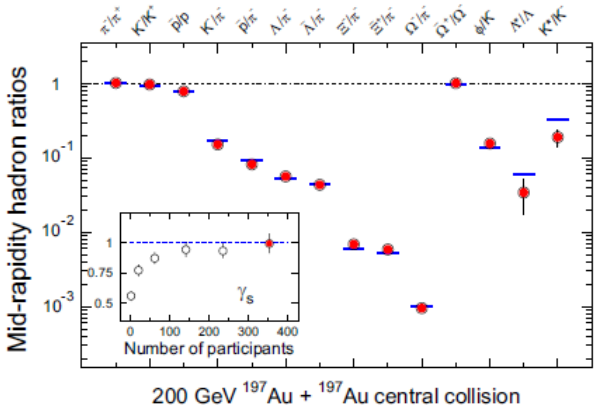

Figure 1.6: Ratios of p_T-integrated mid-rapidity yields for different hadron species measured in STAR for central Au+Au collisions at 200 GeV. The horizontal bars represent statistical model fits to the measured yield ratios for stable and long-lived hadrons. The inset shows γ_s versus multiplicities in Au+Au collisions, compared with results in p+p collisions (leftmost point) [Ada05a].

The characteristics of the bulk system at *kinetic freeze-out*, can be explored by analysis of the transverse momentum distributions for various hadron species. For example, STAR measured spectra for identified particles [al04a, al04b, al05, al04c] were fit by the Boltzmann-Gibbs Blast Wave model (BGBW) [SSH93] with a compact set of parameters of temperature (T), flow velocity (β), and flow profile (ρ) [Ada05a, SSH93]. With the BGBW model applied to the data in a limited p_T range (≤ 1 GeV/c) where the equilibrium is believed to reach, the results show a negative correlation between the T and β, *i.e* β raises from smaller value ~ 0.2 in p+p collisions and ~ 0.3 in peripheral collisions to large $\beta \sim 0.6$ in central collisions, while the temperature decrease from peripheral to central collisions [Ada05a]. The observed parameters are contrast to zero velocity in p+p colli-

sions from theoretical expectation [STA], because of the strong assumption of equilibrium system in BGBW and arbitrary fit range in p_T for the fit quality. Beside, it treats p+p, peripheral Au+Au, central Au+Au system with same heat bath at fixed temperature. This is also contrast to observed change of particle spectra slope from peripheral (power-law, Levy) to central (exponential) in Au+Au collisions [Adl02b, Ada05b, Ada05d, Abe07b].

The non-extensive Tsallis statistics, dealing with complex systems in condensed matter successfully, have been utilized to understand the particle production in high energy and nuclear physics [DBS07, WW09, ALQ00]. Therefore, the Tsallis is embedded in blast wave model instead of Boltzmann distribution for source of particle emission, describing hydrodynamic expansion in heavy ion collisions, *i.e. Tsallis Blast Wave model (TBW).* In the TBW model, three parameters are common for all particles: temperature T, non-equilibrium parameter q, and maximum flow velocity $\beta_s = \beta(1 + n/2)$, where n = 1 and average flow velocity β is bounded to the range [0, 0.7] [Abe09] to aid in fit convergence and avoid non-physical results. The Tsallis distribution behaviors as a power-law function at high p_T and an exponential distribution at low p_T, and becomes the familiar Boltzmann distribution, when $q \to 1$.

Fig. 1.7 shows fitting results for identified particles [Adl02b, Ada05b, Abe07b] in central (0 - 10%) and peripheral (60 - 80%) centralities as solid-lines, compared with BGBW model fit as dash-lines on the left panel. This fits are limited at 3 GeV/c to avoid surface emission at high p_T. $(q-1)$, a measure of the degree of non-equilibrium, decreasing from 0.086 to 0.018, indicates the effects that the fluctuations at initial impact due to Color-Glass Condensate (CGC) formation or individual nucleon-nucleon collision may not be completely washed out by subsequent interactions at either the QGP phase or the hadronic phase [DOP02, MMS08, BRB09]. T, the average temperature of the local source, shows a small increase from 114 to 122 MeV, which is in contrast to the conventional BGBW result, where a decrease of temperature was observed [Abe09]. β, the average flow velocity, increase from zero in peripheral and peripheral Au+Au to $(0.470 \pm 0.009)c$ in central Au+Au collisions. These parameters are shown on the right plot in the Fig. 1.7 by T versus $(q-1)$ and β versus $(q-1)$. Each shaded region represents a one-σ contour from the

error matrix obtained from the TBW fit for a given centrality. The dependence is clearly nonlinear and has a negative correlation, and their correlations are fit with a quadratics and obtain T = (0.123 ± 0.0014) - (1.2 ± 0.4)$(q-1)^2$ and β = (0.49 ± 0.01) - (61 ± 5)$(q-1)^2$, as shown in the figure.

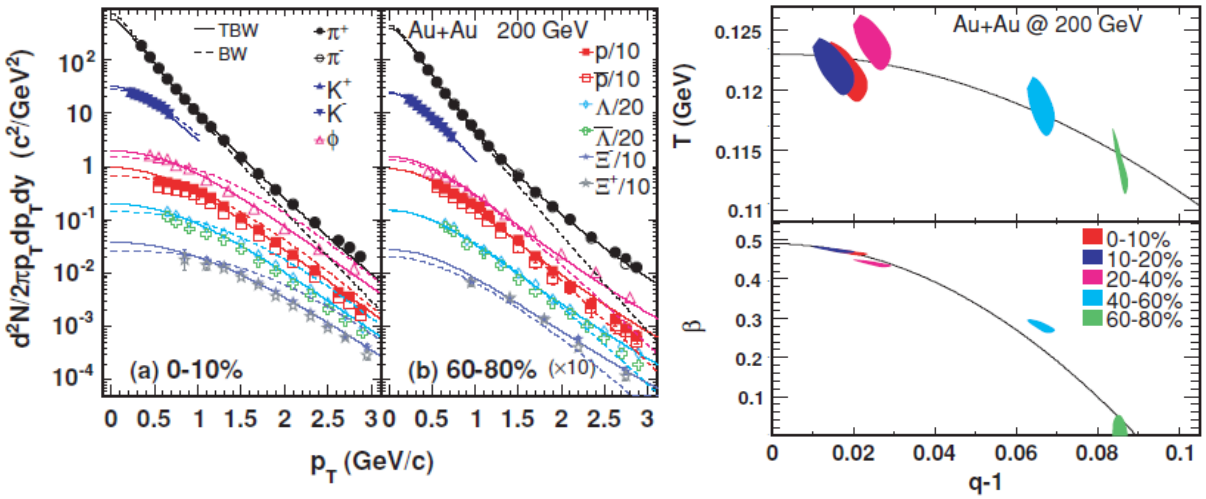

Figure 1.7: On the left panel, identified particle transverse momentum spectra in Au+Au collisions at $\sqrt{s_{\rm NN}}$=200 GeV in 0 - 10% central collisions on panel (a), and in peripheral 60 - 80% collisions (b). The symbols represent experiment data points and solid curves are TBW fit results [Tan09] and dashed lines are BGBW calculations with β and T from [STA]. On the right panel, the fit parameters T and β as a function of $(q-1)$. Each block is one-σ contour from the error matrix of the TBW fit for a given centrality of Au+Au collisions [Tan09].

This fit is also extended to p+p collisions to describe system non-equilibrium. Good fits are shown by separating particles as two groups: mesons and baryons. For example, proton being close to $K^\star$ in mass, shows more similarly shape in spectra to that of kaon. This again verify the characteristic baryon versus meson grouping in p+p data, which has been observed perviously in m_T scaling analysis of the same data [Abe07c].

There are still open discussions about the Tsallis statistics. Firstly, the dependence of T and β on $(q-1)$ is argued to relate to bulk viscosity. If this viscosity is very large at phase transition, a systematic study of TBW model fits may help locate the critical point in the coming Beam Energy Scan at RHIC. Secondly, $(q-1)$ values in p+p collisions at LHC are expected to be larger than those at RHIC because of increased relative contributions of hard and semihard processes. If $(q-1)$ is not larger for LHC p+p collisions and non-zero

flow velocities are observed, the question of thermalization or even quark-gluon plasma in such collisions might be raised, so the results of TBW fits at LHC will certainly be informative.

anisotropic flow In non-central heavy-ion collisions, two nuclei overlap each other when they pass each other. The overlapping region forms an anisotropy in coordinate space, then subsequently leads to an anisotropy in momentum space, due to re-scattering in the system evolution. The dynamic expansion of the system can wash out the coordinate-space-anisotropy, while the momentum-space-anisotropy saturate during the evolution of the system [KH]. The final state particle spectrum in momentum space can be characterized in a Fourier expansion in terms of particle azimuthal ϕ distributions with repect to $(w.r.t)$ the reaction plane Ψ_r, as Eq. 1.6.

$$E\frac{d^3N}{dp^3} = \frac{d^2N}{2\pi p_T dp_T dy}(1 + \sum_{n=1}^{\infty} 2v_n cos[n(\phi - \Psi_r)]), \tag{1.6}$$

$$v_n = \langle cos[n(\phi - \Psi_r)]\rangle, \tag{1.7}$$

where reaction plane (Ψ_r), is defined by the beam direction and the impact parameter. The first and second coefficients, v_1 and v_2 are called the directed and elliptic flow. Due to the approximate elliptic shape of the overlapping region, the elliptic flow, v_2 is the largest harmonic observed in mid-rapidity. Because of the quenching of coordinate-space-anisotropy, elliptic flow can reveal early information about the system. Since it also depends on re-scattering, elliptic flow is sensitive to the degree of thermalization of the system in the early stage.

Fig. 1.8 shows identified particle $v_2(p_T)$ and the hydrodynamic model predictions at low p_T ($p_T < 2$ GeV/c) [Ada05a]. In this low p_T region, v_2 has larger values for lower mass particles. This mass ordering is reasonably described by the hydrodynamic models, which assume ideal relativistic fluid flow and negligible relaxation time compared to the time scale of the equilibrated system. The agreement implies early thermalization, *i.e.* strongly interacting matter with a very short mean free path dominates the early stages

of the collisions.

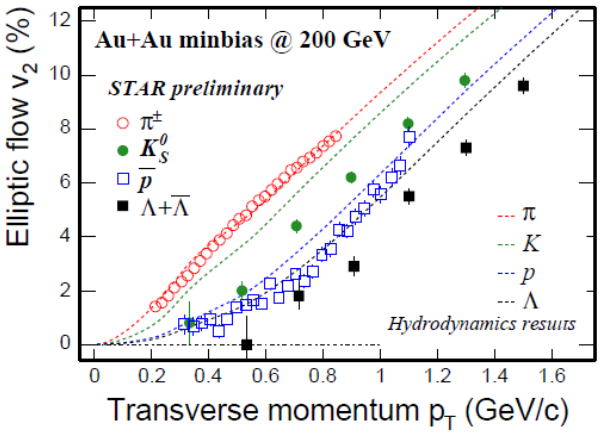

Figure 1.8: Elliptic flow v_2 of identified particles as a function of p_T at low p_T region compared with hydrodynamic model predictions.

Fig. 1.9 shows $v_2(p_T)$ in a larger p_T range for different particles [Adl03b, Ada04b]. v_2 for all particles saturates above a certain p_T ($\sim$ 2 - 3 GeV/c). In addition, particles are separated into two groups on the left plot: mesons and baryons. With the *Number of the Constituent Quarks* (NCQ) for the corresponding hadrons, v_2/n_q versus p_T/n_q for all particles are plotted on the right panel ($n_q = 2$ for meson, and $n_q = 3$ for baryon). At p_T/n_q >0.6GeV/c, all those particles fall onto one universal curve expect pions (due to resonance decay effect [GK04, DES04]. This meson/baryon grouping phenomenon was also observed in the nuclear modification factor R_{cp} at intermediate p_T ($1.5 < p_T <$ 5 GeV/c) [al05, Sor]. Coalescence models [LK02, MV03] which assume hadrons are formed through coalescing of constituent quarks provide a viable explanation for these observations. This indicates that the flow developed during a sub-hadronic (partonic) epoch, offers a strong evidence of de-confinement at RHIC.

Energy loss and jet quenching Another observable is studied to prove existence of the QGP matter created in heavy ion collisions: di-hadron azimuthal correlation. Fig. 1.10 shows the azimuthal distribution of associated hadrons (p_T> 2 GeV/c) relative to a triggered hadron (p_T^{trig} >4 GeV/c). On the near side, $\Delta\phi = 0$ indicates that the enhanced correlation are observed in p+p, d+Au, and Au+Au collisions. This means that one pair

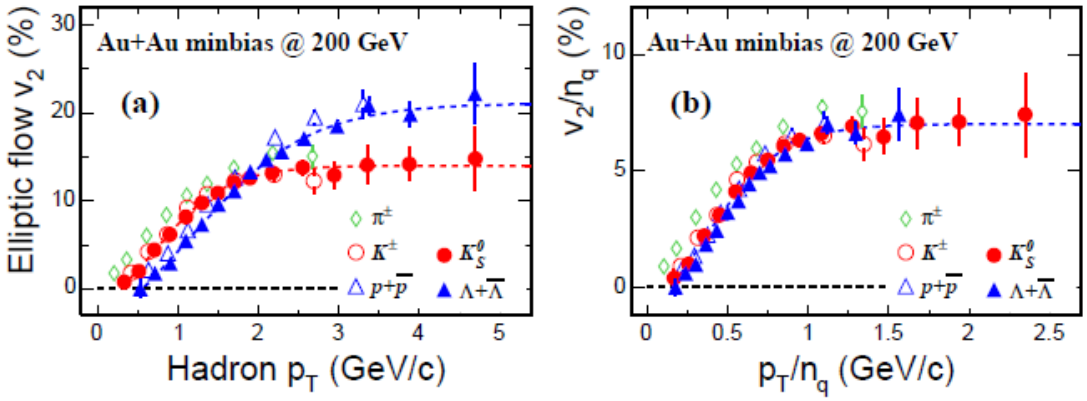

Figure 1.9: Left: Identified particle v2 up to intermediate p_T. Right: After scaling the v2 and $p_T$with number of constituent quarks nq, all particles fall onto one universal curve at p_T/nq $>$ 0.6 GeV/c. [Don]

of these from a single jet. Meanwhile, on the away-side, $\Delta\phi = \pi$, the enhancement of correlation is observed both in p+p collisions and d+Au collision while it almost disappears in central Au+Au collisions. This again suggests that the suppression is due to the final state interaction of hard-scattered partons or their fragmentation production in the dense medium generated in Au+Au collisions [Ada03], if the correlation is indeed the result of jet fragmentation. A more differential probe of partonic energy loss is the measurement of high p_T dihadron correlations relative to the reaction plane orientation. The right panel on the Fig. 1.10 shows a study from STAR of the high p_T dihadron correlation from 20 - 60% centrality Au+Au collisions, with the trigger hadron situated in the azimuthal quadrants centered either in the reaction plane ("in-plane") or orthogonal to it ("out-of-plane") [Ada04a]. The same-side dihadron correlation in both cases is similar to that in p+p collisions. In contrast, the suppression of the back-to-back correlation depends strongly on the relative angle between the trigger hadron and the reaction plane. This systematic dependence is consistent with the picture of partonic energy loss: the path length in medium for a dijet oriented out of the reaction plane is longer than in the reaction plane, leading to correspondingly larger energy loss in the out of plane. The dependence of parton energy loss on path length is predicted [Mik] to be substantially stronger than linear.

The energy lost by away side partons traversing the collisions matter must lead to an

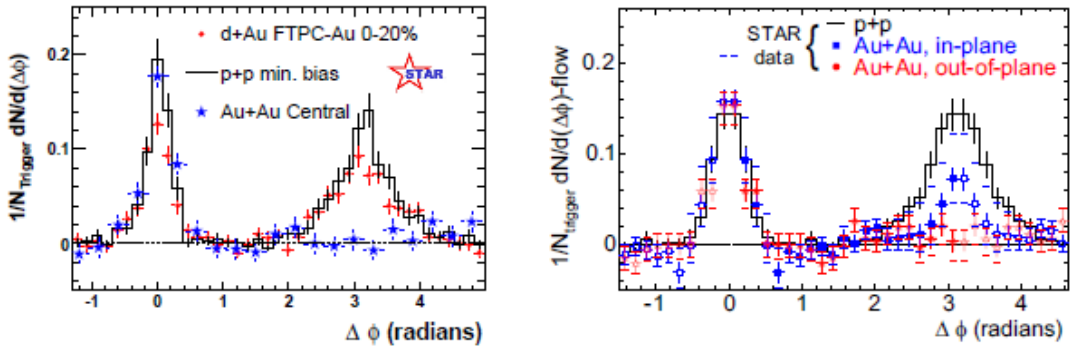

Figure 1.10: Left Panel shows correlations for p+p, central d+Au, and central Au+Au collisions (background subtracted) from STAR [Ada05a]. Right Panel shows the background-subtracted di-hadron correlation for different orientations of the trigger hadron relative to the Au+Au reaction plane.

excess of softer emerging hadrons, due to conserve transverse momentum. In order to study jet degradation in the medium, associated softer particles ($0.15 < p_T < 4$ GeV/c) on away-side are analyzed, relative to different triggered particles ($4 < p_T^{trig} < 6$ GeV/c, $6 < p_T^{trig} < 10$ GeV/c) in different centralities Au+Au collisions. The left plot in Fig. 1.11 shows the centrality dependence of mean p_T ($< p_T >$) of the associated away-side charged hadrons opposite to the high p_T trigger, compared with that of inclusive hadrons. The trends of $< p_T >$ in both trigger are observed to decrease from peripheral to central Au + Au collisions, and two values approach each other within larger uncertainties. These results hint the attainment of thermalization via the frequent soft parton-parton interactions in the early stages. However, how strong those partons interaction is still a crucial open question, that needs to be answered quantitatively to address the evidence of early thermalization of the system.

An independent way is proposed to explore the existence of the QGP, via Nuclear Modification Factor (R_{AA}). It is believed that particles at high p_T (> 5 GeV/c) are mainly produced from the initial QCD hard-scattering processes [Adl02a]. If QGP is created in heavy ion collisions, the final state particles yields can be changed by interacting with the medium, *w.r.t* a reference in p+p collision. In experiments, the R_{AA} is defined as the ratios of particle yields in $A + B$ collisions to those in $p + p$ collisions, scaled by the

number of binary nucleus-nucleus collisions [Adl02a]:

$$R_{AA} = \frac{d^2N_{AB}/dp_T dy}{N_{bin} d^2N_{pp}/dp_T dy}, \tag{1.8}$$

where $\langle N_{bin} \rangle$ is the equivalent number of binary collisions calculated from the Glauber model.

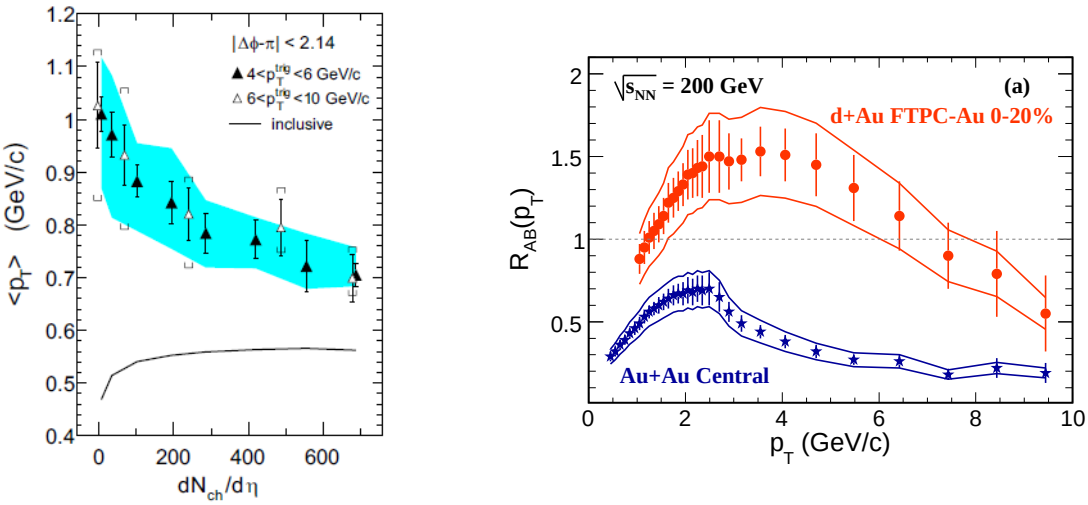

Figure 1.11: Left Panel: Associated charged hadron $< p_T >$ from the away-side in 200 GeV p+p (two leftmost points) and Au+Au collisions at various centralities, in each case opposite a trigger hadron with p_T in 4-6GeV/c (filled triangles) or 6-10 GeV/c (open triangles) range [Wan04]. The shaded band and the horizontal caps represent the systematic uncertainties for the filled and open symbols, respectively. $< p_T >$ for inclusive hadron production in the Au+Au collisions is indicated by the solid curve. Right Panel: $R_{AB}(p_T)$ for minimum bias and central d+Au collisions and central Au+Au collisions. The bands show the normalization uncertainties.

Fig. 1.11 shows the R_{AA} versus p_T for charged hadrons in 0-5% Au+Au collisions and 0-20% d+Au collisions on the right panel. A clear suppression of N_{bin} scaled hadron yields relative to p+p collisions has been observed at high p_T in Au+Au collisions, while disappeared in d+Au collisions. This phenomena indicates that the suppression in Au+Au collisions are not effected by the initial state (such as saturation, nuclear shadowing of the PDF, and initial state multiple scattering and so on), rather by the final state interaction (FSI) of hard scattered partons or their fragmentation products in the dense medium generated in Au+Au collisions [Ars03, Adl03a, Bac03, Ada03]. (The enhancement of R_{dAu} at intermediate p_T range and mid-rapidity is explained by Cronin Effect [al79], which is

attributed to the influence of multiple parton scattering through cold nuclear matter prior to the hard scattering that produces the observed high-p_T hadron [Wan97].) Therefore, R_{AA} is an unique tool to explore the new matter by final state interaction and prove if there is a very dense matter created in central Au+Au collisions at RHIC.

How jet interact with the medium? In order to further understand this, theorist's effort throw light on the explanation step by step. First, *energy loss* is provided to explain it: when a parton jet goes through the medium, it can interact with medium and lose energy through radiation of gluons. Somehow, it can explain the previous suppression of charged hadron. But in QCD framework, the strength of the gluon self coupling, C_F, is 3 and the strength of a gluon coupling to a quark is 4/3. Therefore, the Casimir factor for gluons is 9/4 times that for quarks, which leads to more energy loss in traversing a medium [Wan98] for proton than that for pion. Naively, proton yields are expected to be suppressed more than pion in Au+Au collisions. However, with more statistics, STAR recent measurements shown on the Fig. 1.12 present the similar p/π and $\overline{p}/\pi$ ratios in peripheral and central Au+Au collisions. This phenomena is contrast to the prediction of QCD.

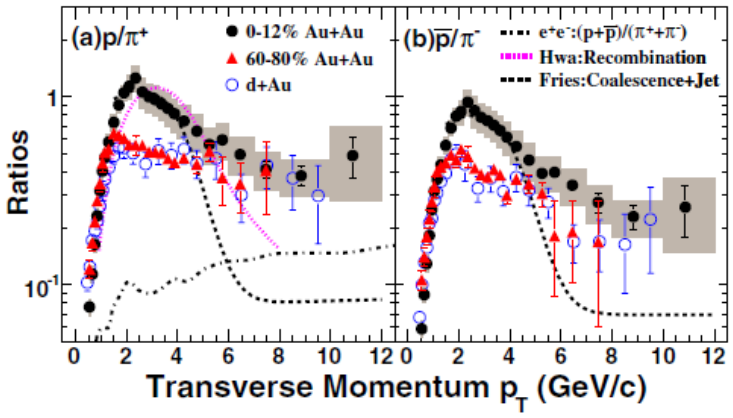

Figure 1.12: The p/π^+ and $\overline{p}/\pi^-$ ratios from d + Au [Ada05e, Ada06b] and Au + Au collision at $\sqrt{s_{\rm NN}}$=200GeV/c [Abe06]. The shaded boxes represent the systematic uncertainties in the top 12% central Au + Au collisions. The systematic uncertainties for 60%-80% Au + Au collisions are similar. The $(p+\overline{p})/(\pi^+ + \pi^-)$ ratio from light quark jets in $e^+ + e^-$ collisions at $\sqrt{s_{\rm NN}}$ = 91.2 GeV is shown as a dotted-dashed line [Abr98]. The dotted and dashed lines are model calculations in central Au + Au collisions [HY04, FMN03].

To solve this problem, another picture of *Jet Conversion* has been developed recently

by theorists [LKZ07, LF08b]. In this physics picture, a jet parton not only loses energy by radiating gluons, but also changes its flavor by interacting with medium, through following two main channels:

$$q + \overline{q} \rightarrow g + g, \tag{1.9}$$

and

$$q(\overline{q}) + g \rightarrow g + q(\overline{q}). \tag{1.10}$$

Based on this idea, R_{AA} for K^0_S is predicted about 0.4 at high p_T with conversion, while it's ~0.2 at high p_T without conversion. With the same conversion factor, the ratio of $R_{AA}(\mathrm{p})/R_{AA}(\pi)$ is about unit at high p_T, compared with ~ 0.6 without this conversion. All these predictions are shown on the Fig. 1.13. Meanwhile, v_2 for u, d and s are calculated with this conversion and corresponding hadrons, such as π^0, K^0_S, proton and Λ at high p_T in [LF08a].

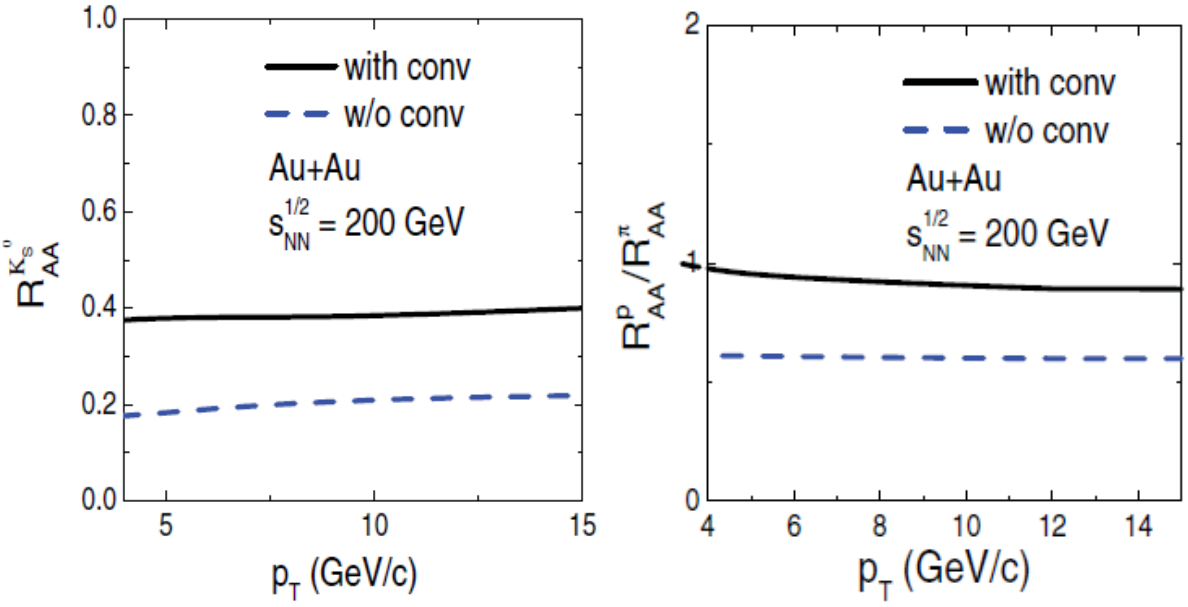

Figure 1.13: Left Panel: R_{AA} for K^0_S versus p_T with and without jet flavor conversions. Right Panel: The ratio of R_{AA} for proton to R_{AA} for pion, with and without jet conversion [LF08b].

In addition, jet hadro-chemistry is brought out for LHC energy [SW08]. In this idea, there are enhanced parton splitting in medium, compared with no medium. Based on this, both K/π and p/π ratios are enhanced with jet in medium, relative to vacuum. In

the future, this theory can be refined by considering flavor and baryon number exchanging between projection and target parton in the medium.

1.2.2 p + p collisions

Although RHIC is designed for heavy ion collisions, it also successfully ran p+p collisions with/without polarization. According to hadronic cross section, elastic and in-elastic collisions are sorted. For in-elastic collisions, there are singly-diffractive, double-diffractive and non-diffractive processes. Diffractive processes are defined as processes where one nucleon acts as a region of absorption and the interference of scattering amplitudes gives rise to diffraction pattern in the forward and backward regions. A nucleon suffering a diffractive scattering becomes excited and then loses a small amount of energy when breaking up into a few particles at a small emission angle. This can occur in one of the nucleons (singly) or in both (doubly). In non-diffractive processes the nucleons hit 'head-on' and both disintegrate creating large particle multiplicities at mid-rapidity. The STAR p+p trigger is only sensitive to the *non-singly diffractive (NSD)* cross-section (σ_{NSD}), since it requires charged tracks to be detected in coincidence on both sides of the interaction point, so about 70% of the inelastic cross-section (σ_{inel}) are measured at STAR.

In p + p collisions, final state particles are generated from the level of fundamental interactions between partons (gluons and quarks), which is governed by QCD. At large momentum transfer (Q^2), perturbative QCD is applicable to solve the first principle, although it's impossible to get an exact solution at low momentum transfer. As mentioned above, particle cross-section can be calculated by the pQCD, and its parameters have been refined by *deep in-elastic scattering* for $e^+ + e^-$ and lepton-nucleon collisions. They have been implemented in computer code to describe or predict some particle cross-sections successfully, such as PYTHIA with CDF tune. The PYTHIA is a event generator based on Monte-Carlo simulations, using JET-SET algorithm developed in the late seventies by the Lund group and successfully applied to e^++e^- data from PETRA and PEP [SS05]. The parton cross-section is approximated by 2 $\rightarrow$2 processes and the associated

LO Feynman diagrams. Parton distribution functions, as well as the fragmentation functions, are non-perturbative objects and cannot be calculated from QCD first principles. They are therefore user-defined from a list of currently available parametrizations. The default hadronization mechanism in PYTHIA is the "Lund symmetric string fragmentation" parametrization [AGI83].

In the framework of models based on QCD, the inclusive production of single hadrons is described by the convolution of parton distribution functions (PDFs), parton interaction cross-sections and fragmentation functions (FFs). With increasing p_T range, there are discrepancies of hadron production between measurements and Leading Order (LO) QCD calculations. In order to complement the calculations, parton processes at higher orders in α_s are included for additional parton cross-sections, *i.e.* NLO calculations. By comparing measurements with QCD calculation, parameters *FFs* can be constrained more stronger and each set of FF can be refined or revised more reasonably. As shown on Fig. 1.14, pion p_T spectra can be described very well by these NLO pQCD calculations, AKK, KKP, and phenomenological parton model (EPOS). However, proton p_T spectra deviate from NLO pQCD predictions at high p_T range. This indicates that data points in p+p collisions could provide more constraints to NLO pQCD calculations.

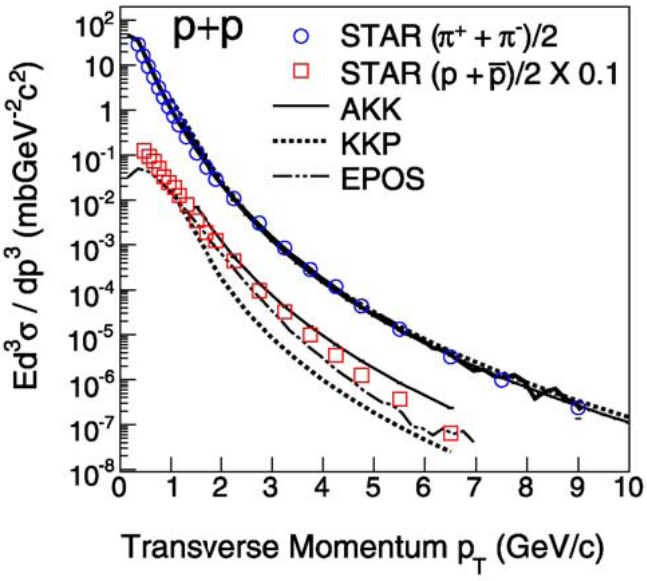

Figure 1.14: Published pion and proton measurements in p + p collisions, and curves are theoretical predictions [Ada06b].

However, those p_T spectra measurements are limited at 10 GeV/c for pion and 7 GeV/c for proton due to current statistics at STAR, so extension of spectra measurement is crucial to test NLO pQCD. In addition, measurements in p + p collisions also provide a ideal baseline to explore QGP created in heavy ion collisions, and Cronin effect in d + Au collisions. In this thesis, study in p + p collisions is the main work, which will be discussed later on. Also, particle identification in Au+Au collisions with our developed method are done to reduce the systematic uncertainties in previous results [Abe06].

1.3 Summary

Why we do this study? As we mentioned above, our goal at RHIC is to explore the new hot and dense phase matter, QGP, created in heavy ion collisions. There are many tools to explore the QGP and study its properties. In this dissertation, I will focus on the measurements of R_{AA} in central Au+Au collisions. In order to extend the measurements to high p_T, where hard processes are dominant, it's crucial to precisely study particle production in p+p collisions as a reference. Therefore, in this thesis, we developed a new calibration method to identify charged particles at high p_T, and unique means to reconstruct high-p_T resonance with triggered daughters using EMC triggered events. These methods allow us measure $\pi^{\pm}$, $K^{\pm}$, p ($\overline{p}$) and K^0_S *etc.* at high p_T precisely. The new calibration method is also applied to Au + Au data to improve the systematic uncertainties of previous measurements of charged hadrons spectra at high p_T in Au+Au collisions [Abe06]. Meanwhile, p+p data provide a good test for the fundamental theory, the pQCD calculations, and constrain parameters for these models.

CHAPTER 2

Experimental Set-up

2.1 RHIC Accelerator Complex

The Relativistic Heavy Ion Collider (RHIC) at Brookhaven National Laboratory (BNL) is constructed to accelerate and collide heavy ions and polarized protons with high luminosity. It started to build from 1991 and began operate in 2000, and have continued development and construction in the following 10 years. RHIC is the first machine in the world to collide heavy ion, which are atoms removed their outer cloud of electrons. The top center-of-mass collision energy is 200 GeV per nucleon pairs, which is more than 10 times greater than the highest energy reached at previous fixed target experiments. The RHIC experiments allow people to study what the universe may have looked like in the first few moments after its creation. This may help us understand more about why the physical world works the way it does, from the smallest subatomic particles to the largest star. In more details, it can give us points to explore new state of hot, dense matter out of the quarks and gluons that are the basic particles of atomic nuclei, as theorist predicted. Besides of heavy ion collisions, polarized proton-proton collisions are delivered at RHIC for exploring the spin puzzle [Ash88, Bas09], that quarks in proton only carry about 20% of the proton's spin. This is contrary to the expectation that the spin of a proton was simply the sum of the spins of its three component quarks. *What account for the missing 80%?* To investigate this question, the RHIC delivered polarized proton beams with center-of-mass energy from 200 GeV to 500 GeV.

The basic design parameters of the collider are list in Tab. 2.1 [HLO03]. The luminosity achieved now is actually much higher than the original design. The store-averaged

luminosity reached now are 12×10^{26} cm^{-2}s^{-1} for Au+Au collisions, 2.3×10^{31} cm^{-2}s^{-1} for p+p collisions and 1.3×10^{29} cm^{-2}s^{-1} for d+Au collisions.

Table 2.1: Performance specifications of RHIC [HLO03]

	For Au+Au	For p+p
Beam energy	100 $\rightarrow$ 30 GeV/nucleon	250 $\rightarrow$ 30 GeV/nucleon
Luminosity	2×10^{26} cm^{-2}s^{-1}	1.4×10^{31} cm^{-2}s^{-1}
Number of Bunches/ring	60 ($\rightarrow$ 120)	60 ($\rightarrow$ 120)
Luminosity lifetime	$\sim$10 hours	$>$ 10 hours

Fig. 2.1 shows a diagram of the RHIC machine complex, including a Van de Graaff facility, a Linear Proton Accelerator, the Booster Synchrotron ring, the Alternative Gradient Synchrotron (AGS) and ultimately the RHIC synchrotron ring. To operate Au beam, the Pulsed Sputter Ion Source are used to create the negatively charged Au ions with charge Q = -1 e. Then they are accelerated through the Van de Graaff facility and stripped of their electrons with a foil at the Tandem's high voltage terminal. At the exit of Tanderm, the kinetic energy and net charge of Au ions reach 1 MeV/nucleon and Q = +32 e respectively. Those ions are then injected into the booster synchrotron and then accelerated to an energy of 95 MeV/nucleon, and stripped further to Q = +77 e at the exit of booster. After acceleration and stripping in the booster, ions are transferred into the AGS, where they are accelerated up to 10.8 GeV/nucleon, which is the RHIC injection energy. The 24 bunched injected into AGS are de-bunched and then re-bunched to four bunches at the injection from porch prior to the acceleration. Finally, the final four bunches are transferred into RHIC bunch by bunch, through the AGS-to-RHIC Beam Transfer Line, and further stripped to the bare charge state of Q = +79 e in this transfer. For p+p operations, protons are injected from the 200 MeV Linac into the transfer, followed by acceleration in the AGS and injection into RHIC.

The RHIC synchrotron ring consists of two quasi-circular concentric accelerator/storage rings on a common horizontal plane, blue and yellow rings. Each ring has its own dependent set of bending and focusing magnets as well as ratio frequency cavities, but both of them share a common horizontal plane detectors.

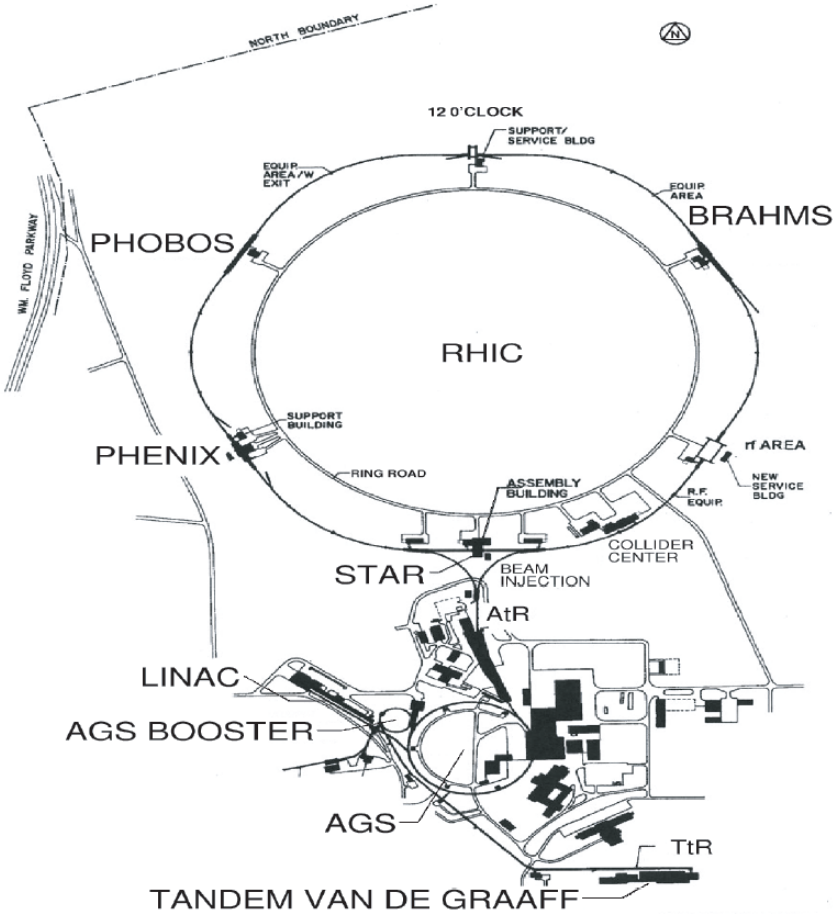

Figure 2.1: Schematic of the RHIC complex, including the accelerators and detectors, taken from [Rua05] [Sor].

To analyze RHIC physics, four experiments as the eyes of RHIC are set on the RHIC ring. They are two large experiments STAR (6 o'clock) and PHENIX (8 o'clock) and two smaller ones PHOBOS (10 o'clock) and BRAHMS (2 o'clock), respectively.

2.2 STAR Detector overview

As mentioned before, Solenoidal Tracker at RHIC (STAR) is one of four main detector systems at Brookhaven National Laboratory. It was specially designed to investigate the behavior of strongly interacting matter at high energy density and to search for signatures of quark-gluon-plasma (QGP) formation. Key features of the nuclear environment at RHIC are a large number of produced particles (up to approximately 1000 per unit

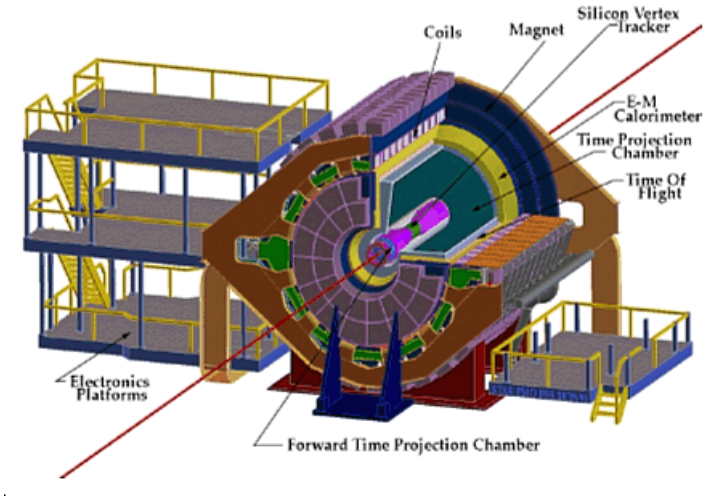

Figure 2.2: Perspective view of the STAR detector.

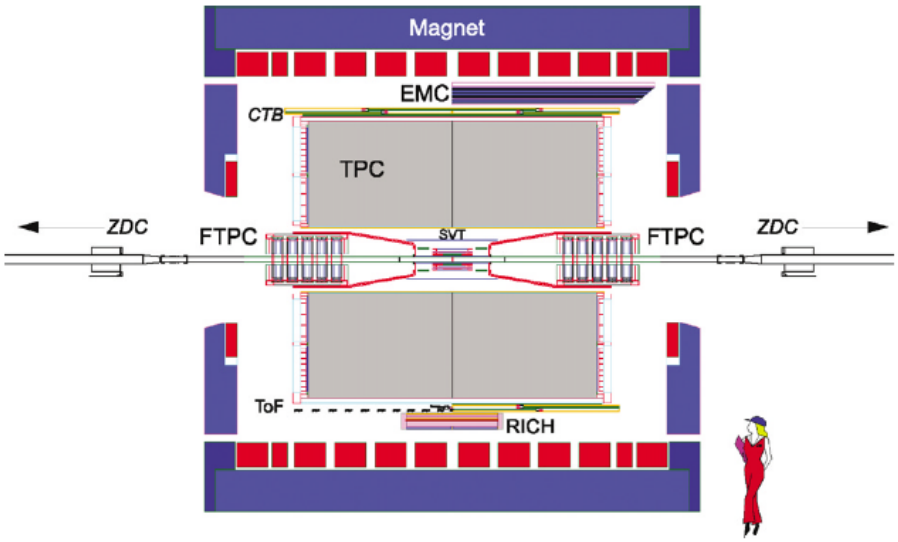

Figure 2.3: Cutaway side view of the STAR detector.

of pseudo-rapidity) and high momentum particles from hard parton-parton scattering. STAR can measure many observables simultaneously to study signatures of a possible QGP phase transition and to understand the space-time evolution of the collision process in ultra-relativistic heavy ion collisions. The goal is to obtain a fundamental understanding of the microscopic structure of these hadronic interactions at high energy densities. In order to accomplish this, STAR was designed primarily for measurements of hadron production over a large solid angle, featuring detector systems for high precision tracking, momentum analysis, and particle identification at the mid-rapidity. The large acceptance of STAR makes it particularly well suited for event-by-event characterizations of heavy ion collisions and for the detection of hadron jets.

STAR consists of the main tracker detector, Time Projection Chamber (TPC), and several other subsystems. The Layout of the STAR experiment is shown in Fig. 2.2, including magnet, Electro-Magnetic Calorimeter (EMC), Time-of-Flight (TOF), TPC, Forward TPC (FTPC) and Silicon Vertex Tracker (SVT) from outer side to inner side. A cutaway side view of the STAR detectors is displayed in Fig. 2.3.

The STAR Magnet is designed to provide uniform magnetic field of maximum value 0.5 T (called full field in STAR) and 0.25 T (half field) for charged particle momentum analysis. It's built with a length of 6.85 m and inner and outer diameter of 5.25 m and 7.32 m respectively. In the field, charged particles are bend through the detectors, which allow people to measure the helical trajectory, and obtain their momenta. Up to now, the STAR magnet has been run in full field, reversed full field and half field configurations.

The TPC is the main tracker detector of STAR. It is $4m$ long, locating at a radial distance from 50 to 200 cm from the beam axis, and covering a pseudo-rapidity range $|\eta| < 1.8$ and full azimuthal symmetry ($\Delta\phi = 2\pi$). The details of the TPC will be discussed later (sec. 2.3). To extend its rapidity coverage, two radial-drift TPC are installed at the forward region (FTPC), covering $2.5 < |\eta| < 4$. To improve the precision of the tracking at the forward region, a Forward GEM Tracker (FGT) based on triple GEM technology is proposed and in preparation [Sim08]. In addition, the inner tracker detectors, Silicon Vertex Tracker (SVT) and Silicon Strip Detectors (SSD) covering $|\eta| < 1$ and complete

azimuthal symmetry, are set in the TPC to provide precise localization of the primary interaction vertex and identification of secondary vertices from weak decay of K^0_S, Λ, Ω and so on. The SVT consists of 216 silicon drift detectors (equivalent to a total of 13 million pixels) arrange in three cylindrical layers at distances of approximately 7, 11 and 15 cm from the beam axis. The SSD is the fourth layer of the inner tracking detector, at a distance of approximately 23 cm from the beam axis. However, these inner tracker detectors result in considerable material budget, which provide lots of photonic background to the electron related analysis, so they are removed at year 2007. Another new silicon vertex detector Heavy Flavor Tracker (HFT) [Sha07] is proposing to replace the SVT and SSD for precise vertices. This detector will have two layers of pixels with limited materials, locating at mean radius of 1.5 cm and 5 cm from the beam axis, respectively. The SSD will be re-installed to fill the gap between the innermost silicon detectors and the TPC.

The Time-Of-Flight (TOF) [Sha06a, Don06, Llo05] based on Multi-Resistive Gap Chamber (MRPC) technique, was designed and installed at the outer of TPC. It covers $|\eta| < 1$ in pseudo-rapidity and complete azimuthal angle. Its intrinsic timing resolution is less than 80 ps and detecting efficiency is larger than 95%. It extend particle identification for π/K (p/K) separation from 0.6 (1.0) GeV/c up to 1.8 (3.0) GeV/c. Together with the TPC, identification for charged hadrons have been extended to 12 GeV/c in Au+Au collisions so far [Abe06], and electron can be identified at $p_T > 0.2$ GeV/c. The trigger system of the TOF detector is the two (upgraded-) Pseudo Vertex Position Detector, (u-) pVPD, each staying 5.4 m away from the TPC center along the beam line. They provide a starting time information for the TOF and pseudo vertex position of each event.

The μ identification with the TOF are limited at low p_T ($0.17 < p_T < 0.25$ GeV/c), where the time of flight difference between π and μ is big enough to separate them [Abe08]. To extend μ capability up to higher p_T, a μ detector, Muon Telescope Detector (MTD), is proposed at STAR [Rua09]. The technique for the MTD is similar to that for the TOF. However, the MTD has much larger readout strips and sits outside of the STAR magnet (~ 4.2 m away from beam line center), so that almost all electrons and charged hadrons

can be absorbed by the BEMC and STAR magnet. Its detecting efficiency is 40-50% for μ at $p_T > 2$ GeV/c, including acceptance. A MTD prototype has been installed at STAR in year 2007 and works well [Rua08, Sun08].

The STAR Barrel Electro-Magnetic Calorimeter (BEMC) located at outside of the TOF covers $|\eta| < 1$ with complete azimuthal symmetry [Bed03]. The Endcap Electro-Magnetic Calorimeter (EEMC) provides coverage for $1 < \eta \leq 2$, over the full azimuthal range, supplementing the BEMC [All03]. This system was proposed to measure transverse energy of events, and trigger on high p_T photon, electron and electro-magnetically decayed hadrons. This feature together with its high data acquisition rate capability allows us to use it as a trigger to collect events with high p_T tracks. This is very important for high p_T physics (rare probe). The data analysis will be discussed in detail in Sec. 2.4.

The number of recorded events at STAR are limited by the slowest detector, the TPC, whose rate is about 50 Hz in Au+Au collisions. To obtain different physics, STAR online trigger systems are used to select interesting events. The fast detectors that provide input to the trigger system are a Central Trigger Barrel (CTB) at $|\eta| < 1$, Zero-Degree Calorimeters (ZDC) located in the forward direction at $\theta < 2$ mrad and Beam-Beam Counter (BBC). The CTB surrounds the outer cylinder of the TPC, and triggers on the flux of charged-particles in the mid-rapidity region, but it will be replaced by the TOF. The ZDC is used for determining the energy in the neutral particles remaining in the froward directions. The BBC consists of a hexagonal scintillator array structure at $\pm$ 3.5 m from the nominal interaction point. It is the main device to make the relative luminosity measurement and to provide a trigger to distinguish $\vec{p}\vec{p}$ events from beam related background events by means of timing measurements.

2.3 Time Projection Chamber

The TPC developed from Multi-Wire Proportional Chamber (MWPC) and Drift Chember (DC), is used as primary tracking device of the STAR detector [And03b]. It records the tracks of particles in 3-dimension, provide information of their momenta, and

ionization energy loss (dE/dx) which can be used for particle identification.

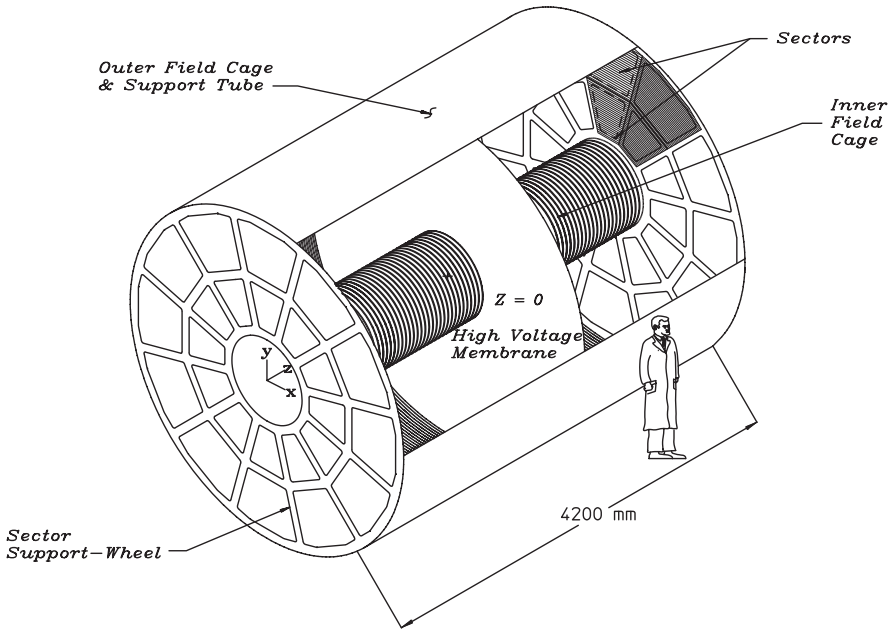

Figure 2.4: The schematics of the STAR TPC.

Fig. 2.4 shows the STAR TPC structure schematically. It consists of 4.2 m long cylinder along beam line with 4 m in diameter, Central Membrane (CM), Inner and Outer Field cages, and the readout end-caps.

The cylinder with active volume from radius 0.5 m to 2.0 m is filled the P10 gas (10% methane and 90% argon), which has long been used in TPCs, regulated at 2 $mbar$ above atmospheric pressure. The 90% argon is chosen for its low ionization energy $\sim$ 30 ev, and 10% methane is mixed for enhancing the number of ionization and absorbing electrons from excited argon radiation. The transverse diffusion of electrons in P10 is 230 $\mu m/\sqrt{cm}$ or about $\sigma_T = 3.3$ mm after drifting 210 cm within magnetic filed at 0.5 T . The longitudinal diffusion of a cluster of electrons that drifts the full length of the TPC is $\sigma_L = 5.2$ mm. This sets the scale for the resolution of the tracking system in the drift direction. The thin conduction Center Membrane (CM) located at the center of the cylinder separate the TPC into two parts. Each part provides uniform electric field

of $\sim$ 135 V/cm together with a chain of 183 resistors and equipotential rings along the Inner and Outer field cages from the CM to the ground planes. The electric field can drift the ionized electrons to the readout system based on MWPC and read pads, which can provide the x- and y- positions for the electrons. The Fig. 2.5 shows a cut-away view of inner sub-sector and outer sub-sector pad plane in one pad plane, and the cut is taken along a radial line from the center of the TPC to the outer field cage, so the center of the detector is to the right (*i.e. the right sub-sector is the inner pad and the left is the outer*). The amplification/readout layer is composed of the anode wire plane of small, 20 mm, wires with the pad plane on one side and the ground wire plane on the other. The third wire plane is a gating grid. The end view of one sector of pad plane is shown on the Fig. 2.6. The outer radius sub-sectors have continuous pad coverage to optimize the dE/dx resolution. This is optimal because the full track ionization signal is collected and more ionization electrons improve statics on the dE/dx measurement. Another modest advantage of full pad coverage is an improvement in tracking resolution due to anti-correlation of errors between pad rows. The inner sub-sectors are in the region of highest track density and thus are optimized for good two-hit resolution. This design uses smaller pads and the pad plane to anode wire spacing is reduced accordingly. The inner sector only serves to extend the position measurements along the track to small radii thus improving the momentum resolution and the matching to the inner tracking detectors. It also helps to detect particles with lower momentum. The parameters of the outer and inner sub-sectors are summarized in Table 2.3. The ground grid plane of 75 μm wires completes the sector MWPC. The primary purpose of the ground grid is to terminate the field in the avalanche region and provide additional shielding for the pads. This grid can also be pulsed to calibrate the pad electronics. The outermost wire plane on the sector structure is the gating grid, located 6 mm from the ground grid. This grid is a shutter to control entry of electrons from the TPC drift volume into the MWPC. It also blocks positive ions produced in the MWPC, keeping them from entering the drift volume, where they would distort the drift field. The gating grid plane can have different voltages on every other wire. It is transparent to the drift of electrons while the event is

being recorded and closed the rest of the time. The positive ions are too slow to escape during the open period and get captured during the closed period.

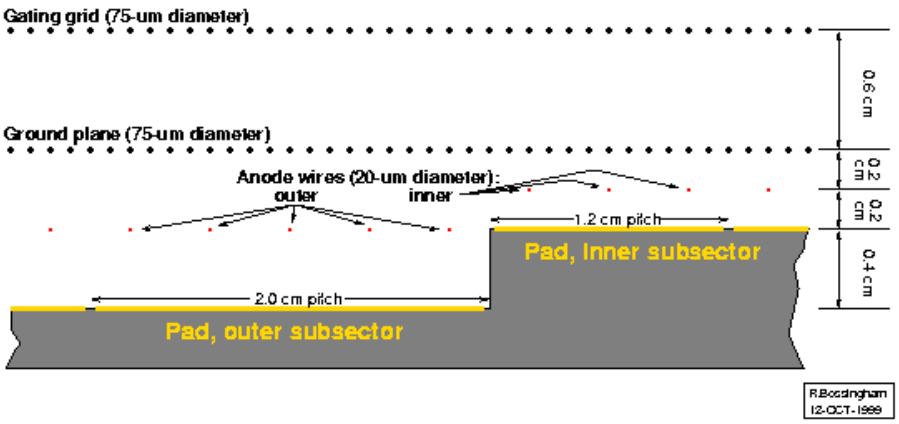

Figure 2.5: The basic arrangement of the wires relative to the inner (close to the right) and outer pad rows (close to the left).

Let's summarize how the TPC works? When the charged particle goes through the gas volume, electron-ions pairs are ionized by the charged particle in the P10 gas. Then, the electrons drift to the end-caps in the uniform electric field, and the drift time and the uniform drifting velocity provide the position in Z-direction along beam line. Consequently, the drifting electrons go to the end readout system, which is mounted on aluminum support wheels. The electron avalanche in the high field at the 20 μm anode wires providing an amplification of 1000-3000. Finally, the pads included in the chamber collect induced signal with other three wire planes, which are show on the Fig. 2.5. Therefore, the clusters can be found precisely in transverse plane separately.

Table 2.2: Parameters of the TPC inner and outer subsectors.

Item	Inner subsector	Outer subsector	Comment
Pad size	2.85 mm × 11.5 mm	6.20 mm × 19.5mm	
Isolation gap between pads	0.5 mm	0.5 mm	
Pad rows	13	32	
Number of pads	1750	3942	5692 total
Anode voltage	1170 V	1390 V	20:1 signal:noise
Anode gas gain	3770	1230	

The track is reconstructed by tracking software (ITTF), which not only associates

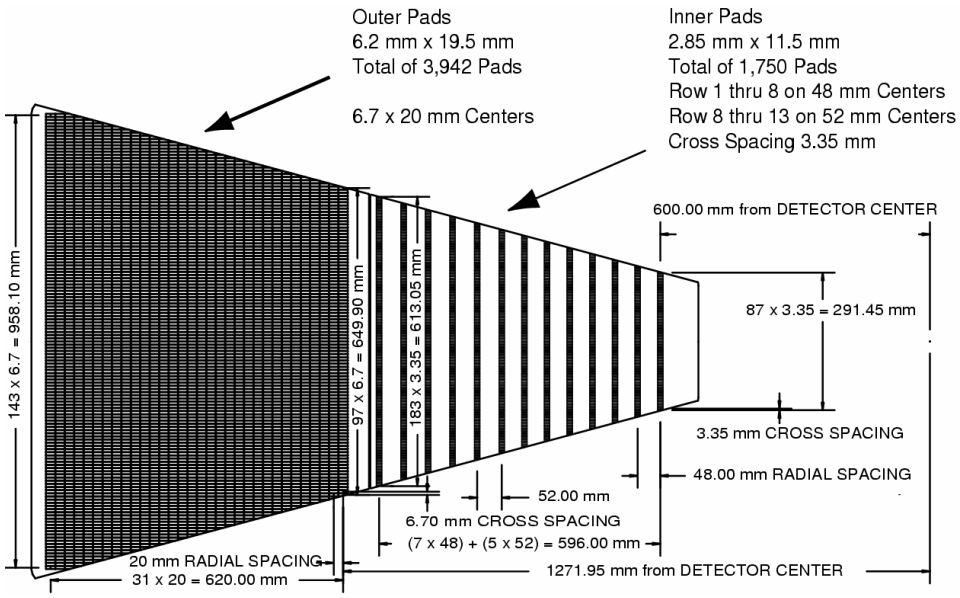

Figure 2.6: The anode pad plane of one full TPC sector. The inner subsector is on the right and it has small pads arranged in widely spaced rows. The outer subsector is on the left and it is densely packed with larger pads.

space points to track, but also fits the points with a track model to extract momentum information. The clusters are found separately in transverse plane and on the direction of beam line. The position resolution depends on the drift length and the angle between the particle momentum and the drift direction and on the level of mm. After finding and associating the clusters along the track, it is fitted to track models. The track model is, to first order, a helix. Second-order effects include the energy lost in the gas which cause a particle trajectory to deviate slightly from the helix. The track is then be extrapolated to the other detectors and the points from other detectors might be added. At the end this track is then fitted with a more sophisticated fitting method and from there on is called a global track. Once all of the global tracks from the same event have be reconstructed, the primary vertex of this event can be reconstructed with pretty good accuracy. The vertex resolution inversely proportional to the square root of the number of tracks in the calculation and can reach 350 μm in central Au+Au collisions. After getting the primary vertex, a track which originates from the primary vertex can be refitted using the primary vertex as additional point. If the distance of closest approach (dca) of a global track is small enough ($<$ 3 cm for example) and the refitting works out well then this

refitted track is marked as primary track and stored into a separated collection for further use. The momentum resolution of primary track in p+p collisions is approximately $\Delta p_T/p_T \approx 1\% + 0.5\% \times p_T$.

Distortion and gating grid Electron drifting velocity is about 5.45 cm/μs, while the positive ion velocity is about 100 cm/s. This can leave lots of ions in the drift chamber, and add an electric field, with x- and y- component, to original uniform field in z direction. Therefore, the drifting electron will also get x- and y- component, and move away from where they should be on the pad plane. The simple cartoon on Fig. 2.7 shows the field lines in inner and outer sector in red arrows, and the force direction of electron in blue arrows. In addition, some ions ionized in the MWPC chamber, leak to the drift chamber through the gate grid, called grid leak. This also induces the non-uniform field in drifting chamber. This effect increases with higher luminosity, so increased ionization levels in the TPC gas may be happened with the rising luminosity for physics goal of STAR experiment at RHIC recently and future. The resulting ionic space charge and grid leakage introduce field distortions in the detector which systematically shift the reconstructed momentum of positive and negative particles in oppositive directions. The effect is expected to grow as function of p_T. STAR has developed a method for correcting the track reconstruction due to space charge distortion [Van06]. Performance of the corrections can be assessed by examining the distribution of signed DCA (Distance of Closest Approach of a primary track to the collision vertex) as a function of luminosity. However, residual distortion after above correction has been observed through the ratio of electrons to positrons (e^-/e^+) dominantly from gamma conversion. We expect e^-/e^+ to be unity independent of p_T since $\gamma \rightarrow e^- + e^+$ and a significant fraction of leptons from heavy-flavor decays are also expected to be close to unity [Ada05c, Abe07d, Abe08]. The high-statistics data set from the BEMC trigger is ideal for such a study, and the details will be discussed in section 2.4.

The ionization energy lost in the TPC gas provides a effective tool for identifying particle species. The dE/dx can be extracted from the energy loss measured on up to 45 pad-rows. Therefore, the maximum number of dE/dx is 45 for a given track. The dE/dx values of hits associated with the track have a typical Landau tail due to

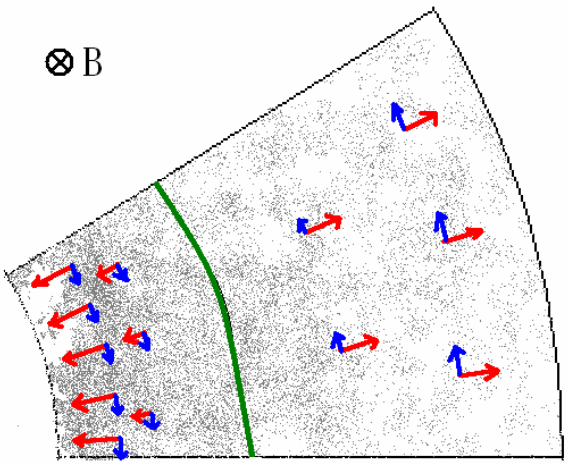

Figure 2.7: The cut view of the TPC with additional electric field due to space charge in inner and outer sectors. Red arrows represent electric field line, and blue arrows are the force direction of electron. The black cross means the magnet field.

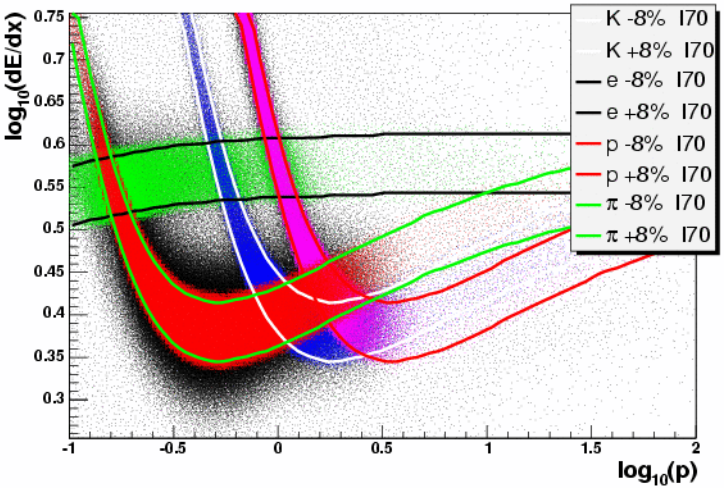

Figure 2.8: Distribution of $log_{10}(dE/dx)$ as a function of $log_{10}(p)$ for electrons, pions, kaons and protons. The units of dE/dx and momentum are keV/cm and GeV/c, respectively. The color bands denote within $\pm 1\sigma$ the dE/dx resolution. $I70$ means Bichsel's prediction for 30% truncated dE/dx mean.

uncertainties in thin gas, δ_e etc. The hits with the top 30% of high dE/dx values are discarded and an average of dE/dx value from the rest of the hits is derived for that track [And03a]. This method is called "truncated mean". The dE/dx for a given particle at low momentum decreases with increasing momentum to reach a minimum ionization, then increases due to the relativistic rise. For a minimum ionizing particle (MIP) the dE/dx resolution in the STAR TPC is 6-8% for a track with the maximum of 45 sampled dE/dx points. pions are well separated from the rest ($e^{\pm}$, $K^{\pm}$, $p(\bar{p})$) at $0.3 < p_T < 0.6$ GeV/c (with $\beta\gamma$ in 2∼4). This has been used to calibrate the TPC dE/dx without other means of identification. It provides the fixed points for the dE/dx function to extrapolate to higher momentum. In the thin material (TPC gas), the Bichsel function was proved to be a very good approximation for dE/dx and has been adopted by STAR as a standard method of predicting dE/dx position for charged hadrons in all momentum ranges [Bic06].

$$\Delta_p = \xi[ln(\frac{2m_e c^2\beta^2\gamma^2}{I}) + ln(\frac{\xi}{I}) + 0.2 - \beta^2 + \delta(\frac{\beta}{\gamma})], \tag{2.1}$$

$$\xi = (\frac{K}{2})z^2(\frac{Z}{A})(\frac{x}{\beta^2})MeV, \tag{2.2}$$

Where δ_p is the most probable energy loss, and the parameters can be found from [Bic06]. The Landau function is an approximation which does not include features related to atomic structure. The Landau function [Bic06] is an approximation which does not include features related to atomic structure. With the Bichsel function, a decrease of the relativistic rise of dE/dx with increasing segment length x is seen and parameterized empirically. This effect, gas multiplication gains and noise of TPC electronics and pileup in high luminosity environment may make the dE/dx deviate from the Bichsel function. This need re-calibration of dE/dx, which are discussed in Chapter 3.

Fig. 2.8 shows the 70% truncated mean dE/dx distribution. It's resolution is less than 8%, which makes the π/K separation up to $p \sim 0.7$ GeV/c and proton/meson separation up to $p \sim 1.1$ GeV/c. The TPC is originally designed to identify particles at low momentum. Fortunately, the separation of dE/dx of particles at relativistic rising region also allows people to identified particles at high momentum ($p > 3$ GeV/c) [Sha06a, Xu08].

The K/π (p/K) separation is approximately 1.7σ ($\sim 0.3\sigma$) at $p_T = 3$ GeV/c and 1.5σ ($\sim 1\sigma$) at $p_T = 10$ GeV/c [Xu08] in p+p collisions.

2.4 Barrel Electro-Magnetic Calorimeter

The BEMC is located at interval between the TPC and the magnet coils, and covers 2π in azimuthal and $|\eta| \leq 1$ after year 2006 ($0 \leq \eta \leq 1$ in year 2005), matching the acceptance for full TPC tracking. The inner surface of the BEMC has a radius of about 220 cm and parallel to the beam axis.

The design for the BEMC includes a total of 120 calorimeter modules, each subtending 6° in $\Delta\phi$ (~ 1 rad) and 1.0 unit in $\Delta\eta$. These modules are mounted 60 in ϕ and 2 in η. Each module is roughly 26 cm wide by 293 cm long with an active depth of 23.5 cm plus $\sim$ 6.6 cm in structural plates (of which $\sim$ 1.9 cm lies in front of the detector). The modules are further segmented into 40 towers, 2 in ϕ and 20 in η, with each tower subtending 0.05 in $\Delta\phi$ by 0.05 in $\Delta\eta$. The full BEMC is thus physically segmented into a total of 4800 towers. Each of these towers in projective and points back to the center of the TPC. Fig. 2.9 shows a schematic side view of a module illustrating the projective nature of the towers in the η direction.

The BEMC is a sampling calorimeter using lead and plastic scintillator because of the large area and complex geometry. Fig. 2.10 shows an end view of a module showing the mounting system and the compression components. The core of each BEMC module consists of a lead-scintillator stack and Shower Maximum Detectors (SMD) situated approximately 5 radiation length ($5X_0$) lengths from the front of the stack for high spatial resolution, which is a wire proportional counter-strip readout detector using gas amplification. The (SMD) is used to distinguish high momentum single photons from photon pairs from π and η meson decays. There are 20 layers of 5 mm thick lead, 19 layers of 5 mm thick scintillator and 2 layers of 6 mm thick scintillator. The thicker scintillator layers are associated with the pre-shower detector which is significantly helpful in both π^0/γ and electron/hadron discrimination. Totally, the BEMC has a depth of $\sim$20 X_0 at

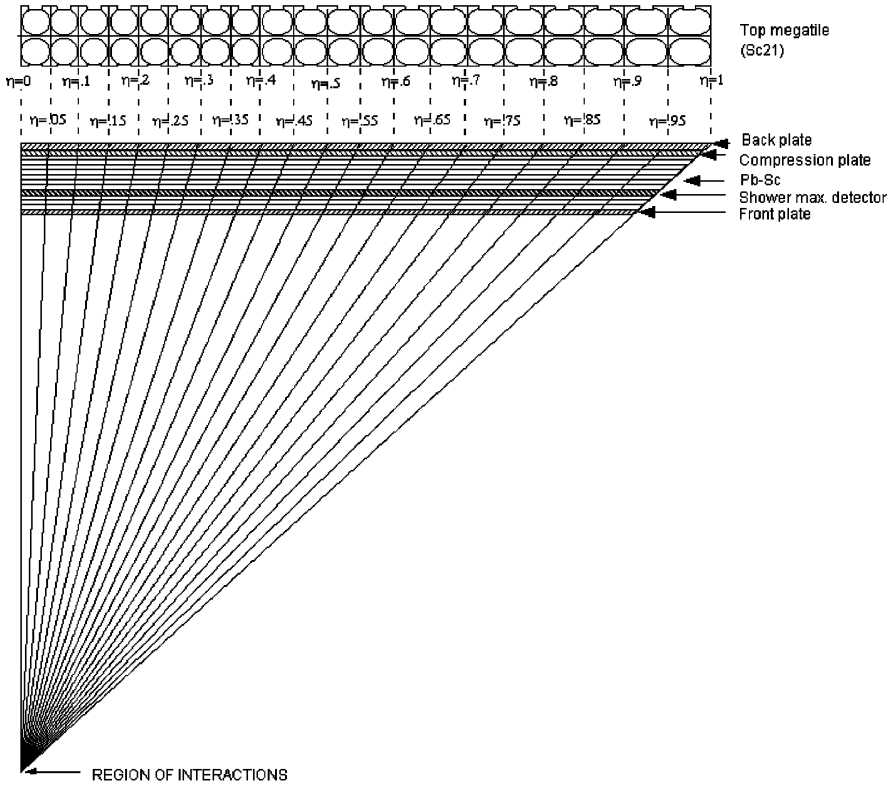

Figure 2.9: Side view of a calorimeter module showing the projective nature of the towers. The 21st mega-tile layer is also shown in plan view.

$\eta = 0$.

The intrinsic energy resolution of tower is $\sigma_E/E \approx 1.5\% \oplus 14\%/\sqrt{E}$. However, the hadron background can decrease the effective resolution in experiments. In central Au+Au collisions, the resolution for electron energy at 1.5 GeV and 3 GeV is around 17% and 10%, respectively [Bed03].

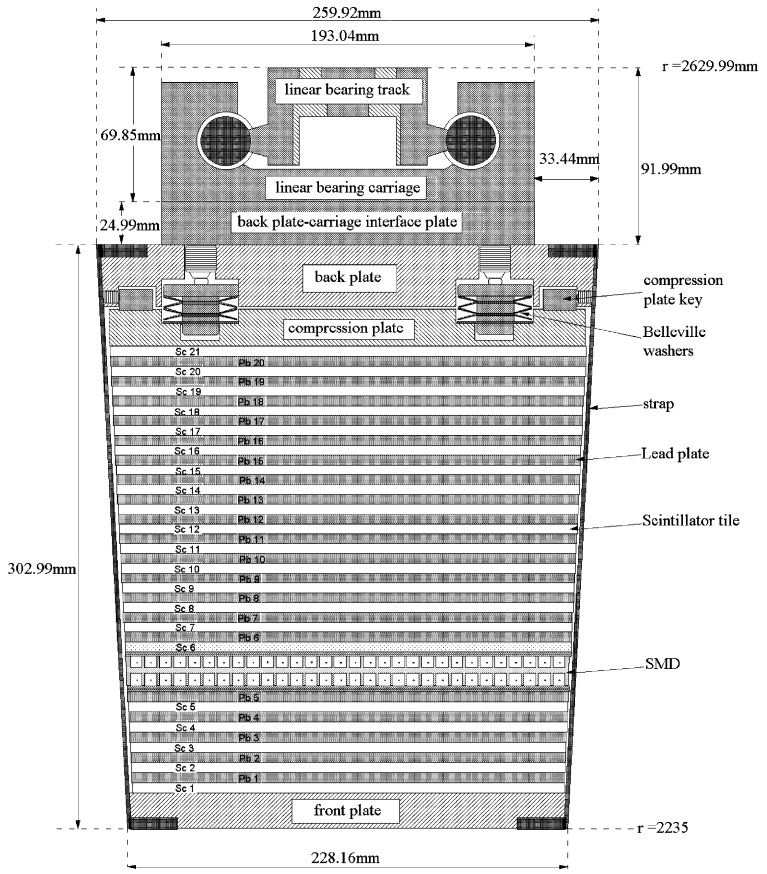

Figure 2.10: Side view of a STAR BEMC module showing the mechanical assembly including the compression components and the rail mounting system. Shown is the location of the two layers of shower maximum detector at a depth of approximately $5X_0$ from the front face at $\eta = 0$

This system allows measurement of the transverse energy of events, trigger on and measure high transverse momentum photons, electrons, and electromagnetically decayed hadrons. It can also be used to discriminate $\pi^0/\eta/\gamma$ and e/h by measuring the deposited energy and cluster size. The EMCs also provide prompt charged particle signals essential to discriminate against pileup tracks in the TPC, arising from other beam crossings falling within the 40 μs drift time of the TPC, which are anticipated to be prevalent at RHIC

p+p collision luminosity ($\sim 10^{32} cm^{-2} s^{-1}$). Besides, the system is taken as a fast detector due to its high rate comparing with TPC Data AcQuisition (DAQ) rate $\sim$100 Hz, while the actual interaction rates are in the order of 1 MHz for p+p collisions and 100 MHz for Au+Au collisions. This allows STAR to trigger on or filter events for studying rare, high p_T processes (jets, leading hadrons, direct photons, heavy quarks) and providing large acceptance for photons, electrons, π^0, η, J/ψ, Υ mesons in systems spanning polarized p+p through Au+Au collisions.

In reverse, we can also discriminate hadrons from electrons. Then, a new method to reconstruct resonance is developed with one triggered hadron and discussed in Chapter 5. We have reconstructed K^0_S and Λ through their hadronic decay mode, such as $K^0_S \rightarrow \pi^+ + \pi^-$,$\Lambda \rightarrow p(\overline{p}) + \pi^-(\pi^+)$, and extend these measurements up to 12 GeV/c using the BEMC triggered events. The details can be found in Chapter 5. With the same way, we can also $K^\star \rightarrow \pi^\pm + K^\mp$, $\rho \rightarrow \pi^+ + \pi^-$, $\phi \rightarrow K^+ + K^-$ etc, which are discussed in the Chapter 7.

CHAPTER 3

Charged particle identification in p+p collisions at $\sqrt{s_{NN}} = 200$ GeV

The study of identified hadron ($\pi^{\pm}$, $K^{\pm}$, $p(\overline{p})$) spectra at high p_T in p+p collisions provides a good test of perturbative quantum chromodynamics (pQCD) [AKK05, KKP01]. The $p(\overline{p})$ and $\pi^{\pm}$ spectra have been limited at $p_T \leq 7$ GeV/c and 10 GeV/c respectively, due to limited statistics in minimum bias triggered p+p collisions in the year 2003 [Ada06b]. They also have significant systematic errors due to the uncertainties in mean dE/dx position for proton and kaon [Ada06b]. In order to understand mechanism of hadron production, it's necessary to make a strict constraint on the quark and gluon FFs by comparing theory with experimental data at high p_T. In addition, it's also a good baseline for studying color charge effect of parton energy loss in heavy ion collisions, in which hadron spectra can arrive up to 12 GeV/c now [Abe06]. This chapter is dedicated to the details of analysis in p+p collisions.

3.1 Data Sets and Triggers

The data used for this analysis are collected from p+p collisions in the year 2005. The STAR main tracking detector, TPC provides a way to identify charged hadrons by measuring momentum and dE/dx information of charged particles [And03b]. As we mentioned before, the TPC is taken as slow detector, while the BEMC is a fast detector at STAR. Therefore, the BEMC [Bed03] was set as online triggers, "jet patch trigger", when the energy deposited on 300 nearby towers (0.2×0.2 in $\eta-\phi$) is larger than the threshold, and "high tower trigger" for energy deposited on the single tower 0.05×0.05 in $\eta \times \phi$

Table 3.1: Data sets used in this analysis.

Triggers	p+p(JP2)	p+p(HT1)	p+p(HT2)
EMC trigger threshold	$E_T > 6.4$ GeV	$E_T > 2.5$ GeV	$E_T > 3.4$ GeV
Number of events	5.6 M	5.1 M	3.4 M

within each patch. In this dissertation, a total of ∼5.6 million jet patch triggered events with energy threshold 6.4 GeV (JP2) in year 2005 are selected to improve the statistics for charged particles at high p_T range and extend our measurements up-to 15 GeV/c in p+p collisions at $\sqrt{s_{NN}}$ = 200 GeV. In order to reduce the trigger bias, only tracks on the away side of jet patch trigger are chosen by requiring azimuthal angle between one track and the trigger ($\Delta\phi$) larger than 90 degree or less then -90 degree.

3.2 Re-calibration Method

In Section. 2.3, we have introduced the dE/dx information in the STAR TPC, and the calibration of dE/dx in STAR collaboration. Due to some approximations in theoretical calculations and some effects in noise of the electronics, gas multiplicity gains, pileup in high luminosity etc., the dE/dx value in experiments may be deviated from the predictions of Bichsel function. The dE/dx separations among $\pi^{\pm}$, $K^{\pm}$ and $p(\bar{p})$ are about 1-3σ where the dE/dx amplitude of pions is the highest and that of protons is the lowest. Pions are the dominant sources of inclusive and jet hadrons, and they shadow kaons and protons in the dE/dx distribution. Clear peak separations of these three hadrons are not possible. This results in large systematic errors due to the uncertainty of dE/dx positions. Knowledge of the precise dE/dx positions for those hadrons is important to understand the efficiencies of PID selection and to reduce the systematic uncertainty in identified hadron yields. In order to improve the particle identification at high p_T, we develop a method to locate the dE/dx positions for different hadrons with good precision.

$\Lambda \rightarrow p + \pi^-$ ($\overline{\Lambda} \rightarrow \overline{p} + \pi^+$) and $K^0_S \rightarrow \pi^+\pi^-$ are reconstructed by their decay topology to identify their decay daughters – charged pions and protons. The identified electrons,

pions and protons provide the necessary distinct dE/dx positions and widths as function of $\beta\gamma$. The deviation from the prediction of the Bichsel function is used to correct for the dE/dx fit and then extract pion and proton yields from the charged hadrons in an inclusive hadron distribution or in a jet. The same method can be applied to p+p, d+Au and A+A collisions in STAR.

3.2.1 dE/dx distribution in the TPC at high p_T

The dE/dx in the TPC is a valuable tool for identifying particle species and works very well at low momentum ($p < 1.0$ GeV/c). Indeed, the detector was designed to separate particles up to 1.2 GeV/c. In addition, with dE/dx resolution of 6-8% at high p_T ($p_T > 3$ GeV/c) [Ada06b, Ada05e, Abe07a], charged pions can be identified by the dE/dx from the TPC, due to a more than 15% difference in dE/dx between pion and other charged particles ($K^{\pm}$, $p/\overline{p}$, $e^{\pm}$) [Sha06b]. Since pions are the dominant source of inclusive hadrons, it is relatively simple to extract pion yields from inclusive particles in this p_T range. To formulate the dE/dx[1] distribution and its associated Bichsel function for PID, we need to define the normalized dE/dx by following terms:

$$n\sigma_X = \frac{1}{\sigma_X} \log \frac{(dE/dx)_{measured}}{< dE/dx >_X}, \tag{3.1}$$

where $dE/dx_{measured}$ is the measured mean dE/dx for a truncated 70% track, $< dE/dx >_X$ is the expected mean dE/dx from Bichsel function for charged particle x with a given momentum, and σ_X is the ln(dE/dx) resolution of the TPC [Sha06b], which depends on the characteristics of each track, such as number of hits measured in the TPC used for dE/dx measurement, path length (X) and the psudo-rapidity of a track. Fig. 3.1 shows $n\sigma_\pi$ distribution of all the charged particles for $3.75 < p_T < 4.0$ GeV/c at $\mid \eta \mid < 0.5$. In order to put all the dE/dx distributions into one histogram to perform a simultaneous fit, the dE/dx distribution is shifted by +6 for positive and -6 for negative charged particles in the histogram, which is presented in Fig. 3.1. An eight-Gaussian function is used to

[1] dE/dx is used to represent the "track descriptor" C defined on p.170 of [Bic06]

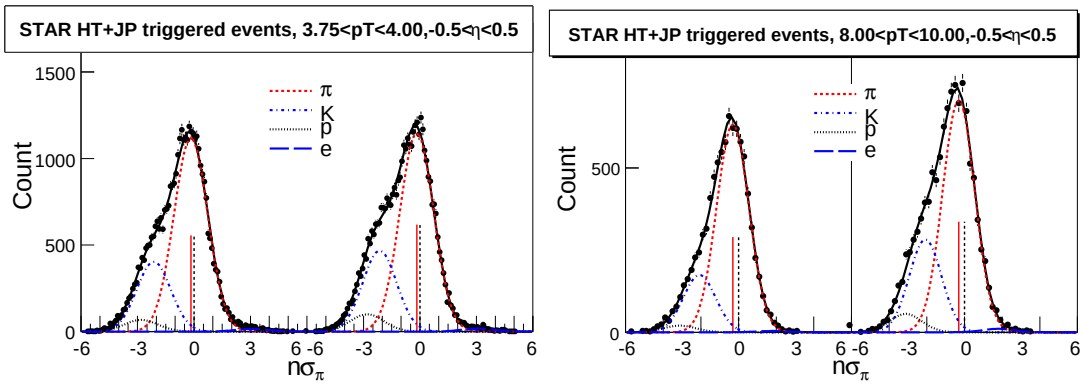

Figure 3.1: $n\sigma_{\pi}^{h}$ distribution at 3.75<p_T<4.0 GeV/c for positive (left panel) and negative (right panel) particles. The solid line is the fit curve by 8-Gaussian function, including pion (dashed line), kaon (dot-dashed line), proton (dotted line), and electron (long-dash line). Two solid vertical lines are fitted pion position, while the dashed vertical lines are calculated positions.

fit this distribution with thirteen parameters to obtain the identified hadron yields and each Gaussian describes one dE/dx distribution for a charged particle. The parameters are peak positions relative to pion peak ($n\sigma_{\pi}^{\pi}$, $n\sigma_{\pi}^{K}$-$n\sigma_{\pi}^{\pi}$, $n\sigma_{\pi}^{p}$-$n\sigma_{\pi}^{\pi}$, $n\sigma_{\pi}^{e}$-$n\sigma_{\pi}^{\pi}$), eight yields for the charged particles and one Gaussian width. With ideal calibration, $n\sigma_{\pi}^{\pi}$ should be a normal Gaussian distribution centered at zero with width of unity. Fig. 3.1 shows that the pion dE/dx position is deviated from the Bichsel function. This means that the dE/dx calibration is not perfect, which also implies that dE/dx position of other particles relative to that of the pions may be off from their theoretical values.

In order to improve particle identification and reduce the systematic uncertainty in identified particle yields from dE/dx [Ada06b, Ada05e, Abe07a], we study in details the precise dE/dx positions of all charged particles using the enhanced electron by the BEMC, pure proton decayed from Λ and pion decayed from K_S^0 in the TPC. Once all the dE/dx positions and widths for all the charged hadrons are obtained by other means, we are able to constrain better the Gaussian fits, and understand the efficiency and contamination better in the case of PID selections for other physics analysis.

3.2.2 Electron identification by the BEMC

Although electron dE/dx is relatively far away from other charged particles, its yields are orders of magnitudes down from pions. In order to identify a electron and obtain its dE/dx position, the dataset with the BEMC trigger based on the energy deposited in the BEMC tower is used to enhance the yield of electrons relative to other particles. Additional hadron rejection is achieved from the shower shape and position from the SMD [Bed03, CPR02]. A unique feature of the SMD is its double layer design which makes it possible to reconstruct the shower as two-dimensional image, so that it can provide fine spatial resolution in ϕ- and η- direction and reject hadron according to different shower shape between hadron and electron. We require p/E to be 0.3< p/E <1.5 where p is track momentum in the TPC and E is the deposited energy of the BEMC tower, shower shape size measured by the SMD in η and ϕ direction to be $n_\eta \geq 2$ and ϕ direction $n_\phi \geq 2$, respectively. The different positions between hit in the BEMC tower and track projection in ϕ and z- direction are restricted to be $\mid \phi_{dist} \mid \leq 0.01\ rad$ and $\mid z_{dist} \mid \leq 2\ cm$ [Bed03]. The $n\sigma_\pi^h$ distribution for track passing these cuts are shown in Fig. 3.2 for 3.75<p_T<4.0 GeV/c. With about 1.5-3σ separation between electron (positron), and other charged hadrons, electron position and yields could be obtained from the eight-Gaussian function as above.

To correct for and to assess the systematic errors due to the residual momentum distortion, we use e^-/e^+ ratio as a function of p_T. Fig. 3.3 shows the ratio as a function of p_T obtained from the BEMC triggered data described as above. It increase as increasing p_T, indicating that the residual distortion on charged particle momenta due to space charge. If the electron and positron yields are a modified power-law function ($f(p_T) \propto (p_0 + p_T)^{-n}$) without any distortion, the distortion due to space charge in the TPC shifts all negatively charged tracks from p_T value to a higher $p_T + A \times p_T^2$ while it shifts all positively charged tracks from p_T value to a lower $p_T - A \times p_T^2$ [Van06]. Data points are fitted by the following function $f(p_T) = (\frac{2.67+p_T+A*p_T^2}{2.67+p_T-A*p_T^2})^{11.4}$, where $A * p_T^2$ means Δp_T affected by charge distortion, and $p_0 = 2.67$ and $n = 11.4$ are parameters obtained from

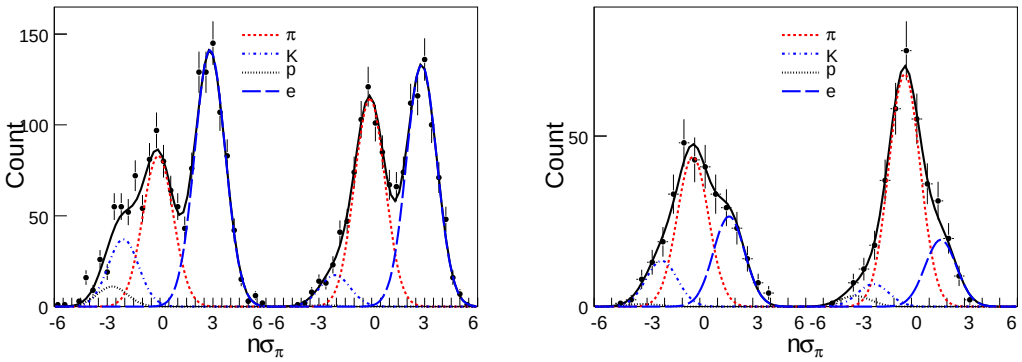

Figure 3.2: $n\sigma_{\pi}^{h}$ distribution with enhancement of electron and positron at 3.75 $< p_T <$4.0 GeV/c (left panel) and 8.0 $< p_T <$10.0 GeV/c (right panel) respectively, and 8-Gaussian function is used to fit these distributions.

the inclusive electron spectra [Abe08]. The p_T dependence of ratios indicates that the momenta of the charged particles obtained from the TPC tracking still systematically shifted away from their true value due to the space charge distortion. We note that the obtained distortion characterized by parameter A is only about 2σ from zero and this results in about 1.3% momentum shift for a single particle track at $p_T = 15$ GeV/c.

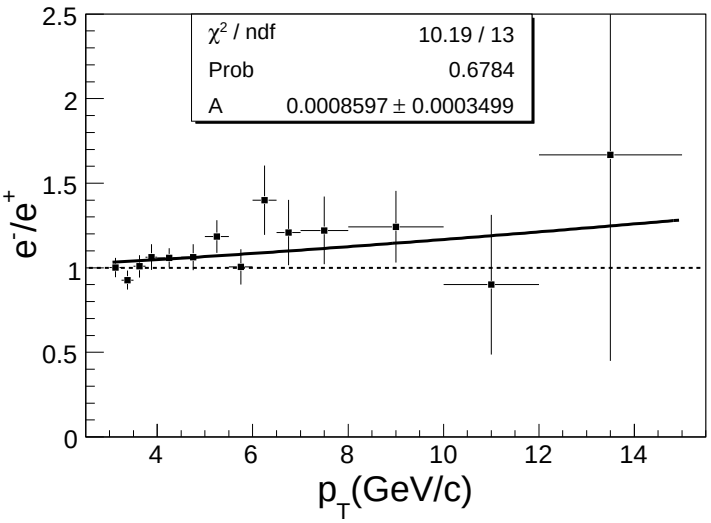

Figure 3.3: The ratio of e^{-}/e^{+} as a function of p_T. The curve is a power-law fit.

3.2.3 Proton and pion from $V0$ reconstructed in the TPC

In order to obtain the dE/dx position of proton ($n\sigma_\pi^p$) for $\beta\gamma > 4$, p ($\overline{p}$) are selected from Λ ($\overline{\Lambda}$) through $\Lambda \to p + \pi^-$ ($\overline{\Lambda} \to \overline{p} + \pi^+$) decays, because it is difficult to get dE/dx position of proton by $h^+ - h^-$ [Sha06b] with this data sample due to low statistics and small difference of yields of proton and anti-proton. At the same time, pions decayed from K_S^0 through $K_S^0 \to \pi^+ + \pi^-$ decay can be used to get dE/dx positions of pion ($n\sigma_\pi^\pi$) at 0.2<p_T<3 GeV/c. First, K_S^0 and Λ are selected by topological cuts on a secondary vertex [Sor] according to long decay length of K_S^0 ($c\tau$ = 2.6 cm) and Λ ($c\tau$ = 7.89 cm). Fig. 3.4 shows the invariant mass distribution for K_S^0 (upper panel) and Λ (lower panel). Then, pure K_S^0 and Λ ($\overline{\Lambda}$) are selected via their invariant mass cuts, 0.485<M(K_S^0)<0.505 GeV/c^2 and 1.112< $M(\Lambda)$ < 1.12 GeV/c^2, and their daughter particles (π, p ($\overline{p}$)) with high purity are obtained to derive $n\sigma_\pi^p$ and $n\sigma_\pi^\pi$. Fig. 3.5 shows $n\sigma_\pi^h$ distributions of pions decayed from K_S^0 (upper panel) fitted by Gaussian function and protons decayed from Λ (lower panel) fitted by the 2-Gaussian function. The protons decayed from Λ decay have higher background (signal-to-background ratio = 9:1) and a second Gaussian representing the pion contamination is necessary. Meanwhile, the p_T dependence of dE/dx width of protons and pions from the fits are obtained and shown in Fig. 3.6. The width is consistently smaller than unity (0.868 ± 0.004). This means that the dE/dx resolution is about 13% better than the prediction and the separations among particles are better than what we expected.

3.2.4 Theoretical values

To compare experimental results with theoretical values, the variables, $n\sigma_X$ - $n\sigma_\pi$ are filled in a histogram for obtaining theoretical expectation, since

$$n\sigma_X - n\sigma_\pi = \frac{\log(dE/dx_{exp}/dE/dx^X_{Bich})}{\sigma} - \frac{\log(dE/dx_{exp}/dE/dx^\pi_{Bich})}{\sigma} \tag{3.2}$$

$$= \frac{\log(dE/dx^X_{Bich}/dE/dx^\pi_{Bich})}{\sigma} = n\sigma_\pi^X \tag{3.3}$$

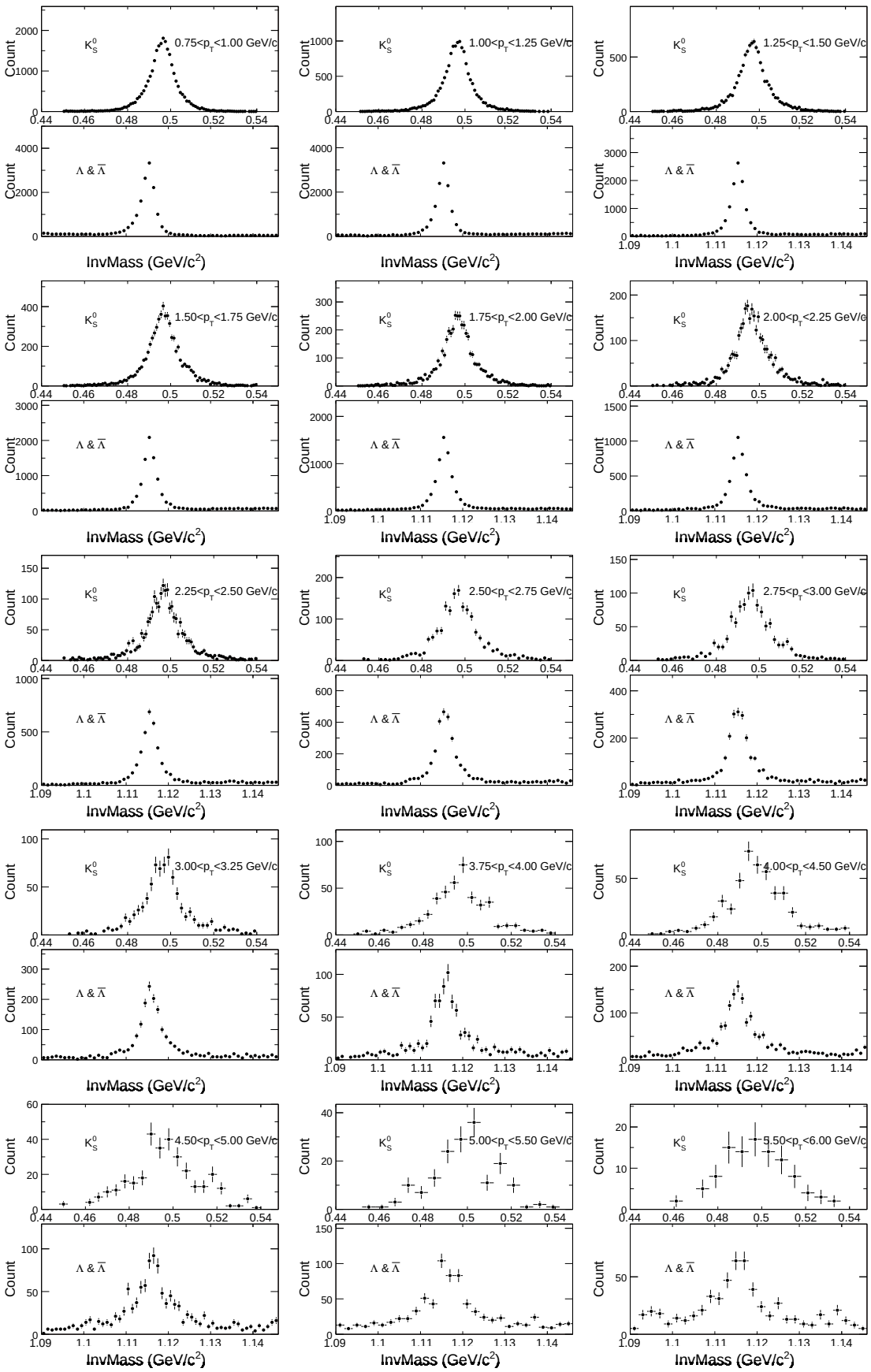

Figure 3.4: K^0_S and Λ invariant mass distribution vs daughter p_T.

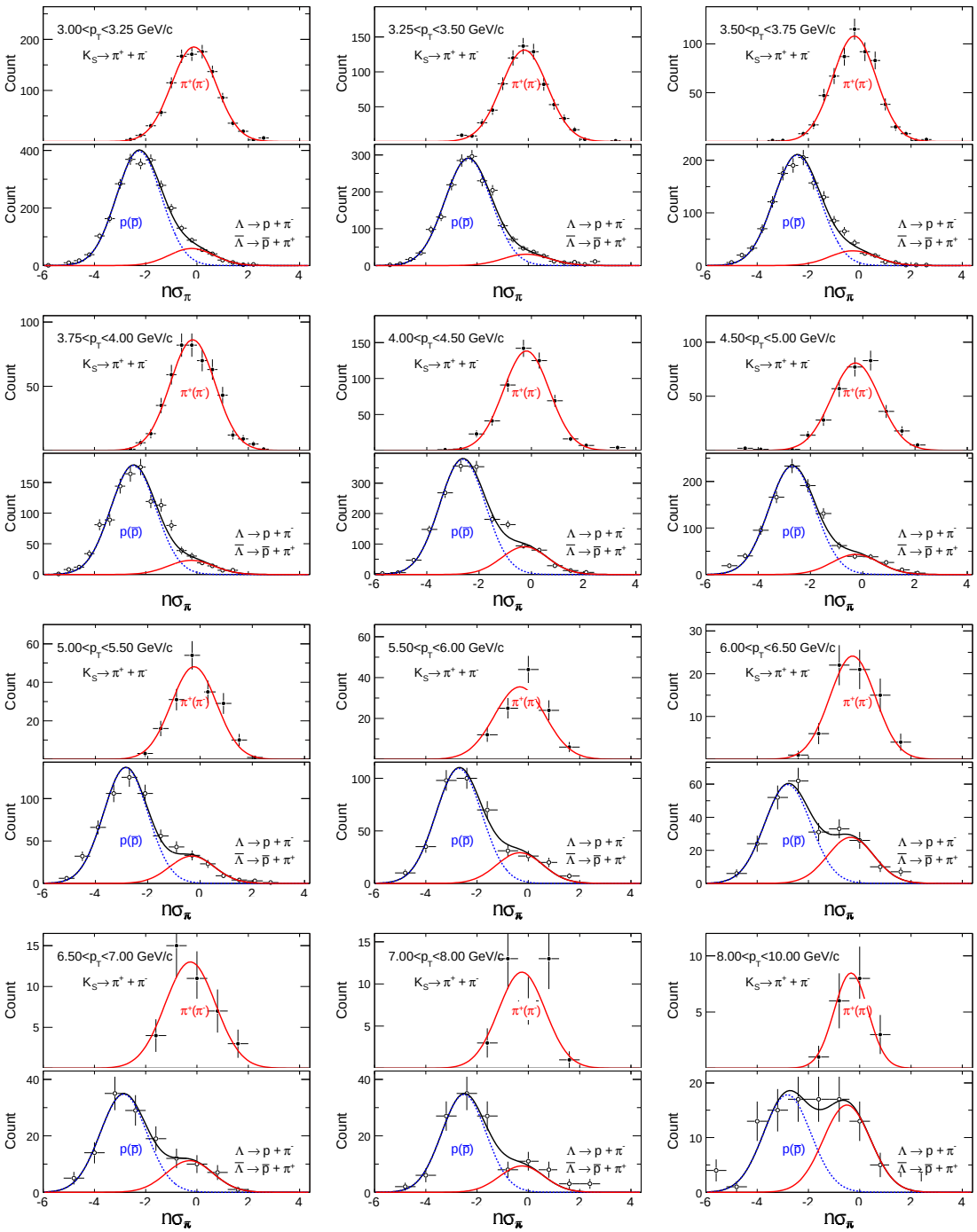

Figure 3.5: $n\sigma_{\pi}^{h}$ distributions of pion decayed from K_S^0(upper) and proton (lower) decayed from Λ. The solid curve is pion, and the dashed one is proton.

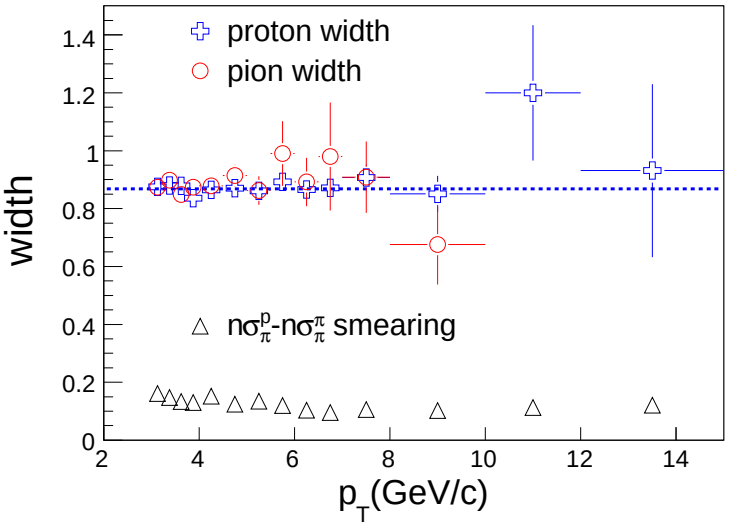

Figure 3.6: The width of $n\sigma$ as function of p_T for pion decayed from K^0_S and proton decayed from Λ. The triangles represent smearing of $n\sigma_p$ - $n\sigma_\pi$.

Where X can be $\pi^\pm$, $K^\pm$, $p(\overline{p})$ and $e^\pm$. In theory, $n\sigma_\pi^\pi$ is zero, and $n\sigma_X$ - $n\sigma_\pi$ is equal to $n\sigma_\pi^X$ - $n\sigma_\pi^\pi$.

Then, theoretical difference between pion and other charged particles can be derived by fitting the $n\sigma_X - n\sigma_\pi$ histogram at each p_T slice with Gaussian distribution, which are shown in the Fig. 3.7. The diffusions of dE/dx for each particle are fitted from these fit widths.

3.2.5 dE/dx deviation vs $\beta\gamma$

With identified pion, proton and electron mentioned above, the experimental results on the deviation of the normalized dE/dx ($n\sigma_\pi^h$) relative to the Bichsel theoretical values as a function of $\beta\gamma$ are shown in the left panel in Fig. 3.8. Since there is almost no particle species dependence of dE/dx, we can describe it with a function of

$$f(x) = A + \frac{B}{C + x^2} \tag{3.4}$$

The fit parameters are listed in Tab. 3.2. With these parameters, we can determine the dE/dx positions and widths of any given charged particles to be better than $< 0.1\sigma$ or

Table 3.2: Fit parameters from momentum and p_T dependence of $n\sigma_\pi^x$ deviation.

parameters	χ^2/ndf	A	B	C
p dependence	95/49	-0.423 ± 0.015	235 ± 23	464 ± 37
p_T dependence	94/48	-0.443 ± 0.015	234 ± 23	444 ± 35

$< 1\%$.

There are two ways to correct for this effect in the data. One can attempt to understand the origin of this deviation and correct for the effect at the hit level (the amplitudes of the ionization signal in each pad and row). This requires re-processing of the hits and reconstructing tracks from scratch. In order to take advantage of the existing compressed dataset with tracking information only, we apply the corrections to the dE/dx Gaussian function for each particle species without modifying the dE/dx itself. This empirical afterburner is applied in each p_T and rapidity bin to directly extract particle yields required by the physics analysis. Right panel in the Fig. 3.8 shows $p_T/mass$ dependence of the normalized dE/dx deviation, which is fitted by the same function as for the case of $\beta\gamma$. The parameters from the function are shown on Tab. 3.2. With the corrected deviation, differences of dE/dx between pion and other charged particles ($n\sigma_\pi^K - n\sigma_\pi^\pi$, $n\sigma_\pi^p - n\sigma_\pi^\pi$ and $n\sigma_\pi^e - n\sigma_\pi^\pi$) are calculated and compared with theoretical values as shown in Fig. 3.9. Clear offsets are depicted in Fig. 3.9 and details are shown on Tab. 3.3.

3.3 Raw yields for charged hadrons

3.3.1 Track selection

In order to get primary tracks, the Distance of Closest Approach (DCA) are required less than 1 centimeter. For good quality of reconstructed tracks, the number of fitted hits ($nHitFits$) are required ≥ 25, and the ratio of number of hits to number of possible hits should be larger than 0.55. The number of fitted hits for dE/dx ($ndedxpts$) is required to be larger than 15 for good dE/dx resolution. Besides, tracks on away-side of trigger

Table 3.3: Difference between $n\sigma_{\pi}^{K,p,e}$ and $n\sigma_{\pi}^{\pi}$ of theoretical values and re-calibrated results. We note that an additional factor of 0.868 should be applied to the final separation in the table taking into the narrower width observed in the data.

p_T(GeV/c)	$n\sigma_{\pi}^{K} - n\sigma_{\pi}^{\pi}$ (fit/theory)	$n\sigma_{\pi}^{p} - n\sigma_{\pi}^{\pi}$(fit/theory)	$n\sigma_{\pi}^{e} - n\sigma_{\pi}^{\pi}$(fit/theory)
3.125	-1.6837/-1.9545	-2.0315/-2.3256	3.2467/3.5737
3.375	-1.6822/-1.9673	-2.1481/-2.4639	3.1566/3.4598
3.625	-1.6754/-1.9706	-2.2382/-2.5777	3.0740/3.3537
3.875	-1.6679/-1.9721	-2.2854/-2.6465	2.9895/3.2536
4.25	-1.6681/-1.9822	-2.3476/-2.7190	2.8709/3.1028
4.75	-1.6891/-2.0201	-2.4343/-2.8395	2.6972/2.9001
5.25	-1.6810/-1.9398	-2.4778/-2.8967	2.5626/2.7482
5.75	-1.6363/-1.9697	-2.5055/-2.9432	2.4506/2.6220
6.25	-1.6025/-1.9359	-2.5089/-2.9559	2.3583/2.5096
6.75	-1.5758/-1.9030	-2.4862/-2.9367	2.2804/2.4167
7.5	-1.5287/-1.8429	-2.4340/-2.8871	2.1951/2.3193
9	-1.4856/-1.7705	-2.3729/-2.8224	2.0245/2.1132
11	-1.4427/-1.6941	-2.2718/-2.7065	1.7981/1.8705
13.5	-1.3675/-1.5744	-2.1548/-2.5583	1.6212/1.6984

are selected to reduce trigger bias in JP2 triggered events by requiring azimuthal angle between track and trigger, $|\Delta\phi|$ larger than 90 degree. The detailed cuts are listed in Tab. 3.4.

Table 3.4: Track quality cuts TPC.

variables	cuts	comments
dca	$< 1\ cm$	Distance of closest approach to the primary vertex
eta	< 0.5	the psudo-rapidity of track
nHitsFit	$\geq$25	the number of fit hits
nHitsFit/nPossHits	> 0.55	the ratio of the number of fit hits to the possible hits
$\Delta\phi$	$> \pi/2$	the azimuthal angle between track and trigger

3.3.2 raw yields from fitting method

Fitting method is used to obtain raw yields for charged particles. Firstly, the normalized dE/dx nσ_{π} are filled into a histogram to perform a simultaneous fit for all charged

particles. Fig. 3.10 shows the $n\sigma_{\pi}^{h}$ distributions for negative (left side) and positive (right side) particles in each p_T slice at mid-rapidity. Then, an eight-Gaussian function is used to fit the nσ_{π} distribution with above calibrated parameters: difference between pions and other particles (K, p, e), and the fit curves are also shown in the Fig. 3.10. Finally, raw yields for pion, kaon, proton and anti-proton are derived from these fit function.

3.3.3 raw yields from counting method

In ideal case, nσ distribution for each particles should be Gaussian and our fitting method should be perfect. Indeed, the nσ_{π} distribution is just an approximate Gaussian. To cross-check this, the so-called counting method is used to derive raw yields for protons, anti-protons and charged kaons. In this method, we take the left side of proton (anti-proton) region (*i.e.* $n\sigma_{\pi} < n\sigma_{\pi}^{p}$) as counting region. Then, a Gaussian distribution is assumed for dE/dx distribution of proton and kaon to calculate their contribution to the number of tracks in counting range. The peak positions for proton and kaon are fixed with re-calibrated value, and the width is from fitting method. Further more, we can count all tracks for pions, kaons, protons and electrons in the full $n\sigma_{\pi}$ range through solving following functions.

$$\pi + K + p + e = h, \tag{3.5}$$

In the counting range,

$$c1 \times p + c2 \times K = X, \tag{3.6}$$

where π, K, p and e represent full yields for each particle, and h are sum of these yields. c1, c2 are K, p contributions, and X is the total yield in the counting region. From these two equations, we can solve the counting yields for kaon, proton.

$$p = \frac{Y - c2 \times (h - \pi - e)}{c1 - c2}, \tag{3.7}$$

$$K = h - \pi - p - e, \tag{3.8}$$

In our analysis, raw yields from these two methods are averaged as final results, and the difference between them are taken into account of systematic uncertainties, which are discussed later.

3.4 Trigger enhancement correction

Due to trigger bias, there are differences between invariant yields in minimum bias events and the BEMC triggered events. Fig.3.11 shows charged pion spectra in the BEMC triggered events compared with published results (squares) in minimum bias triggered events. This indicates that statistics of charged pion at high p_T in the BEMC triggered events is much more than that in minimum bias triggered events. To correct this trigger effect, PYTHIA events are embedded in GEANT with STAR geometry, which can simulate the realistic response of the STAR detector in experiment, including signal of read-out and response of electronics, when tracks are propagated through detector. With simulated signal, different triggered events are selected by passing different detector thresholds as real events in STAR experiment. Together with results in experiment, simulated charged pion spectra in both triggers are shown on the left panel in Fig. 3.12. Then, the enhancement of charged pions can be calculated by dividing the BEMC triggered spectra by minimum bias triggered spectra. The right panel in Fig. 3.12 shows the enhancement factor versus p_T distribution. With the same way, trigger enhancement factors for kaon and proton are calculated and presented on the left and right panel in Fig.3.13.

3.5 Efficiency and acceptance correction

Tracking efficiencies for π, K, p and $\overline{p}$ are studied with the Monte Carlo simulation with the embedding technique [Abe09]. The simulated $\pi^{\pm}$, $K^{\pm}$, p and $\overline{p}$ are generated using a flat p_T and a flat y distribution and pass through GSTAR [Lon] (the framework software package to run the STAR detector simulation using GEANT [Ago03, All06] and TRS (the TPC Response Simulator [Lon])). The simulated π, K, p ($\overline{p}$) are combined

Table 3.5: Cuts used in simulation and reconstruction.

nHitsFit	gDCA (cm)	$\|\eta\|$	nHitsFit/nPossHits	nCommonHits
>25	<1.0	<0.5	>0.55	≥10

with a real raw event and we call this combined event a simulated event. This simulated event is then passed through the standard STAR reconstruction chain and we call this event after reconstruction a reconstructed event. The reconstructed information of those particles in the reconstructed event is then associated with the Monte-Carlo information in the simulated event. Then, we get the total number of simulated π, K, p and $\overline{p}$ from simulated events in a certain transverse momentum bin. Also, we can get the total number of associated tracks in the reconstructed events in this transverse momentum bin. In the end, the tracking efficiency can be calculated by following function:

$$\epsilon(trk) = \frac{N_{assosiatedTracks}}{N_{simulatedTracks}}, \tag{3.9}$$

where $N_{assosciatedTracks}$ is the number of associated (reconstructed) pion, kaon, proton and anti-proton, and $N_{simulatedTracks}$ is the number of simulated π, K, p and $\overline{p}$.

In this analysis, we use the simulated data generated by STAR spin group, which is sampled according to the initial parton p_T intervals: (0,2),(2,3), (3,4), (4,5), (5,7), (7,9), (9,11), (11,15), (15,25), (25,35), (>35) using PYTHIA version6.205 with MSEL = 1. For good association between MC track and reconstructed track, the commonhits, *i.e.* same hit in simulation and reconstruction, is required larger than 10, and some other cuts for track quality are required same as in our real data analysis. Tab. 3.5 shows cuts in this simulation analysis.

In order to fully cover the p_T range in our analysis, the spectrum in different parton p_T range are weighted by the cross-section simulated through the PYTHIA, and the details are following. Firstly, we select parton p_T in (2,3) as our reference. Secondly, we calculate

Table 3.6: Cross-section and number of events in different parton p_T bin from simulation.

p_T(GeV/c)	cross-section (mb)	Number of events
(0,2)	18.233	339083
(2,3)	8.11	507996
(3,4)	1.295	400629
(4,5)	0.3144	600980
(5,7)	0.136	431000
(7,9)	0.02312	412000
(9,11)	0.00551	416000
(11,15)	0.002222	416000
(15,25)	0.0003888	408000
(25,35)	1.018e-5	380000
(>35)	5.3e-7	100000
minbias	28.12	

the weighted factor as:

$$W_i = \frac{\sigma_i}{\sigma_0}\frac{N_0}{N_i}, \tag{3.10}$$

where σ_i and N_i are the cross-sections and number of events in i-th bin respectively, and σ_0 and N_0 are for the reference parton p_T bin. Tab. 3.6 shows cross-section and number of events in different parton p_T bin.

With the factor W_is, weighted pion spectra in different parton p_T bin are shown on left plot in Fig. 3.14 in different color circles. Also, the overall pion spectra are summed as minimum bias results shown as black crosses. By dividing the summed pion spectra, fraction distributions in different parton p_T bin are shown in the right panel in the Fig. 3.14 to describe different contributions in different parton p_T bin. However, this method results in the worthless statistic errors due to different contribution in each parton p_T bin.

Fig. 3.15 shows the p_T dependence of tracking efficiencies in different parton p_T range. To derive an uniform expression, we fit these distributions with Eq. 3.11 for each parton p_T bin, and all those fit curves are shown on the last panel in Fig. 3.15.

$$f(p_T) = [0] + \exp([1] + [2] * p_T), \tag{3.11}$$

There are small difference (less than 5% of efficiency) between different parton p_T bin from last plot in the Fig. 3.15. In order to understand this, multiplicity and η dependence of efficiencies in all parton p_T bin are studied and shown in Fig. 3.16 and Fig. 3.17. This study indicates that there are no dependence on η and multiplicity distribution. Therefore, we set the difference as systematic errors, which are included in systematic errors.

Finally, the tracking efficiency for pion with weighted contribution of each parton p_T bin are shown in the Fig. 3.18. Proton and kaon efficiencies can be extracted with the same way, and similar values at high p_T let us use pion efficiency to correct proton and kaon spectra later.

3.6 Background correction

To obtain primary pions, background from K^0_S feed-down was studied and ∼5% contribution was removed from pion results at high p_T. The details can be found from [Rua05, Ada06b]. For proton and anti-proton, we present their inclusive production without hyperon feed-down correction in this dissertation, because there are no enough statistics for hyperon at high p_T to obtain the percentage of decayed proton [Ada06b, Ada05e, Abe07c]. However, the hyperon contribution to inclusive proton (anti-proton) yields was studied to be less then 25% at high p_T from [Ada06b, Abe07c].

3.7 Other checks

To double-check if there is residual trigger bias in our results, HT1, HT2 and JP1 triggered data are analyzed as well. With dE/dx information, we identify particles and get their raw counts in these triggered events with the same way we used in JP2 triggered events. Then, their yields are corrected with the corresponding trigger enhancement factors, which are shown in the Fig. 3.19. p_T dependence of trigger enhancement for charged pions is shown as colored open circles, and for the combined charged, shown as black solid points, are described by Landau function, which are shown as dashed lines

on the same figure. After trigger enhancement correction, there are still discrepancies of charged pion spectra in different triggers, especially at low p_T range.

To resolve the discrepancy, we check the trigger enhancement factors in all triggered events firstly. It can be seen from the Fig. 3.19, there are a few data points jumped a lot from one to next one, which are far away from the fitted curves. However, their errors can not describe their differences, since pion spectra from simulation are obtained from weighted spectra in different parton p_T, and their errors are non-physical. Therefore, we try to make the error larger for some jumped data points, and then fit these data to get more reasonable fit curves which are used into spectra correction. The Fig. 3.20 shows the trigger enhancement factor versus p_T with a few artificial errors and new fit curve.

After correction, spectra in different triggered events are compared by taking ratios of spectra in HT1, HT2, JP1 triggered events to spectra in JP2 triggered events. These ratios are shown in the Fig. 3.21, which indicates that charged pion spectra in HT2 triggered events with threshold energy $E_T > 3.5$ GeV are consistent with results in JP2 triggered events with higher energy threshold, while pion spectra in JP1 and HT1 are higher than that in JP2 significantly. This may be caused by different energy threshold in different trigger. For example, it's more easier to trigger on HT1 and JP1 events with low energy thresholds than to trigger HT2 and JP2 events with high energy thresholds by noisy backgrounds. Another possibility is that we may ignore some corrections, which need to be explored in the future.

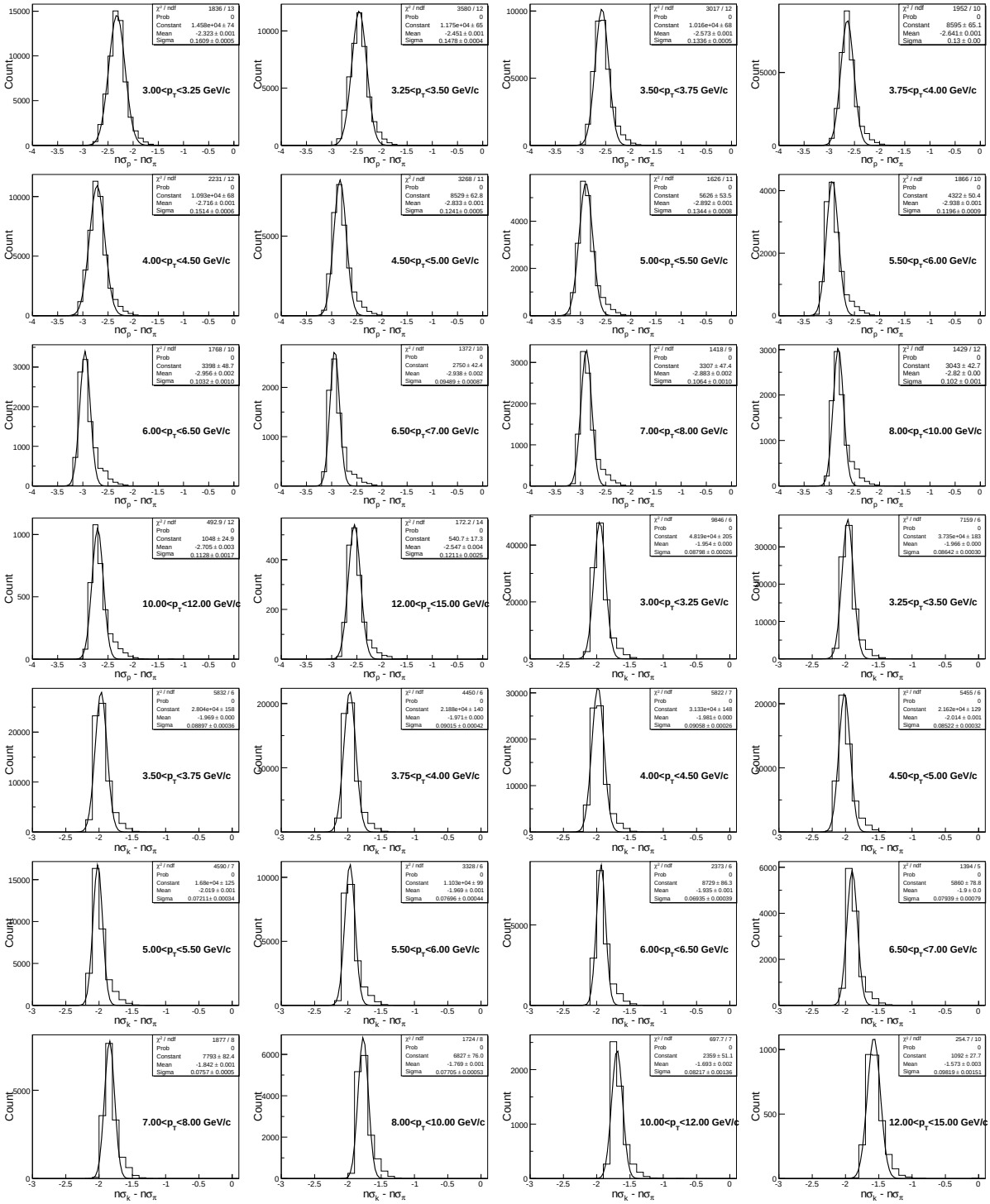

Figure 3.7: $n\sigma_p$ - $n\sigma_\pi$ and $n\sigma_K$ - $n\sigma_\pi$ distributions fitted by Gaussian at each p_T slice.

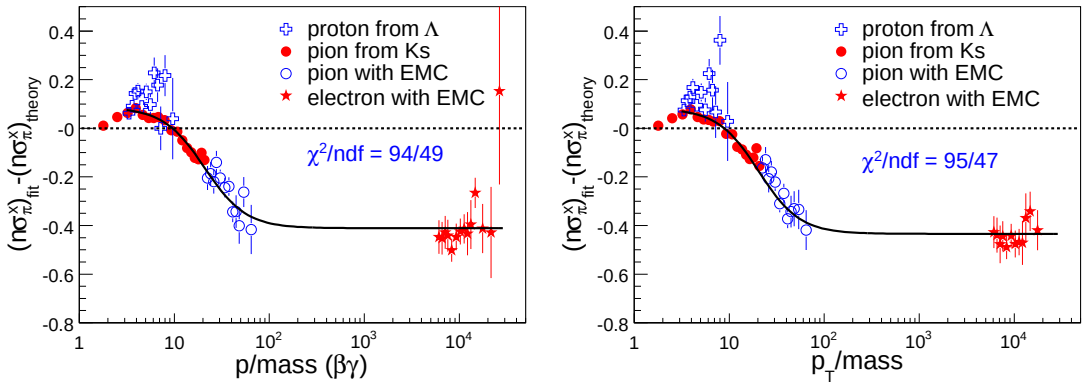

Figure 3.8: The dE/dx deviation in σ of pion (circles), proton (crosses) and electron (stars) as function of $\beta\gamma$ (left) and transverse momentum divided by mass (right).

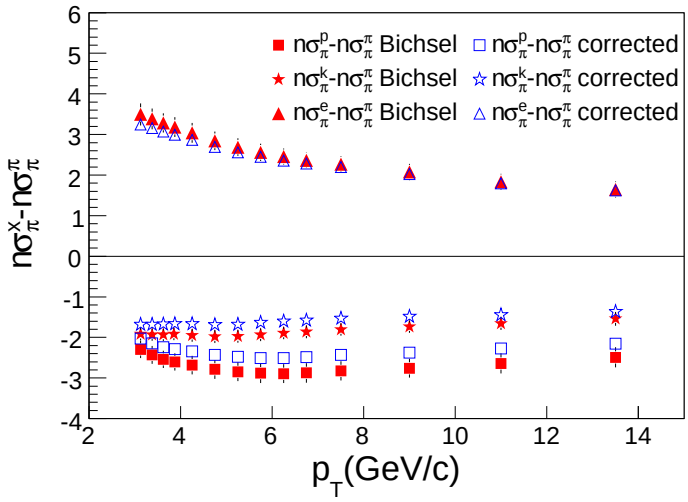

Figure 3.9: Comparison of the relative dE/dx peak position of $n\sigma_\pi^K$, $n\sigma_\pi^p$, $n\sigma_\pi^e$. All solid dots depict theoretical values, and open ones are re-calibrated results.

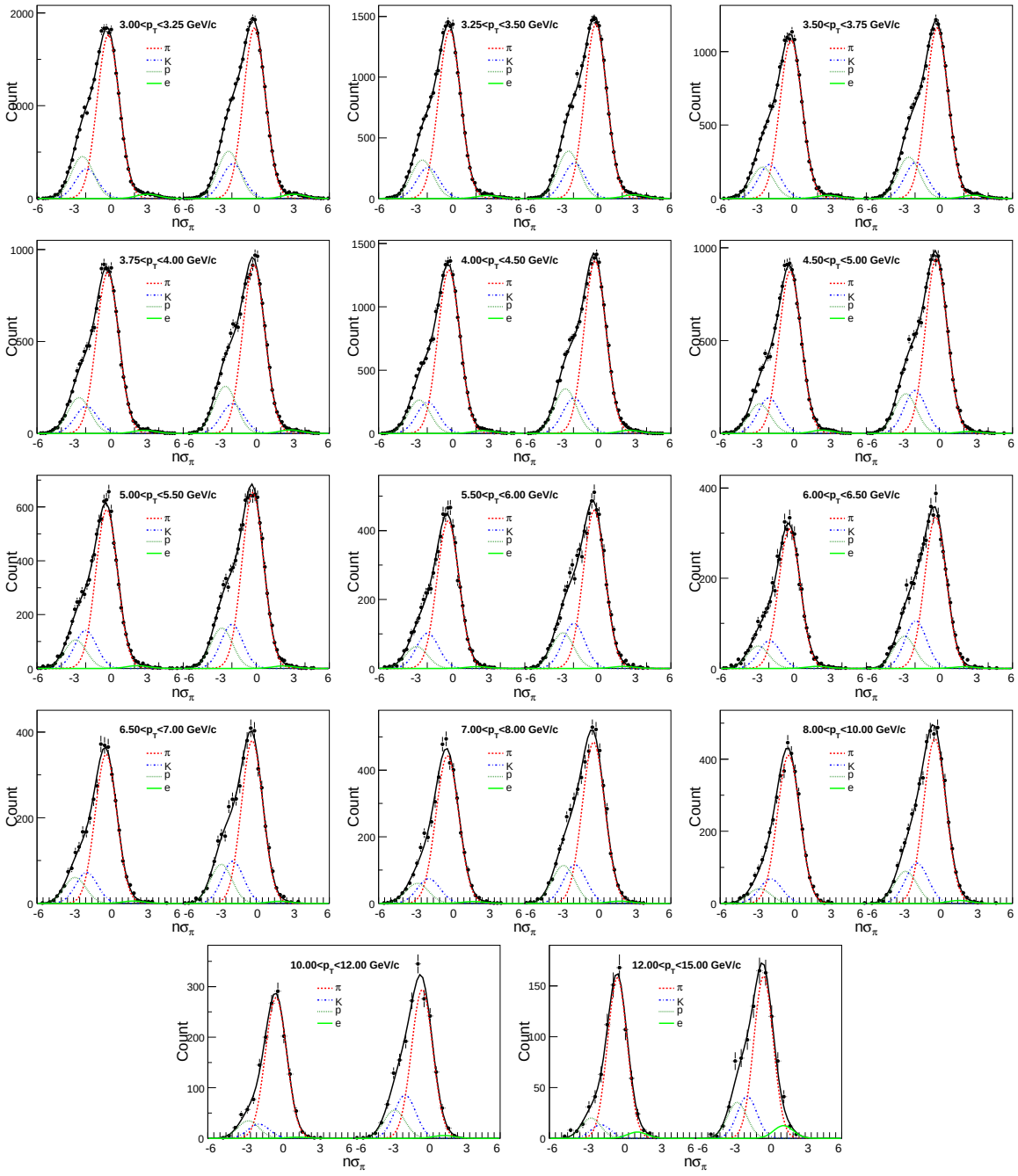

Figure 3.10: dE/dx distribution at different p_T range. Eight Gaussian functions are used to describe each particle contribution. For example, the red line is pion, dashed green line is proton, blue line is kaon and the light green line is electron.

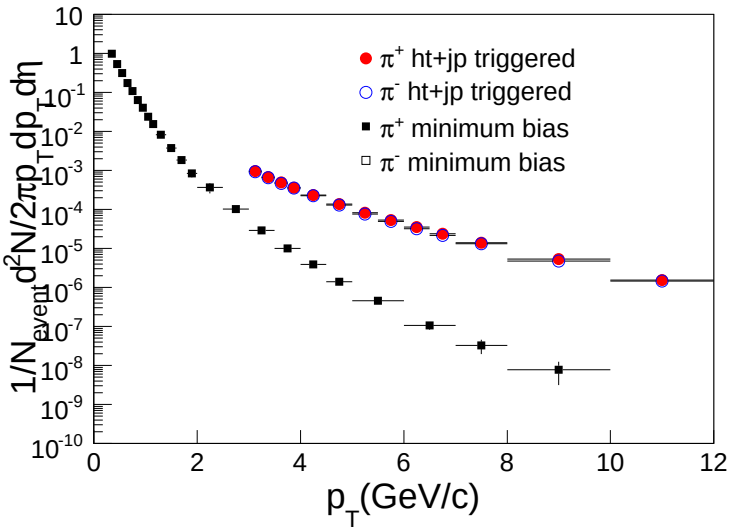

Figure 3.11: pion invariant yields vs p_T in minimum bias and EMC triggered events.

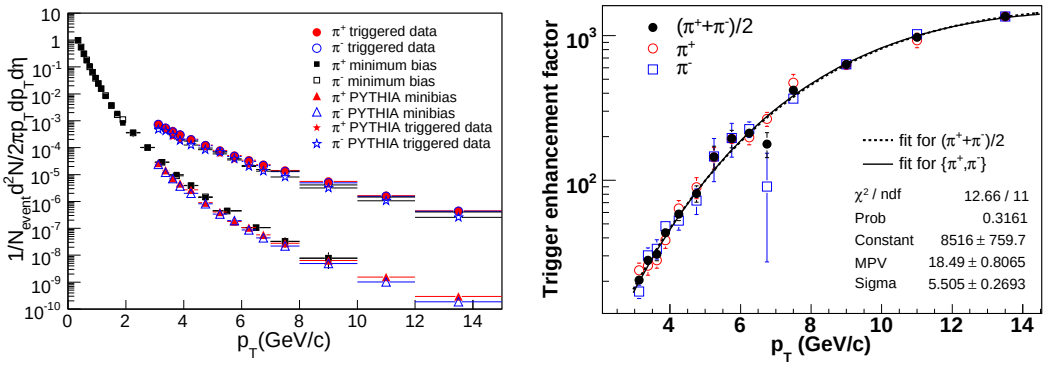

Figure 3.12: The left panel shows pion spectra in minimum bias and the BEMC triggered events from both measurements and the PYTHIA+GEANT simulation. Triggered efficiency from the simulations versus p_T distribution is shown on the right panel.

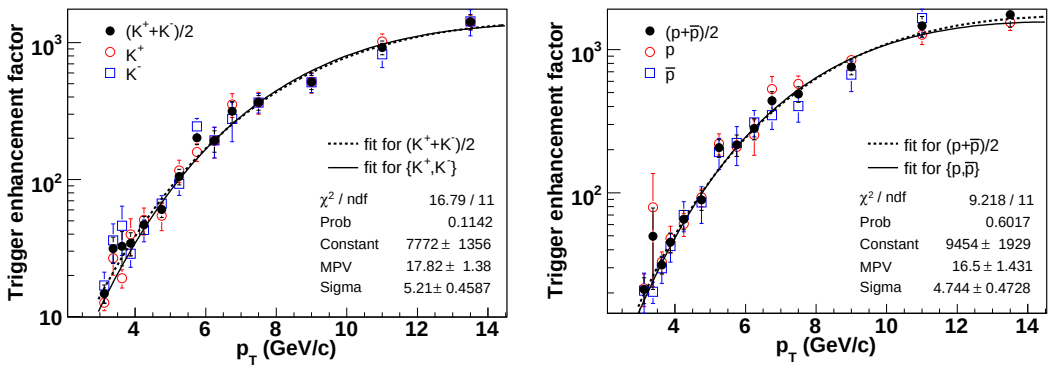

Figure 3.13: Trigger enhancement factor distribution for kaon and proton are shown on the left panel and right panel respectively.

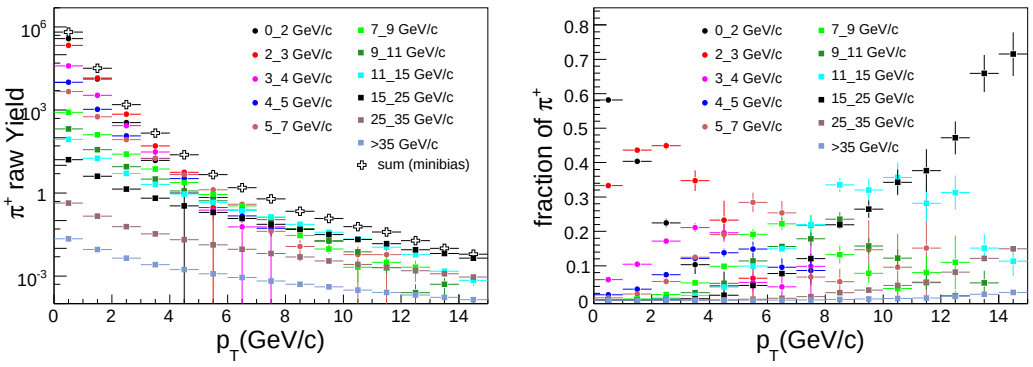

Figure 3.14: Left panel shows weighted positive pion raw yields vs p_T in different parton p_T bin and minimum bias. On the right panel, the fraction in different parton p_T versus p_T distribution are shown.

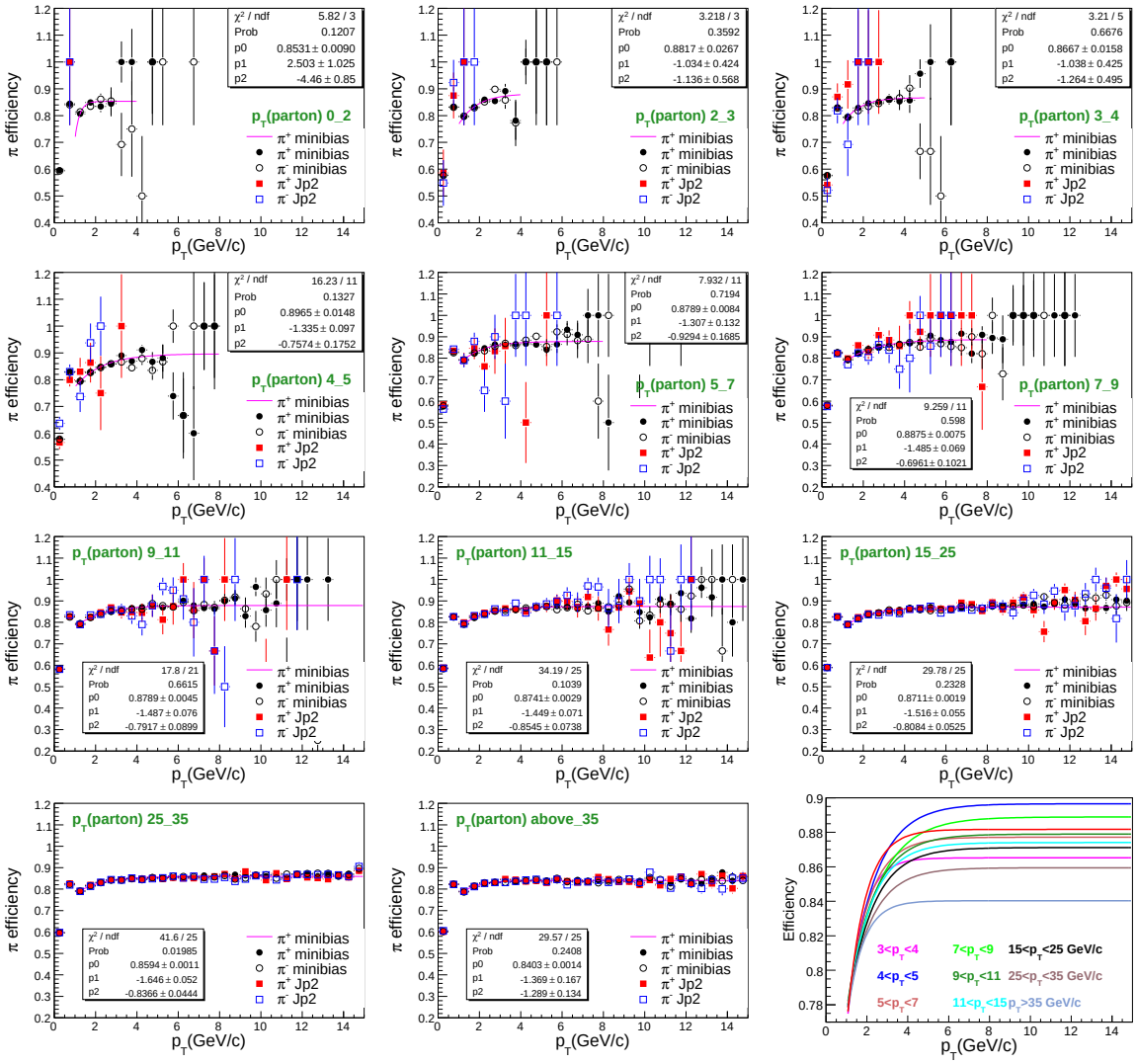

Figure 3.15: Efficiency versus p_T at different parton p_T range.

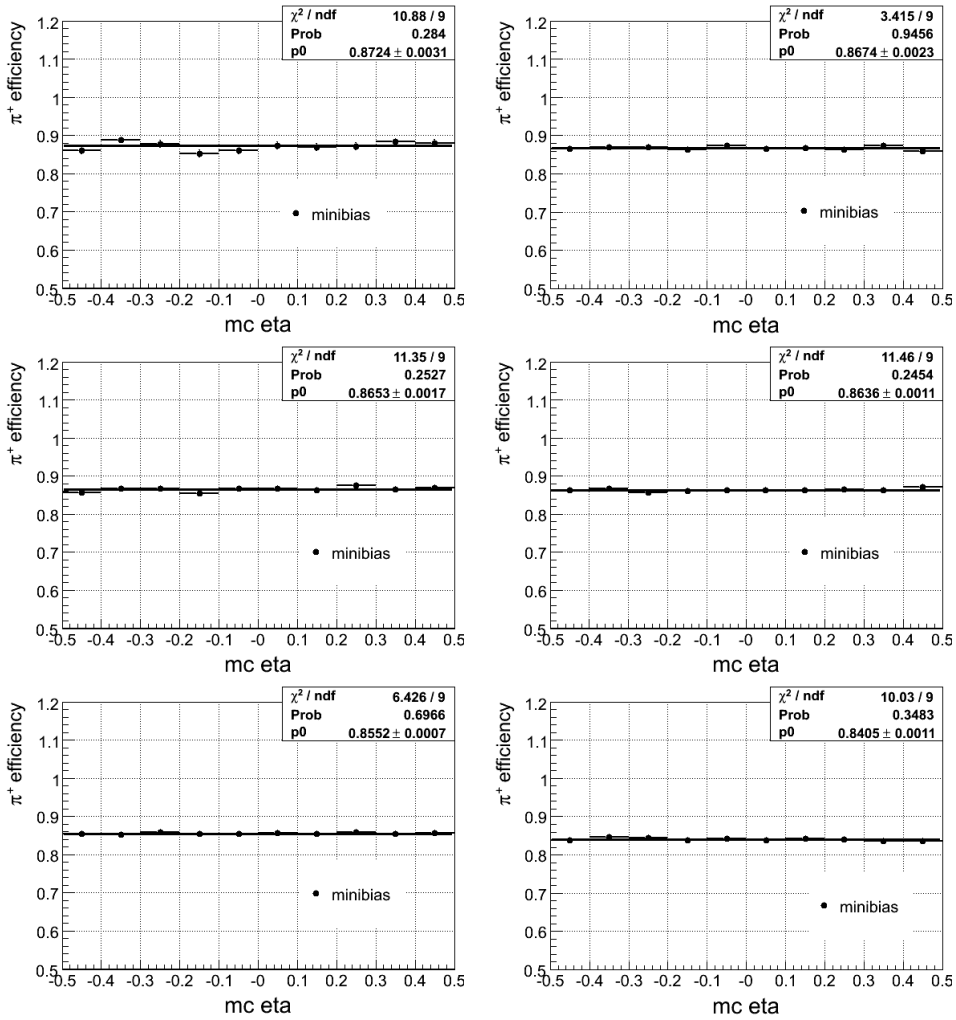

Figure 3.16: Efficiency versus η at different parton p_T range.

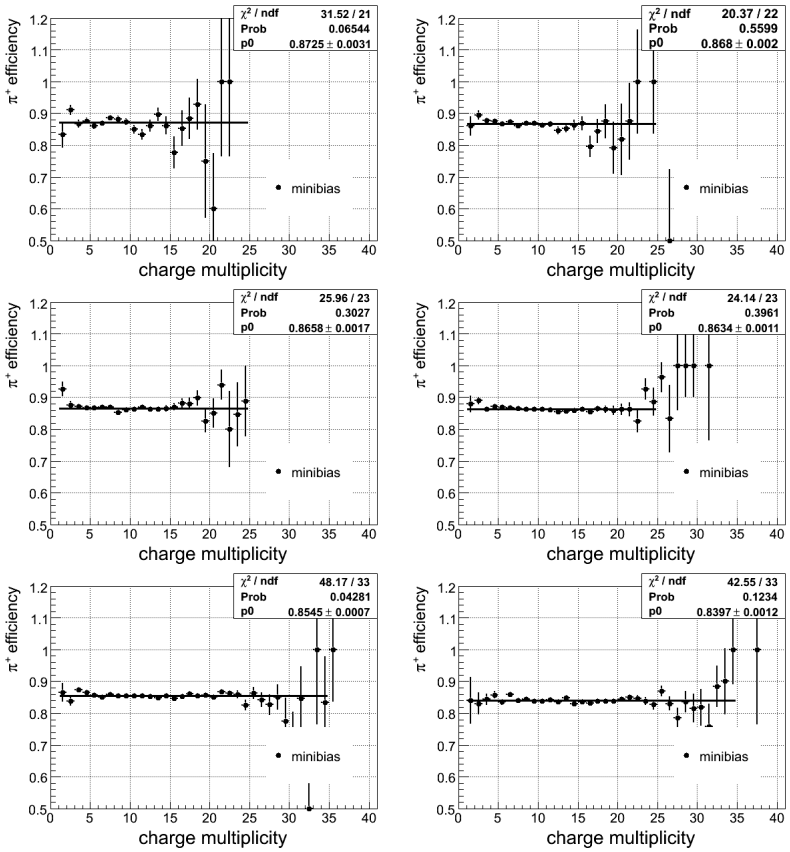

Figure 3.17: Efficiency versus multiplicity at different parton p_T range.

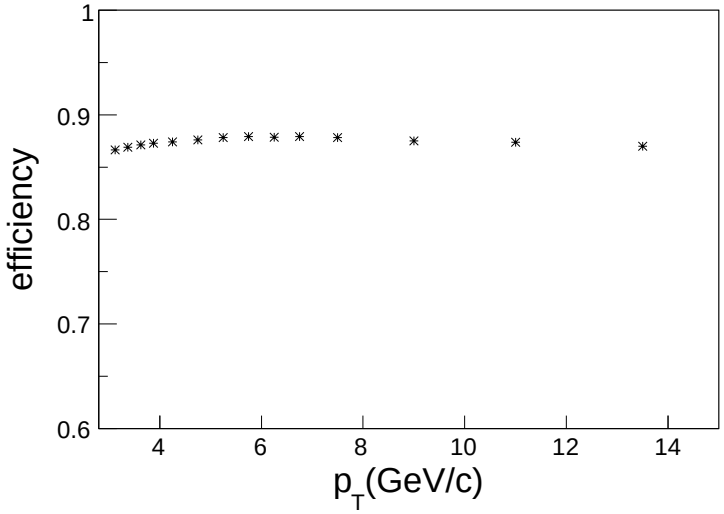

Figure 3.18: pion efficiency versus p_T distribution.

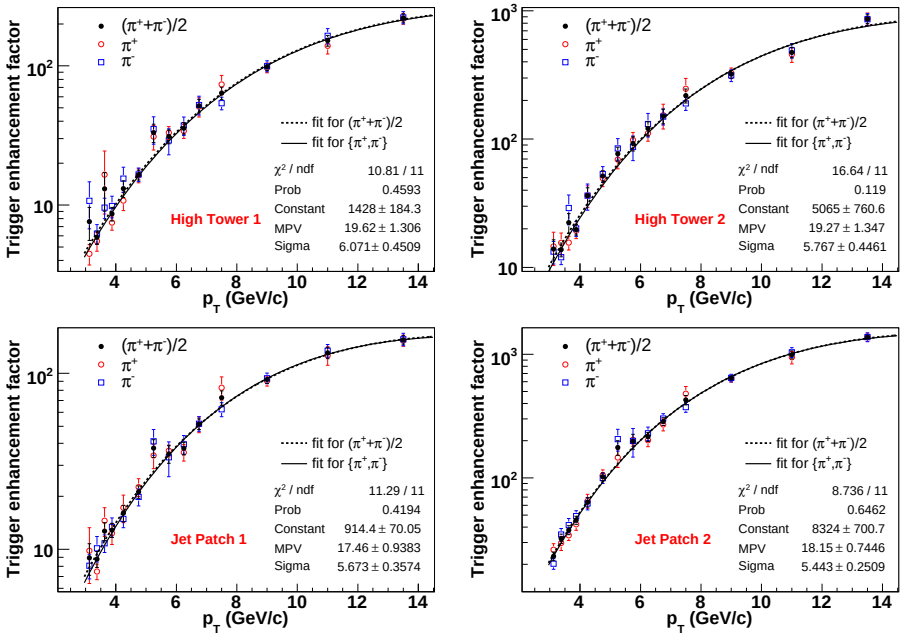

Figure 3.19: Trigger enhancement trigger versus p_T distribution for HT1 (left upper panel), HT2 (right upper panel), JP1 (left lower panel) and JP2 (right lower panel).

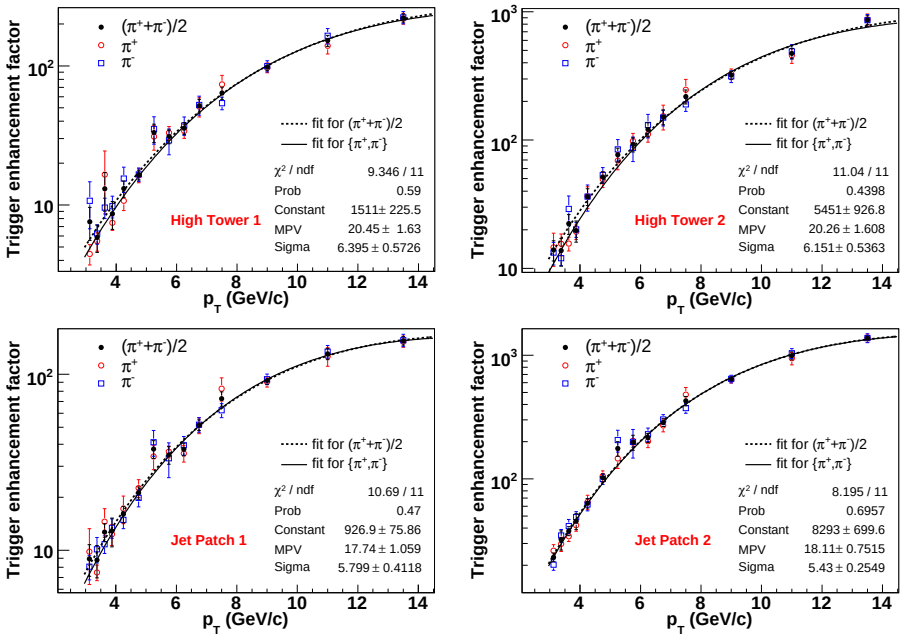

Figure 3.20: Trigger enhancement trigger versus p_T distribution for HT1, HT2, JP1 and JP2 as in the Fig. 3.19, but artificial error bar are added to the first two data points to get more reasonable fit curve.

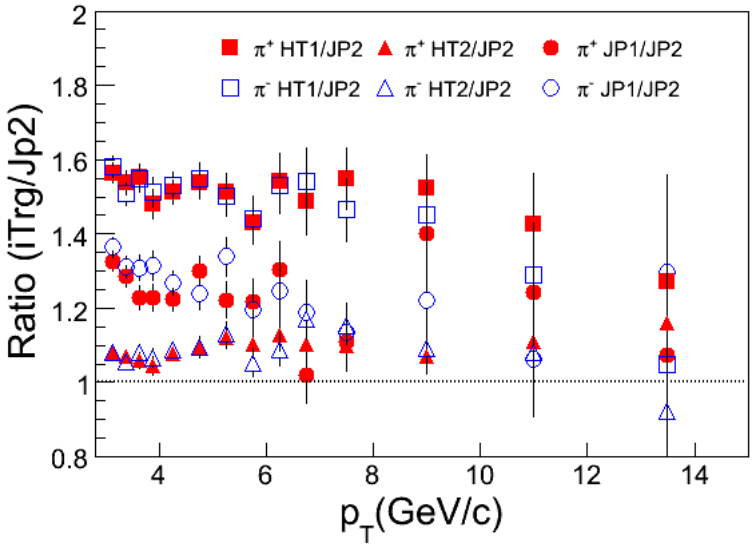

Figure 3.21: The ratios of charged pion production in HT1, TH2 and JP1 triggered events to that in JP2 triggered events.

CHAPTER 4

Charged particle identification in Au+Au collisions at $\sqrt{s_{NN}} = 200$ GeV

To obtain kaon yields and reduce the systematic uncertainties for previous published pion, proton yields in Au+Au collisions [Abe06], we apply the re-calibration method for dE/dx information in Au+Au collisions as we did in p+p collisions. This chapter shows results of the dE/dx re-calibration and spectra of charged hadrons in Au+Au collisions.

4.1 Data Sets and cuts

In order to do this analysis, we analyze ∼21.2 Million central triggered events, which are triggered online by the ZDC coincidence corresponding to 0-12% cross-section (central centrality). Some cuts for track quality are required, such as $|\eta| < 0.5$, $p_T > 0.2$ GeV/c, nHitsfit ≥ 25, ndEdxpt ≥ 15, dca < 1 cm and so on.

4.2 Re-calibration

According to re-calibration in Chapter. 3, we re-calibrate the dE/dx for charged particles in Au+Au collisions. Firstly, the BEMC information are used to enhance electron yields relative to other particles, such as $0.3 < p/E < 1.5$, $n_\eta \geq 2$, $n_\phi \geq 2$, $\phi_{dist} \leq 0.01$ and $Z_{dist} \leq 2$ cm. Fig. 4.1 shows the normalized dE/dx distribution at different p_T range. An eight-Gaussian function is used to fit these distribution as before for deriving nσ_π peak positions of electrons and pions.

Secondly, K^0_S and Λ are reconstructed with topological cuts, and their invariant mass

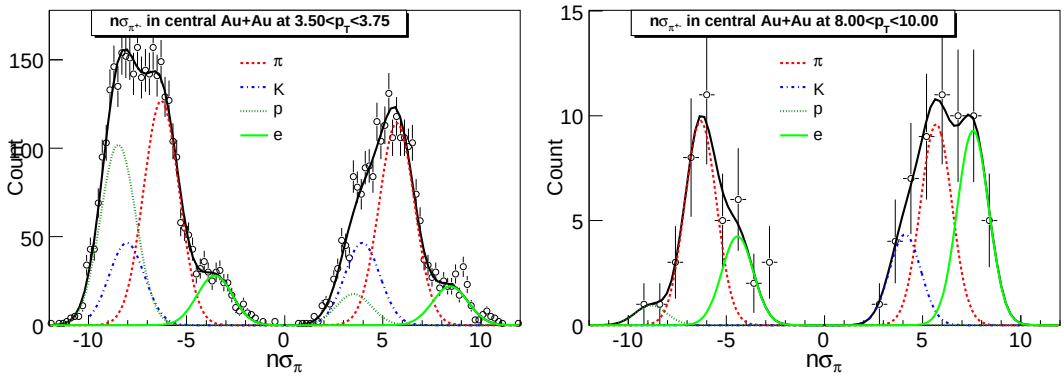

Figure 4.1: $n\sigma_\pi^h$ distribution with enhancement of electron and positron at $3.50 < p_T < 3.75$ GeV/c (left panel) and $8.0 < p_T < 10.0$ GeV/c (right panel) respectively, and 8-Gaussian function is used to fit these distributions.

distributions at different p_T bin are presented in the Fig. 4.2 and Fig. 4.3. Pure K_S^0 and Λ signals are selected with invariant mass cuts: $0.495 < \text{invMass}K_S^0 < 0.505$ GeV/c^2 and $1.11 < \text{invMass}\Lambda < 1.12$ GeV/c^2, and sequently their daughters are used to derive the precise peak positions $n\sigma_\pi^\pi$ for pions and $n\sigma_\pi^p$ for protons in Au+Au collisions. The Fig. 4.4 shows the $n\sigma_\pi$ distribution for pion from K_S^0 and proton (anti-proton) from Λ ($\overline{\Lambda}$), which are fitted by Gaussian and two-Gaussian function respectively. The widths for pion and proton are consistent with each other, and shown in the Fig. 4.5.

In order to double-check proton peak positions, which have big errors due to statistics and some contaminations from K_S^0 and Λ background, $n\sigma_\pi^{h^+} - n\sigma_\pi^{h^-}$ is filled in a histogram to figure out proton peak positions according to the yield asymmetry of p and $\overline{p}$. Fig. 4.6 shows the $n\sigma_\pi^{h^+} - n\sigma_\pi^{h^-}$ distributions at different p_T bin, which are fitted by Gaussian function shown as black curves. The fitted $n\sigma_\pi^p$ values at all p_T slices are consistent with the previous values from Λ decay, and shown as blue diamonds in the Fig. 4.7 later.

The Fig. 4.7 shows the results for the deviation for dE/dx in σ of pion (circles), proton (crosses) and electron (stars) as function of p_T divided by mass in Au+Au collisions on the left panel, and comparison of the relative dE/dx peak position of $n\sigma_\pi^K$, $n\sigma_\pi^p$, $n\sigma_\pi^e$ in Au+Au collisions on the right panel. The red stars represented electrons show large statistical uncertainties due to only 1/4 BEMC coverage in the run4 Au+Au collisions. With the Eq. 3.4, the deviations between experimental and theoretical values are fitted

Table 4.1: Fit parameters from momentum and p_T dependence of $n\sigma_\pi^x$ deviation in Au+Au collisions.

parameters	χ^2/ndf	A	B	C
p_T dependence	816.9/71	-0.361 ± 0.004	104.275 ± 3.779	281.073 ± 7.681

Table 4.2: Difference between $n\sigma_\pi^{K,p,e}$ and $n\sigma_\pi^\pi$ of theoretical values and re-calibrated results in Au+Au collisions. We note that an additional factor of 0.96 should be applied to the final separation in the table taking into the narrower width observed in the data.

p_T(GeV/c)	$n\sigma_\pi^K - n\sigma_\pi^\pi$ (fit/theory)	$n\sigma_\pi^p - n\sigma_\pi^\pi$(fit/theory)	$n\sigma_\pi^e - n\sigma_\pi^\pi$(fit/theory)
3.125	-1.6971/-1.4958	-2.0065/-1.7798	3.1039/2.9561
3.375	-1.7078/-1.5006	-2.1299/-1.8915	2.9990/2.8689
3.625	-1.7100/-1.5017	-2.2243/-1.9771	2.9027/2.7878
3.875	-1.7180/-1.5035	-2.2877/-2.0292	2.8129/2.7107
4.25	-1.7342/-1.5127	-2.3625/-2.0929	2.6884/2.6022
4.75	-1.7617/-1.5382	-2.4598/-2.1821	2.5185/2.4423
5.25	-1.7456/-1.5368	-2.5152/-2.2343	2.3799/2.3154
5.75	-1.7109/-1.5074	-2.5460/-2.2642	2.2645/2.2087
6.25	-1.6740/-1.4822	-2.5548/-2.2710	2.1697/2.1206
6.75	-1.6465/-1.4567	-2.5368/-2.2544	2.0854/2.0456
7.5	-1.5977/-1.4233	-2.4897/-2.2221	1.9954/1.9644
9	-1.5365/-1.3885	-2.4350/-2.1784	1.8305/1.8105
11	-1.4583/-1.3403	-2.3292/-2.0945	1.6189/1.6041
13.5	-1.3470/-1.2545	-2.1947/-1.9900	1.4349/1.4279

and shown as black curve on the left panel in the Fig. 4.7. The Tab. 4.1 shows the fit parameters. Then, the differences of $n\sigma_\pi$ of pion and other charged particles at each p_T bin from re-calibration and theory are listed in the Tab. 4.2.

4.3 Raw yields, efficiency, correction, systematic uncertainties

Raw yields of charged particles in Au+Au collisions can also be obtained by the $n\sigma_\pi$ distributions with fitting method and counting methods. Fig. 4.8 shows the $n\sigma_\pi$ distributions fitted by eight-Gaussian function at different p_T slices. By comparing the re-calibrated values at each p_T range, we found the differences among particles in Au+Au col-

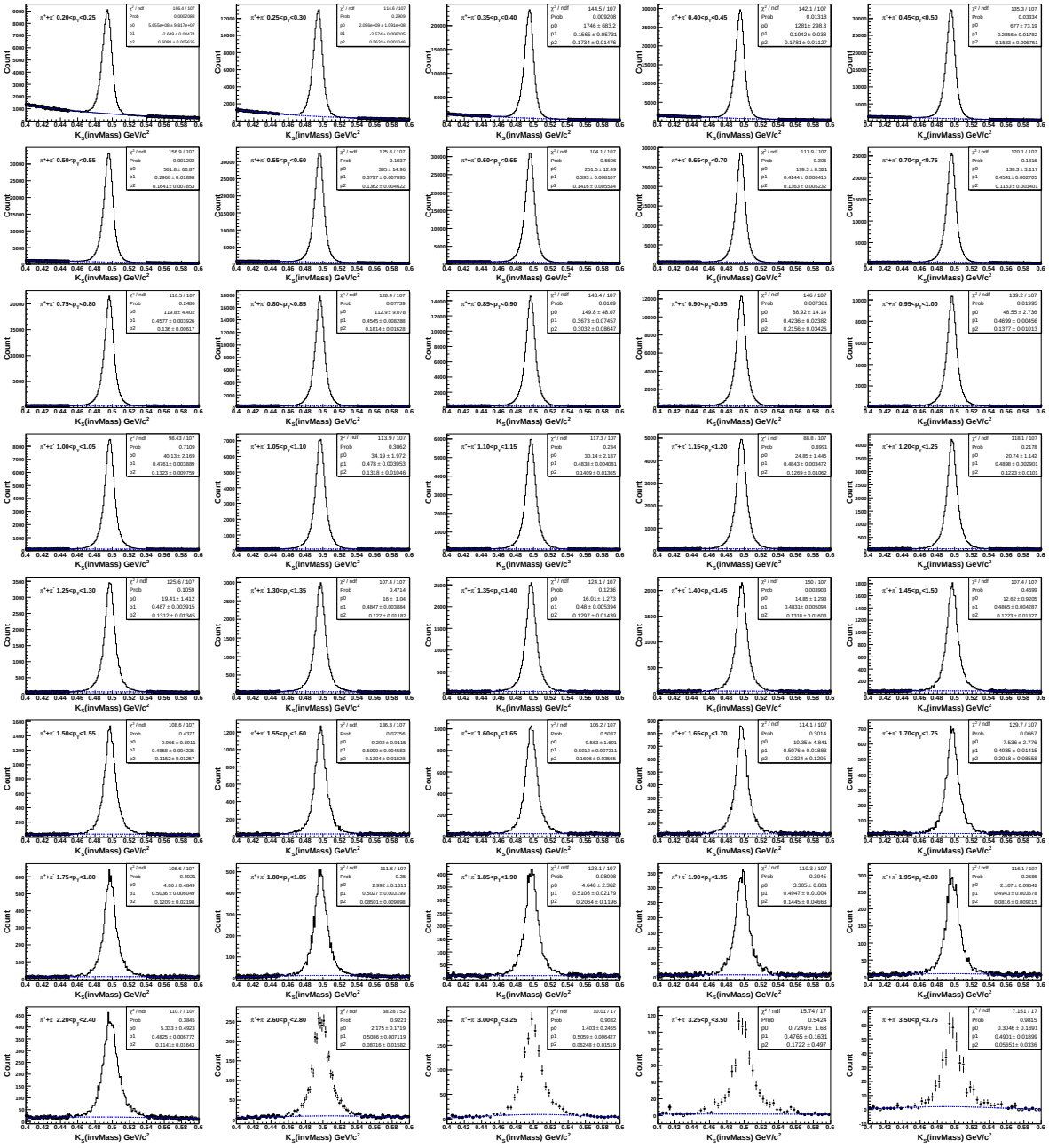

Figure 4.2: Invariant mass of K^0_S at each p_T range.

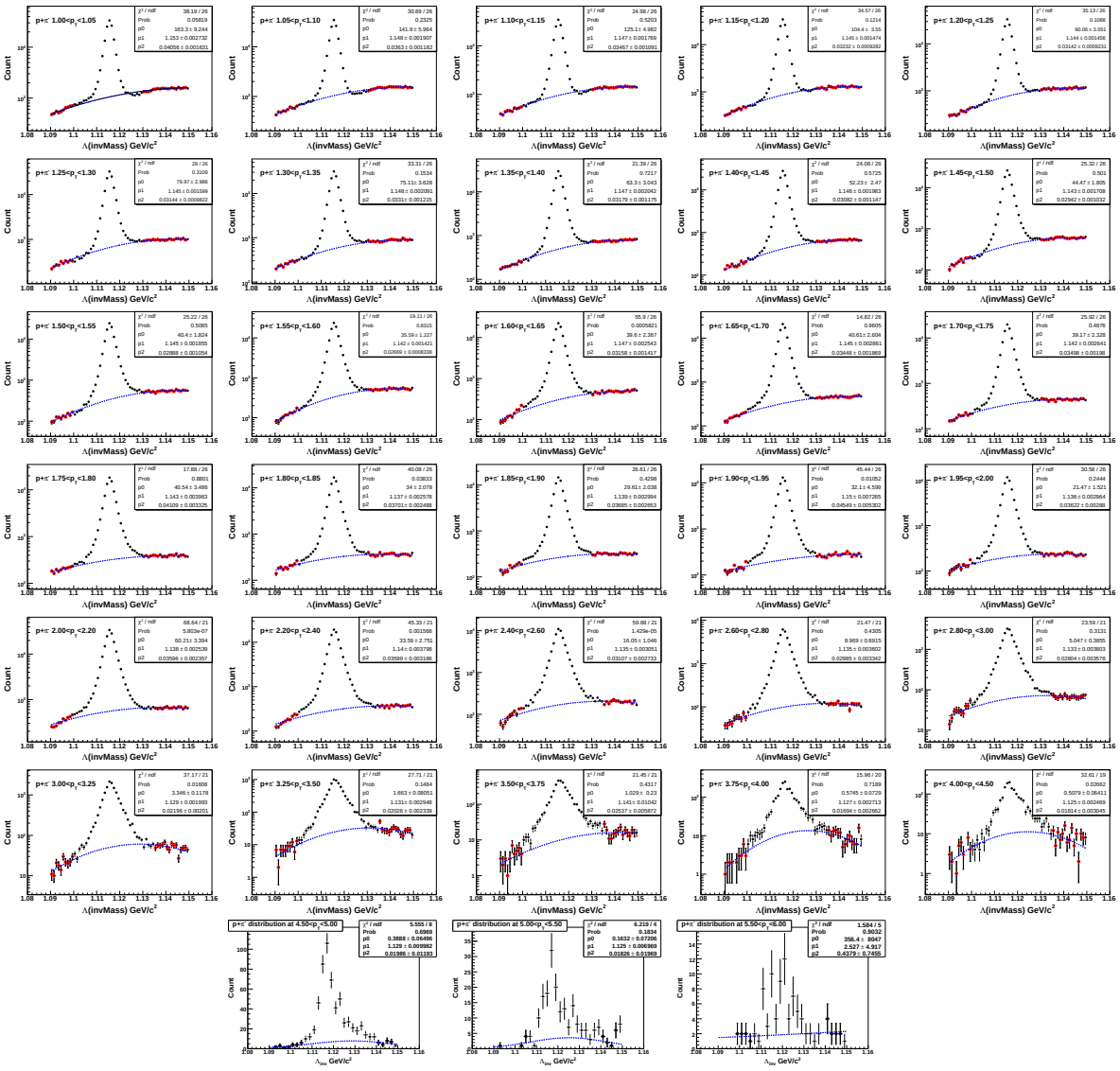

Figure 4.3: Invariant mass of Λ at each p_T range.

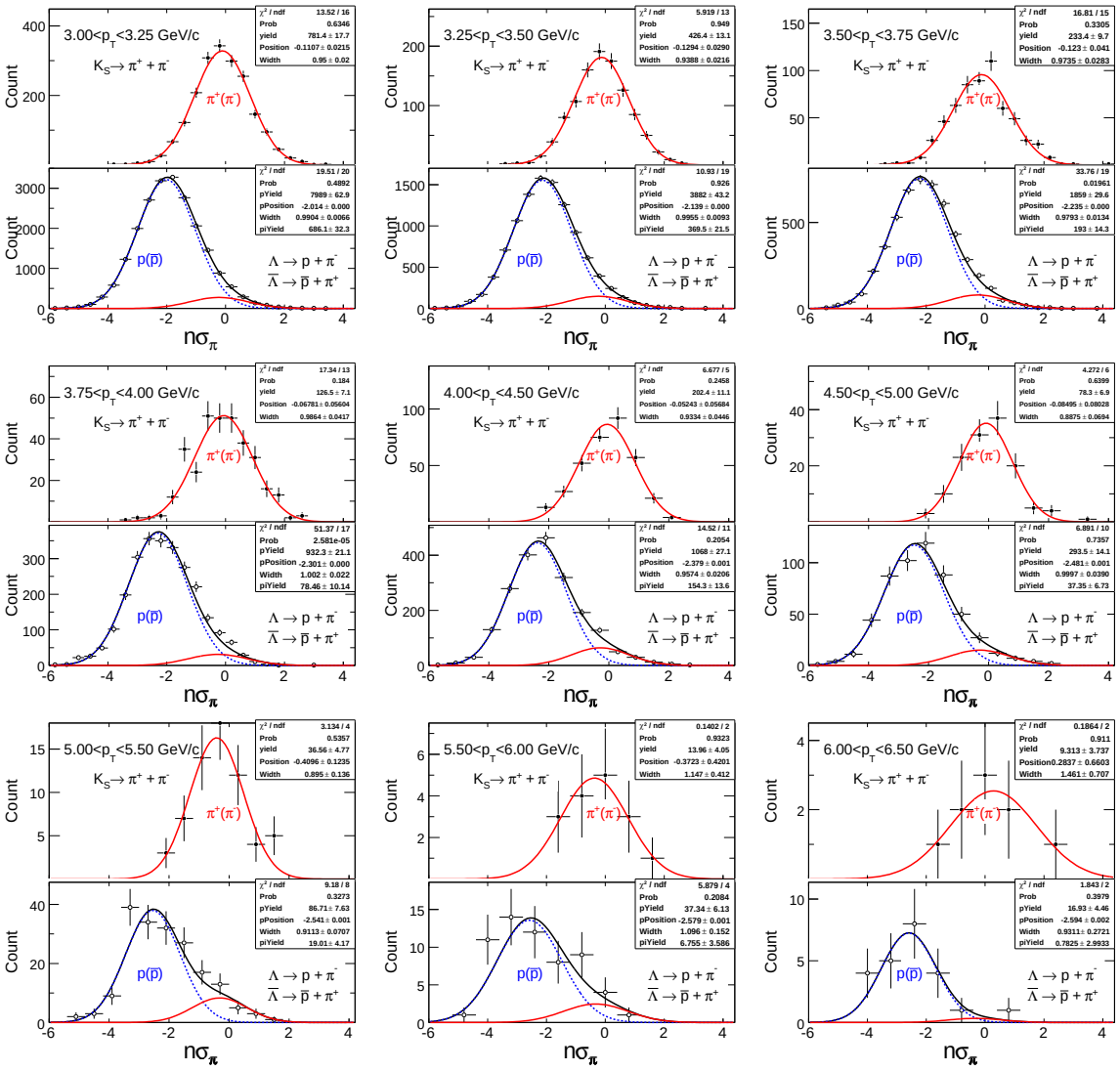

Figure 4.4: nσ_π distribution for pion decayed from K^0_S, and proton (anti-proton) decayed from $\Lambda(\overline{\Lambda})$ at each p_T range.

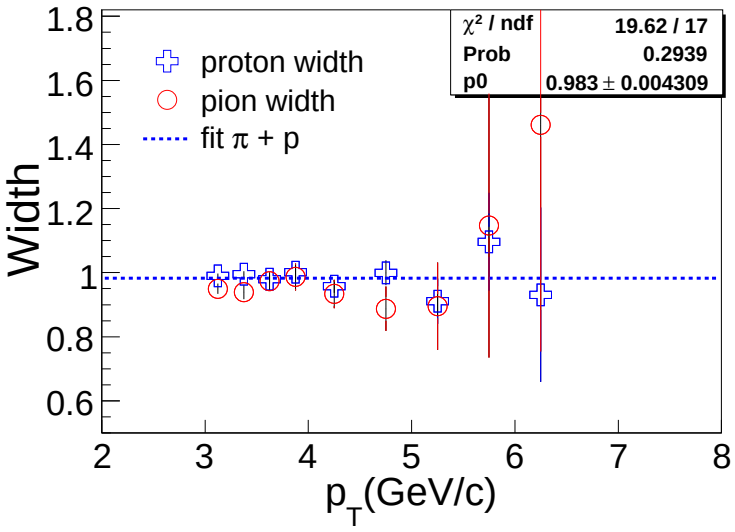

Figure 4.5: Width of $n\sigma_\pi$ versus p_T. will be updated for calibrated one

lisions are smaller than those in p+p collision. Besides, the widths of $n\sigma$ distributions in Au+Au collisions are larger than that in p+p system. This indicates that the dE/dx resolution in Au+Au is worse than in p+p collisions. Therefore, I just show results at $p_T > 6$ GeV/c, where particles can be separated well by $n\sigma_\pi$ relative to low p_T range. To correct detection efficiency, previous studies in Au+Au collisions [Abe06] are applied by Eq. 4.1:

$$[0] * exp(-pow([1]/x, [2]), \tag{4.1}$$

where [0], [1], [2] are 0.7938, 0.1555, 0.9108, respectively obtained from previous study [Rua05] and used in this analysis.

In addition, ∼4% pions from K^0_S feed-down are corrected to obtain primary pion yields. For study of systematical uncertainties, the main source, dE/dx uncertainties are taken first, which are shown in the Fig. 4.9. This figure shows the difference of deviations in σ between data and fit function as a function of p_T, and the upper and lower lines are taken as limits of uncertainties in our analysis by shifting dE/dx peak position left and right with this value. In addition, 0.05, and 0.1 σ are also done to study the uncertainties.

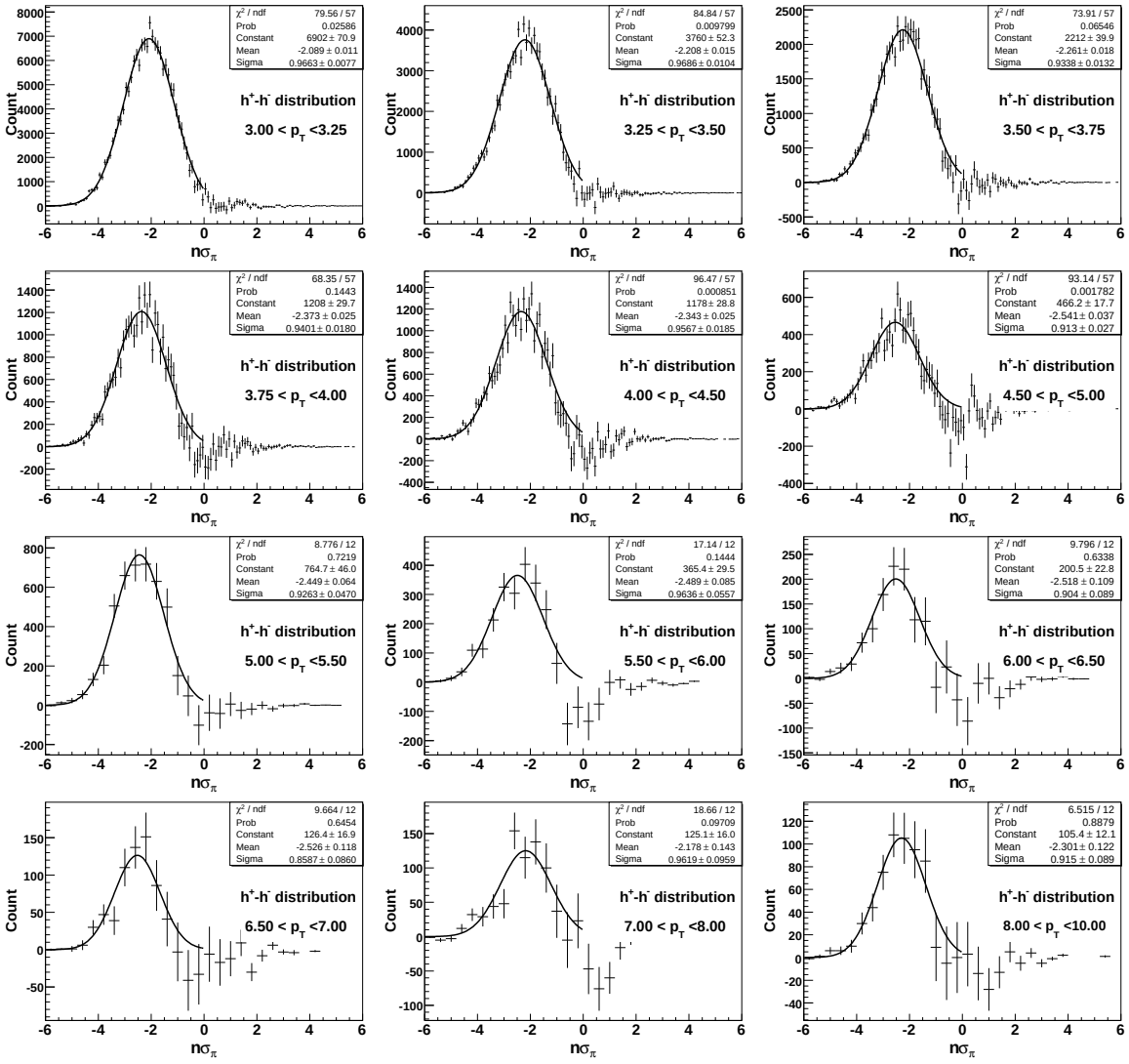

Figure 4.6: The difference of nσ distribution between positive particles and negative particles at each p_T slice, $n\sigma(h^+) - n\sigma(h^-)$. Gaussian is used to fit the peak for proton.

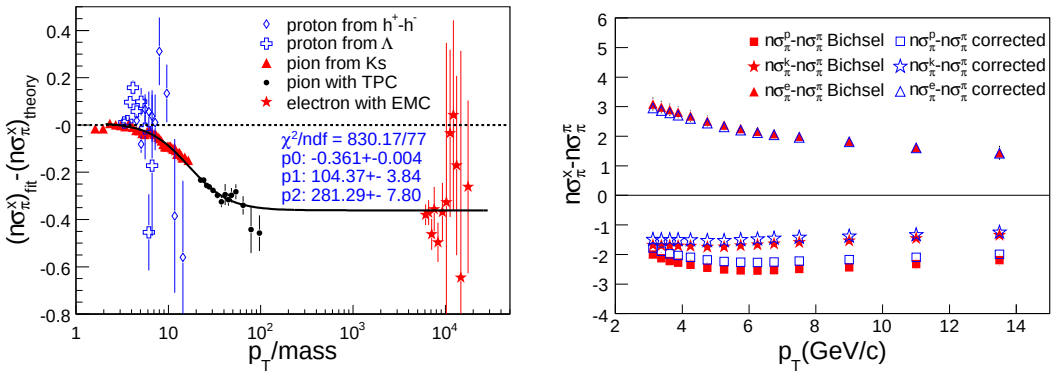

Figure 4.7: On the left panel, dE/dx deviation in σ of pion (circles), proton (crosses) and electron (stars) as function of p_T divided by mass in Au+Au collisions. On the right panel, comparison of the relative dE/dx peak position of $n\sigma_\pi^K$, $n\sigma_\pi^p$, $n\sigma_\pi^e$ in Au+Au collisions, and all solid marks depict theoretical values and open marks represent re-calibrated results.

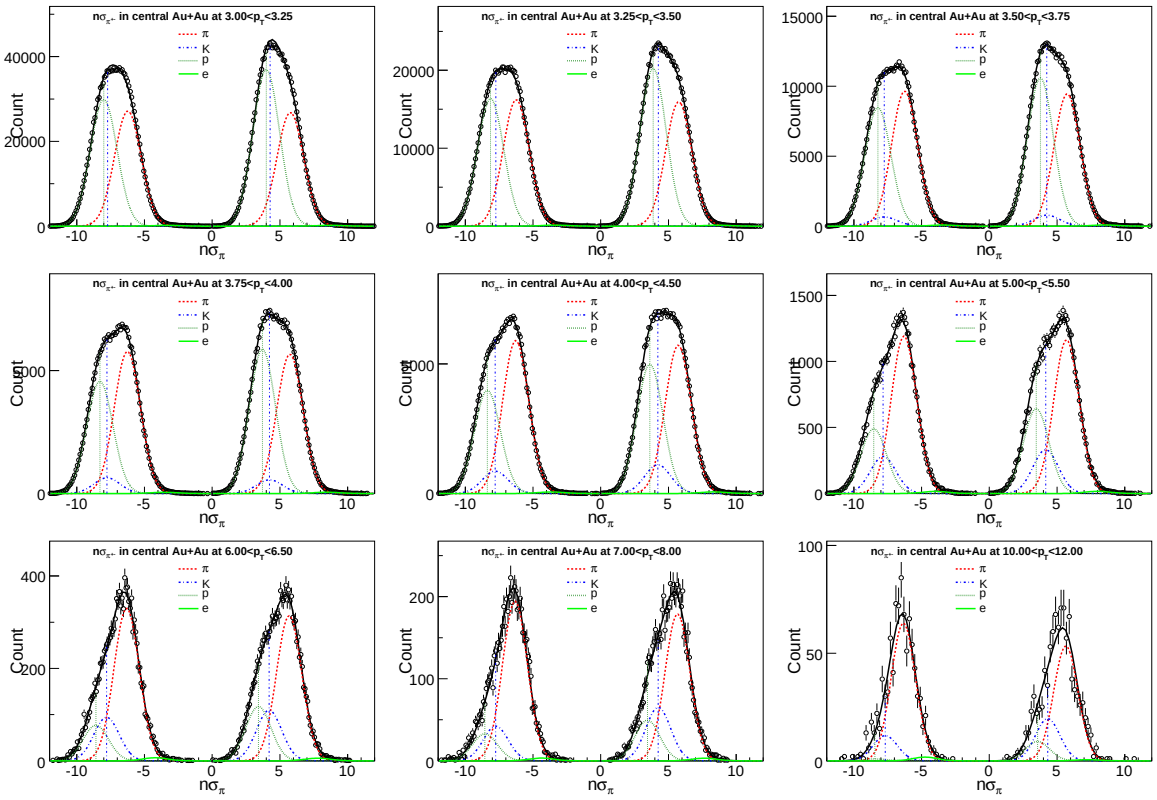

Figure 4.8: dE/dx distribution in each p_T bin and fit by eight-Gaussian function with fixed all peak positions, derived from Fig. 4.7.

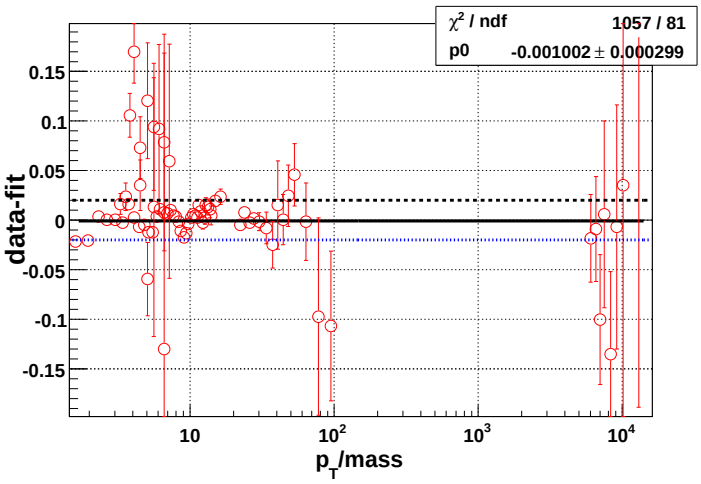

Figure 4.9: The difference between data points and our fit curve on the left panel in the Fig. 4.7.

CHAPTER 5

Neutral K^0_S and Λ reconstruction in p+p collisions at $\sqrt{s_{NN}} = 200$ GeV

The K^0_S can be reconstructed by the STAR detector at RHIC through $K^0_S \rightarrow \pi^+ + \pi^-$ decay mode. Up to now, STAR collaboration has published K^0_S measurements [Abe07c], which was limited to 5 GeV/c due to statistics in minimum bias triggered events. We have developed a new method to reconstruct K^0_S with one daughter π triggered by the BEMC and the other identified by the TPC, *i.e.* *"TPC+BEMC"*. Using the BEMC triggered data, we extended K^0_S measurements up to high-p_T, which also provide a way to cross-check trigger bias for our previous charged kaon measurements in JP2 triggered events by comparing K^0_S at near side and charged kaon at away side of the trigger. This chapter is dedicated to describe the details.

5.1 Data Sets and trigger

Since the event rate at RHIC is much higher than the DAQ rate of the slow detector TPC, the BEMC is taken as fast trigger detector to select/enhance events with high energy electrons, photons and hadrons. Through the EMC-triggered hadrons, we would reconstruct high-p_T K^0_S with higher statistics through its two charged pions decay with branching ratio 68.6%. To obtain more K^0_S in high p_T range, the data used for this analysis are collected from year 2005 p+p runs with energy threshold 2.5 GeV (HT1) and 3.4 GeV (HT2) respectively, which have been introduced in Chapter. 3. The integral luminosity are 0.65 pb^{-1} and 2.83 pb^{-1}, respectively. About 5.1 million HT1-triggered events and 3.4 million HT2-triggered events pass the vertex cut $|V_z| < 100$ cm.

5.2 Particle Identification (PID)

Two daughter pions are identified by the main detector TPC by the dE/dx information. To overcome the relatively low trigger efficiency, we did not require both of the daughters are triggered by the BEMC. Since the two pions decay from K^0_S are quite symmetry, it is sufficient to get high-p_T K^0_S by only requiring one daughter triggered by the BEMC. Both of the daughters are required to pass some general track quality cuts to ensure that they are good tracks and have reasonable dE/dx resolutions. We also require the triggered daughters to pass some EMC-related cuts to ensure they are really triggered.

5.2.1 Track selection

As we discussed in Chapter. 3, charged particles can be separated by the ionization energy loss dE/dx in the TPC. Fig. 5.1 shows the dE/dx distribution as a function of momentum in p+p collisions. The curves are expected values calculated by the Bichsel-function. The equivalent variable $n\sigma_\pi$ distributions are shown on the right panel of the Fig. 5.1, where we can see clear separation between π, K, $p(\overline{p})$ and e at low p_T (p_T< 1 GeV/c) and high p_T (p_T> 2.5 GeV/c. To obtain relative pure pion sample and reduce mis-identified background, we use $|n\sigma_\pi| < 2$ in this analysis. In order to select tracks with good resolution, the number of dE/dx hits included in the truncated mean method is required to be $\geq$ 15. For good quality of global tracks, number of hit fits is required larger than 15, psudo-rapidity is less than 0.5 and larger than -0.5, and p_T is larger than 0.2 GeV/c due to the magnetic field and the radius of the TPC. More details for selection are listed in the following Tab. 5.1.

5.2.2 Triggered track

When a charged particle with high energy goes through the BEMC (a thick absorber), it loses energy through virtual photons by interacting with Coulomb Field - bremsstrahlung. The loss energy is in inverse proportion to the mass square of projectile.

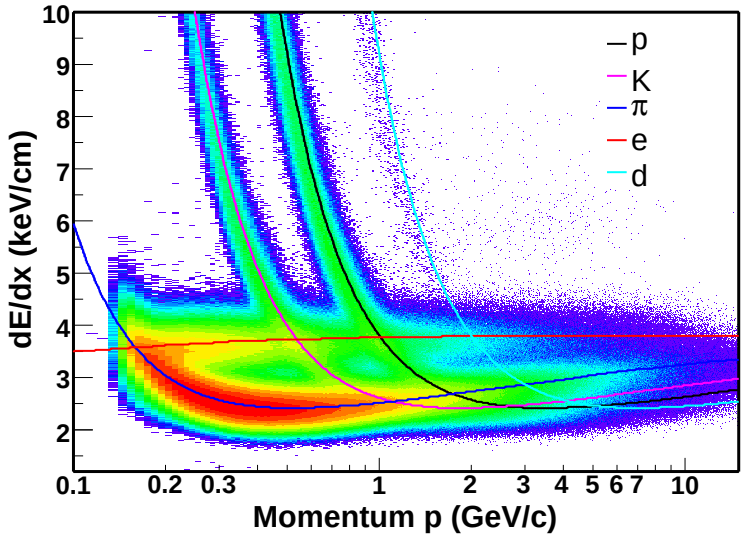

Figure 5.1: The dE/dx distribution as function of momentum in p+p collisions.

Therefore, the electron with smallest mass in charged particles should lose much more energy in bremsstrahlung than other charged particles, such as $\pi^{\pm}$, $K^{\pm}$, p and $\overline{p}$ and so on. The consequence of the radiated photon can be continued to produce electron and position pair, which may interact with medium by bremsstrahlung again. Then the iterations of these processes are continued until the energy of de-gradated electron less than the critical energy of pair-production. This phenomenon is called electro-magnetic process. Due to the difference of energy loss features of electrons (positions) and charged hadrons, the BEMC can separate electron and charged hadrons by their cluster size.

To obtain triggered track, we match the TPC track to the BEMC hits by extrapolating charged track out to the BEMC tower, and then calculate the distance between projected positions of charged particles and the center of the triggered tower recorded by online trigger in ϕ - η directions. Fig. 5.2 shows the distance in ϕ ($\Delta\phi$) and η ($\Delta\eta$) respectively as a function of p_T, and we select tracks with $|\Delta\phi| < 0.075$ and $|\Delta\eta| < 0.075$ respectively, which are one and half tower size in ϕ and η direction.

Since a significant fraction, ~30 - 40%, of charged hadrons with high energy do not deposit enough energy in STAR BEMC via the electro-magnetic process, and only deposit $\sim$ 250 - 350 MeV of equivalent energy in the calorimeter due to ionization energy loss. These hadrons are called "Minimum Ionizing Particles" (MIP) producing "MIP hits" in

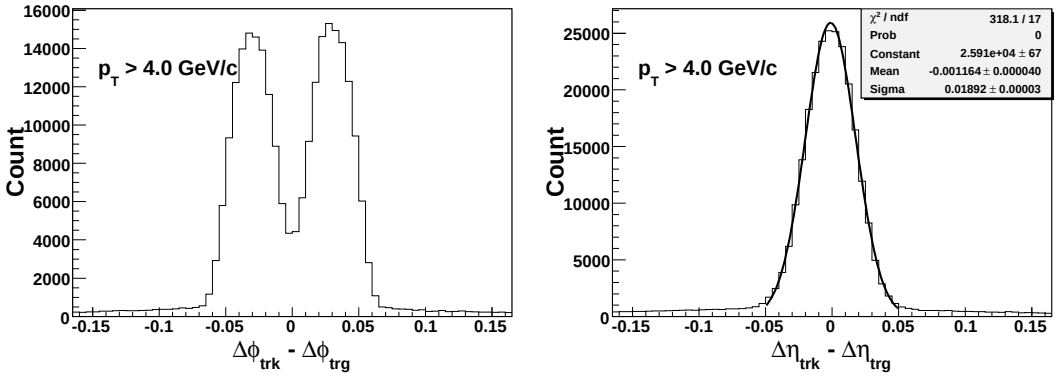

Figure 5.2: ϕ and η differences between projected position and center of triggered tower are shown on the left and right panel respectively.

the BEMC towers. The deposited energies for these MIP are approximately constant, and independent of momentum and particle species. This property provide a convenient calibration reference [CPR02]. To reject these MIP, additional cuts for energy deposited in the BEMC tower are required larger than 2 GeV and less than 2×p (momentum) to reject some tracks which indeed hit the triggered tower, but don't trigger the tower. These two cuts are marked as two lines in Fig. 5.3. In addition, p_T of triggered track is required larger than 3 GeV/c to ensure selected particle with energy larger than the threshold.

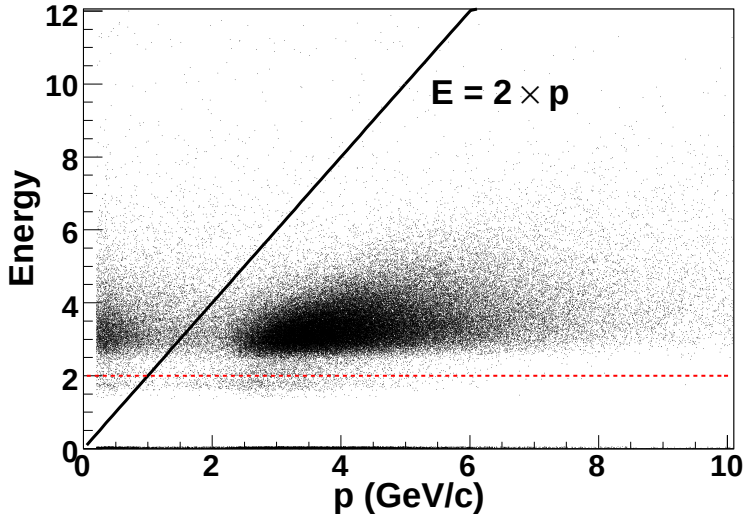

Figure 5.3: Energy versus momentum distribution to reject MIP band and tracks mismatched energy.

Table 5.1: Kinetic cuts for K^0_S reconstruction.

Variable	Cuts	comments
$\Delta\phi$	0.075 rad	Azimuthal angle between center of the BEMC tower and projected track on the BEMC face to select tracks projected in the triggered tower.
$\Delta\eta$	0.075	Psudo-rapidity between trigger center and projected track on the BEMC face.
Energy	2< E <2×p	Ratio of deposited energy in the BEMC and track momentum to remove MIP and false trigger tracks.
Trged p_T	> 3 GeV/c	The p_T of triggered track.
nHitFits	≤ 15	-
ndedxpts	≥ 15	-
η	< 0.5	-
p_T	> 0.2 GeV/c	-
$\lvert n\sigma_\pi \rvert$	< 2	-

Table 5.2: Topological cuts for K^0_S.

dcaV02pV	> 0.6 cm	DCA of V0 to primary vertex
dca in daughters	< 0.9 cm	DCA between daughters
decayLength	> 2.0 cm	Λ Decay Length
dcaPos(neg)2Vtx	> 0.8 cm	DCA of positive (negative) daughter to primary vertex

5.2.3 Topological cuts for K^0_S

According to the long lifetime of K^0_S decay, $c_\tau \sim 2.6\ cm$, and good resolution for vertex reconstruction in mm level, second vertex can be reconstructed and distinguish from the primary vertex. Therefore, the topological cuts can be applied in K^0_S reconstruction to reduce the combinational background. Fig .5.4 shows the topological picture of K^0_S decay to two pions. The topological cuts were studied in [Hei] and implied directly in our analysis, and shown on following Tab. 5.2.

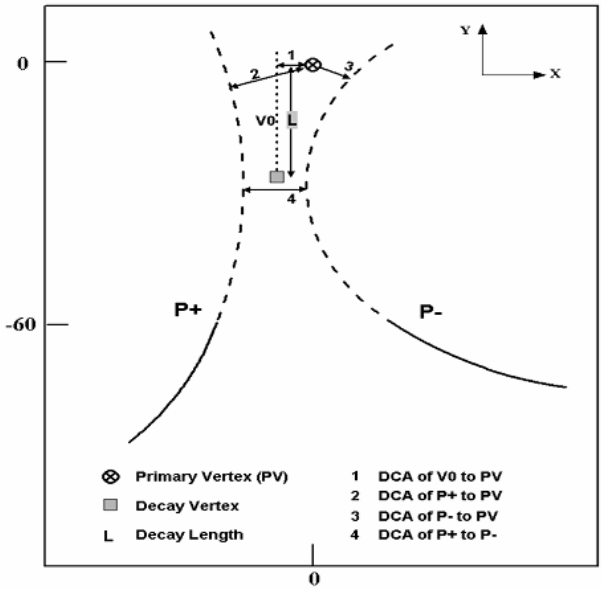

Figure 5.4: Topology for V0 decay.

5.3 K^0_S reconstruction and raw yield extraction

With the "*TPC + BEMC*", K^0_S candidates are reconstructed by one pion from the TPC and the other one from the BEMC in p_T range from 3 GeV/c to 12 GeV/c. Rotation method [Adl02b, Ada05b] and mis-identification method have been studied to reduce the combinational background and residual background, but they do not affect our K^0_S mass distribution. Fig. 5.5 and Fig. 5.6 show the invariant mass distribution in different p_T range from HT1 and HT2 triggered events, respectively.

To extract the raw yields of K^0_S, we need remove the background in the K^0_S invariant mass range. Two methods were tested to get the number of backgrounds in previous study: One is fitting the background with polynomial function; The other one is counting the candidates within two mass windows on both sides of the K^0_S signal (side-band method). The former one is proved to be better than the later one at high p_T range in [Hei]. In our case, a linear function plus a Gaussian function is used to fit the background and signal in this dissertation. Number of K^0_S and its statistical uncertainty can be directly obtained from the fit. In addition, a second polynomial function plus a Gaussian function is used to fit the invariant mass distribution for systematic uncertainties study. Fig. 5.7 shows

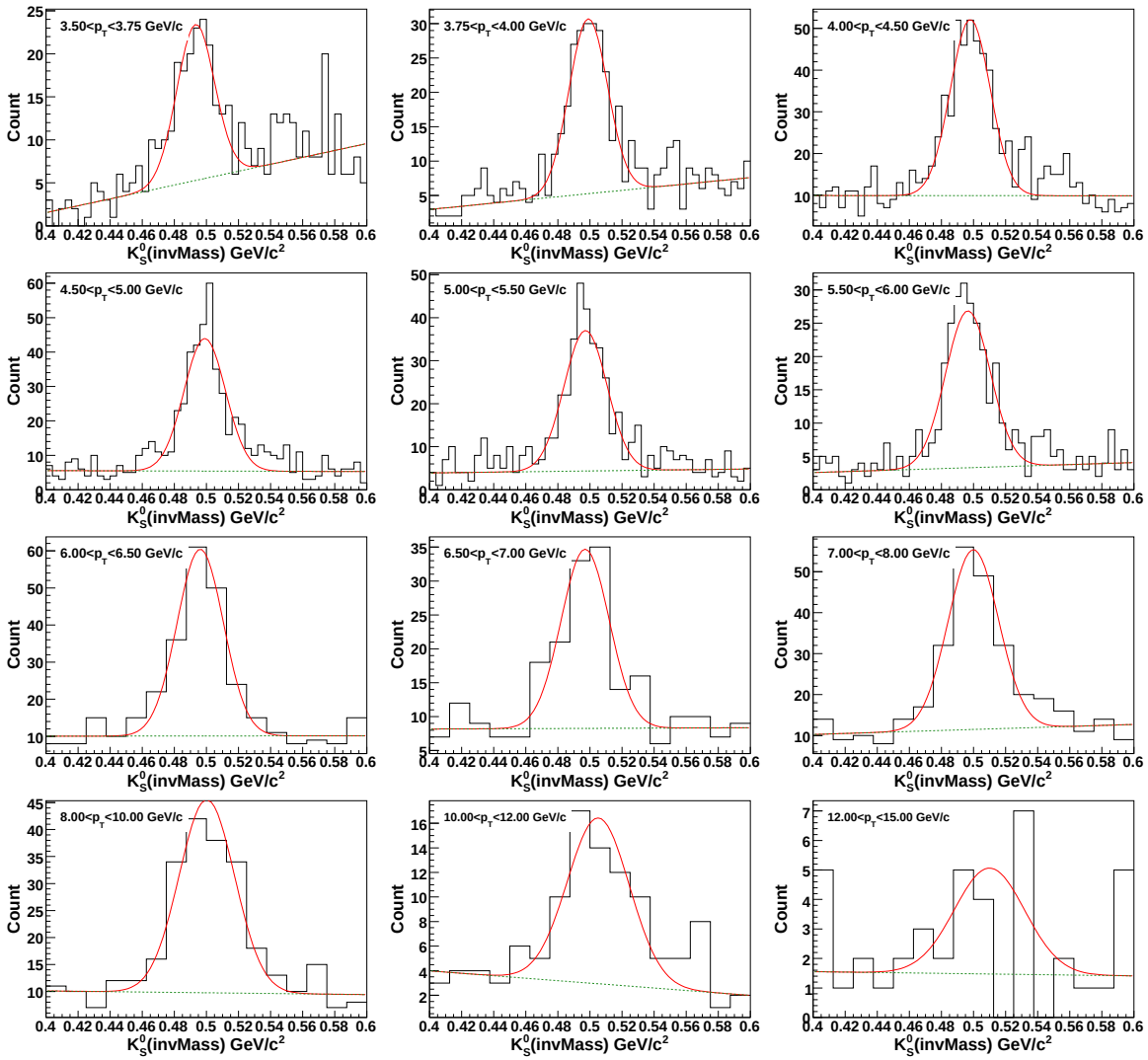

Figure 5.5: Invariant mass from 3.5 GeV/c up to 15 GeV/c in HT1 triggered events.

the obtained K^0_S width and mass. Another way to double-check the raw yields of K^0_S is removing the fitting backgrounds from total counts in K^0_S mass range. This method is independent of the fit quality for K^0_S signal.

With K^0_S raw yields in different p_T slice, p_T spectra for K^0_S in both HT1 and HT2 are shown shown in Fig. 5.8, which also shows published K^0_S spectra in run 3 minimum bias events for comparison.

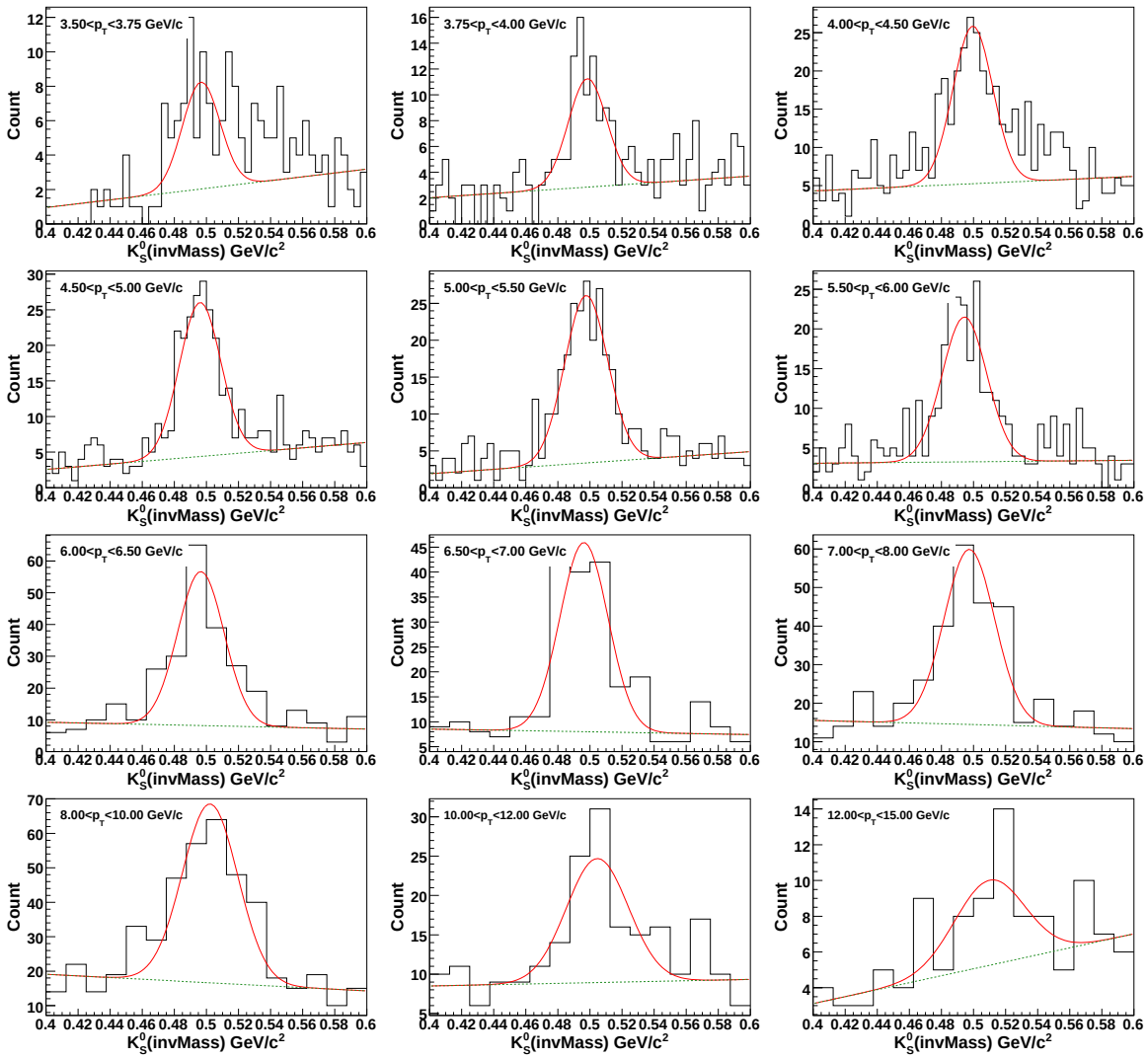

Figure 5.6: Invariant mass from 3.5 GeV/c up to 15 GeV/c in HT2 triggered events.

5.4 Corrections for K^0_S spectra

The raw yields of K^0_S should be corrected for the detector acceptance, detector response efficiency (TPC tracking efficiency and BEMC trigger efficiency) and selection efficiency in reconstruction. Since two daughters from K^0_S decay are identified by the TPC only ("TPC only"), and the BEMC and the TPC ("EMC+TPC") respectively. We get their efficiency separately and then convolute them to get K^0_S reconstruction efficiency according its decay kinematics.

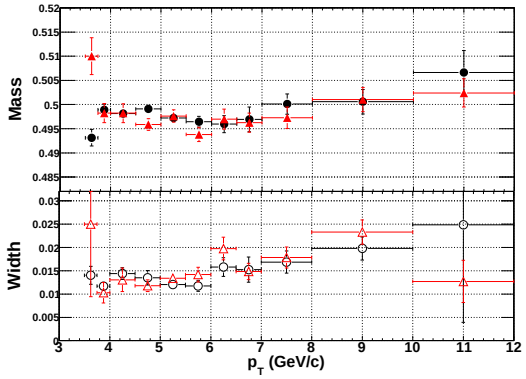

Figure 5.7: Mass and width distribution for K^0_S are shown on the upper panel and the lower panel respectively, circles for HT1 triggered events and triangles for HT2 triggered events.

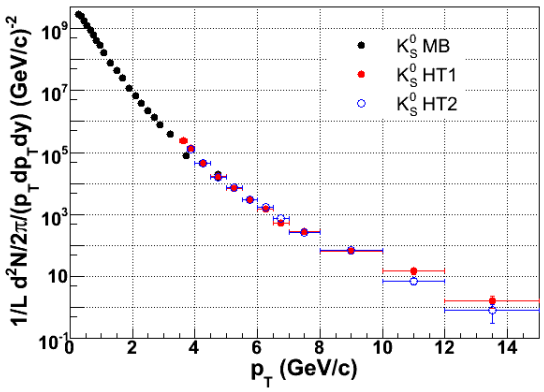

Figure 5.8: Preliminary K^0_S spectra in HT1 and HT2 triggered events and published K^0_S spectra in minibias events shown as black circles.

5.4.1 "TPC only" pion detection efficiency

Due to the TPC acceptance and response, tracking efficiencies of the pion from TPC only were studied and shown in Fig. 3.18. To apply the efficiency at given p_T value in later analysis conveniently, we parameterize the efficiency as function of p_T using Eq. 5.1 for $p_T < 1$ GeV/c,

$$[0] \times exp(-pow([1]/x, [2])) + [3] \times x + [4] \times x \times x, \tag{5.1}$$

and Eq. 5.2 for $p_T > 1$ GeV/c,

$$[0] - exp([1] + [2] \times x) \tag{5.2}$$

Fig. 3.15 has shown Eq. 5.2 for charged pion efficiency at high p_T. Now, we show the fitting results with Eq. 5.1 for low p_T in Fig. 5.9. By combining these two function with their parameters, we can obtain pion tracking efficiency values at given p_T value.

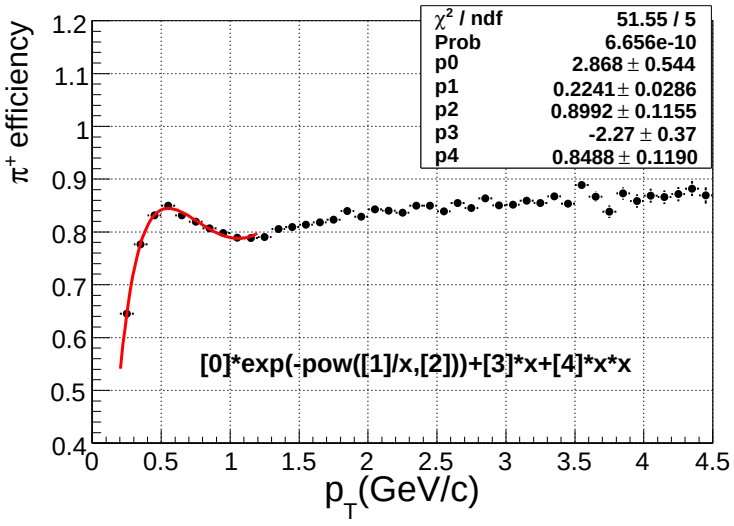

Figure 5.9: pion efficiency at parton $p_T$interval (9,11 GeV/c), and the red curve shows fit at p_T< 1 GeV/c with Function5.1

5.4.2 "EMC+TPC" pion detection efficiency

The "EMC+TPC" pion detection efficiency includes the BEMC trigger efficiency, the TPC tracking efficiency and acceptance etc. Its total efficiency can be derived by comparing the triggered pion raw yields to previous efficiency corrected inclusive pion yields [Ada06b, Xu08]. The raw yields of triggered pion can be obtained by fitting the $n\sigma_\pi$ distributions by multi-Gaussian function as we did in Chapter. 5.

Fig. 5.10 shows charged pion yields in HT1 (shown as circles) and HT2 (shown as stars) triggered events. The published pion yields in minimum bias events and the trigger-bias corrected high-p_T pion spectra from JP2 triggered events obtained before are also shown in the Fig. 5.10 for comparison. The detection efficiencies of triggered pion in HT1 and

HT2 can be obtained by dividing circles (HT1) and stars (HT2) by squares (minibias), respectively. They are shown on Fig. 5.11 as circles and triangles and fitted by following functions:

$$f(p_T) = [0] + [1] \times Erf([2] \times (p_T - [3])) + [4] \times p_T + [5] \times p_T^2 + [6] \times p_T^3, \tag{5.3}$$

and

$$f(p_T) = [0] + [1] \times Erf([2] \times (p_T - [3])) + [4] \times p_T, \tag{5.4}$$

Where

$$Erf(x) = \frac{2}{\sqrt{\pi}} \int_x^\infty e^{-t^2} dt \tag{5.5}$$

The efficiencies of averaged π^+ and π^- both in HT1 and HT2 triggered events are shown on Fig. 5.11 as black circles and trigangles, and fitted by Eq. 5.3 and Eq. 5.4, respectively. The two parameterized curves shown on the Fig. 5.11 will be used in our simulation to obtain the reconstruction efficiency of K^0_S later.

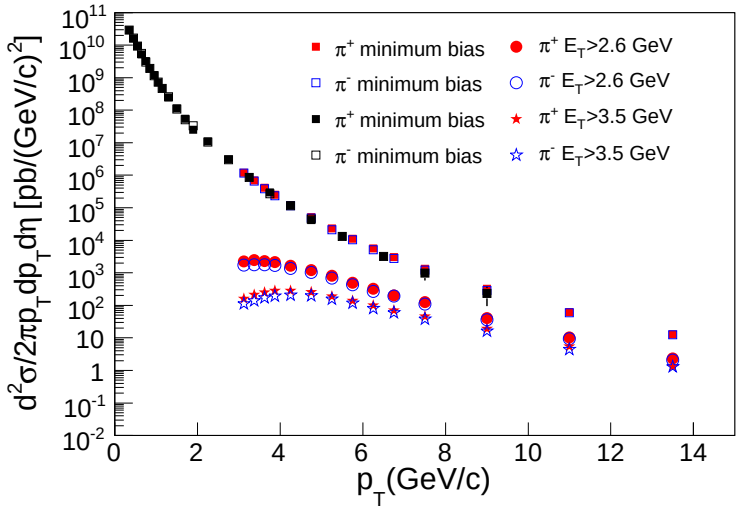

Figure 5.10: Comparison of pion spectra between minbias and HT triggered events.

The trigger efficiency is ∼3% at p_T = 5 GeV/c from Fig. 5.11. According to this value, let's calculate how many equivalent minimum bias events are needed to get the

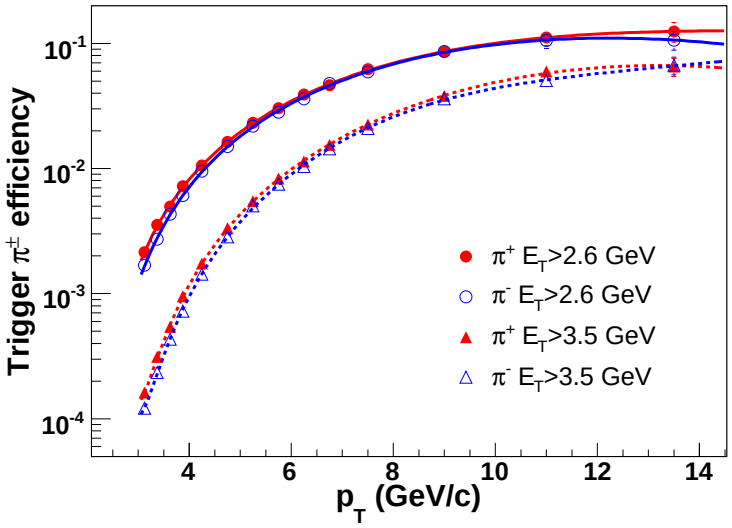

Figure 5.11: Trigger efficiency for charged pion in HT1 and HT2 triggered events (This figure is now updated with final version [Aga11] from thesis-2009 version. The details of the technical part is now summarized in the NIMA eprint and submitted to Nuclear Instrument Method A for publication.)

same number of K^0_S?

$$N = L(0.64pb^{-1}) \times \sigma(30mb) \times \epsilon_{trg}(\sim 3\%)/\epsilon_{trk}(\sim 90\%) \sim 0.6Billion, \qquad (5.6)$$

where N is the number of minimum bias events, L is the luminosity of HT1 triggered events, σ is the non-single diffractive cross section in p+p collisions at STAR, ϵ_{trg} is the trigger efficiency and ϵ_{trk} is the tracking efficiency. This indicates that much more statistics for K^0_S on high p_T are obtained using ∼3 million EMC triggered events, while can not be obtained in minimum bias events so far.

5.4.3 K^0_S trigger efficiency

With the detection efficiencies of the decayed pions (one is identified by "TPC only", and the other is by "BEMC+TPC") the K^0_S detection efficiency is then determined by folding them using the K^0_S decay kinematic. We generate K^0_S sample with flat p_T distribution and flat y distribution from -0.5 to 0.5. The PYTHIA framework software package is used to simulate K^0_S decay to two charged pions. The daughter pion with higher p_T is re-

quired larger than 3.0 GeV/c, treated as triggered pion. We applied the "BEMC+TPC" pion efficiency at the corresponding p_T to it (the efficiency at p_T < 3 GeV/c is set to be 0.). The other pion with lower p_T is associated daughter, and applied the "TPC only" efficiency due to the acceptance, tracking efficiency and dE/dx efficiency. Then, the efficiency of K^0_S in a given p_T bin can obtained by convolution of the decayed pions which are weighted with corresponding trigger efficiency and tracking efficiency at each p_T evaluated from trigger and tracking functions. Finally, the reconstructed K^0_S are filled in one histogram, we call "Histogram(Reconstructed K^0_S)", while the initially generated K^0_S spectra is called "Histogram(Origin K^0_S)". The detection efficiencies of K^0_S due to trigger and tracking are calculated by dividing reconstructed K^0_S by initial K^0_S distribution,

$$\epsilon(Kinetic) = \frac{Histogram(ReconstructedK^0_S)}{Histogram(OriginK^0_S)}, \tag{5.7}$$

The detection efficiencies of K^0_S are shown on the left panel of Fig. 5.12.

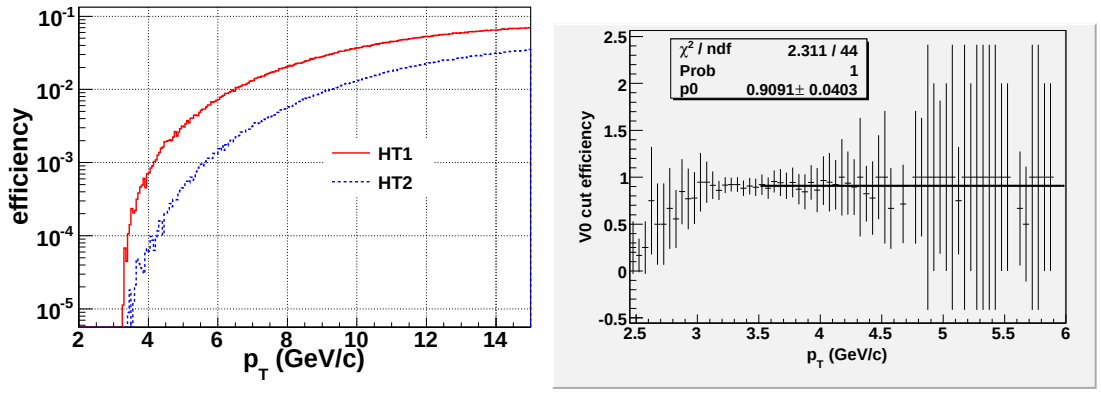

Figure 5.12: Left plot: Combination of K^0_S trigger efficiency and tracking efficiency; Right plot:K^0_S efficiency due to its topological cuts. (This figure is now updated with final version [Aga11] from thesis-2009 version. The details of the technical part is now summarized in the NIMA eprint and submitted to Nuclear Instrument Method A for publication.)

5.4.4 V0 cuts efficiency correction

Due to V0 cuts for good signal to background ratio of K^0_S, many real K^0_S are lost in the finding K^0_S process. This part is not taken into account in our previous simulation, thus is needed to be obtained separately. To do this study, the embedded data generated at run 5 [Abe07c] are used to get the efficiency by dividing K^0_S p_T spectra after V0 cuts mentioned in Tab. 5.2 to the K^0_S spectra before V0 cuts.

$$\epsilon(V0) = \frac{Histogram(V0cut)}{Histogram(input)}, \tag{5.8}$$

The ϵ(V0) as function of p_T can be found on right panel of Fig. 5.12.

Finally, total efficiency for K^0_S for trigger, tracking and topological cuts are combined by these two:

$$\epsilon(K^0_S) = \epsilon(Kinetic) \times \epsilon(V0) \tag{5.9}$$

.

5.5 Systematic uncertainties

We have studied the systematic uncertainties contribute to the final cross section of K^0_S. Following main sources of systematic uncertainties are considered in this analysis:

1. *Different background subtraction for K^0_S.*

   As mentioned before, we use two polynomial functions to describe the background of K^0_S invariant mass distribution in Fig. 5.5 and Fig. 5.6. This results in different yields of signal after subtraction different backgrounds, which contribute about 1.4% uncertainties to K^0_S cross section.

2. *V0 cuts for K^0_S reconstruction.*

   The contribution from V0 cuts has been studied in [Hei], and it results in $\sim$ 5.4% systematic uncertainty in our analysis.

3. *Trigger bias in different trigger.*

   To study the contributions from trigger bias, we compare the K^0_S yields after trigger efficiency correction between two triggered data-sets. 9.7% difference between two yields is taken as trigger bias contribution to the total cross section.

4. *Efficiency determination.*

   On the efficiency determination, 5% systematic uncertainties are included due to the uncertainty on the materials in the STAR simulation software package.

5. *Momentum resolution.*

   To obtain the momentum resolution of K^0_S, we need to know the momentum resolution of daughter pions first. Fig. 5.13 shows the distribution of $\frac{1/p_T(Real)-1/p_T(MC)}{1/p_T(MC)} = \frac{p_T(MC)}{p_T(Real)}$-1 for primary pion at different p_T bin. They are described by the Gaussian function very well. The mean values of Gaussian distribution are almost centered at zero, while the resolutions are linearly depend on the momentum as shown in Fig. 5.14. This indicates that the momentum resolution related to detector resolution becomes worse with increasing p_T. Since the momentum resolutions for primary track in p+p collisions are similar to that in Run 2 Au+Au collisions shown on the left panel in the Fig. 5.15, we use the momentum resolutions of global tracks in Run 2 Au+Au collisions shown on the right panel in Fig. 5.15 to represent hat in our data-set p+p collisions.

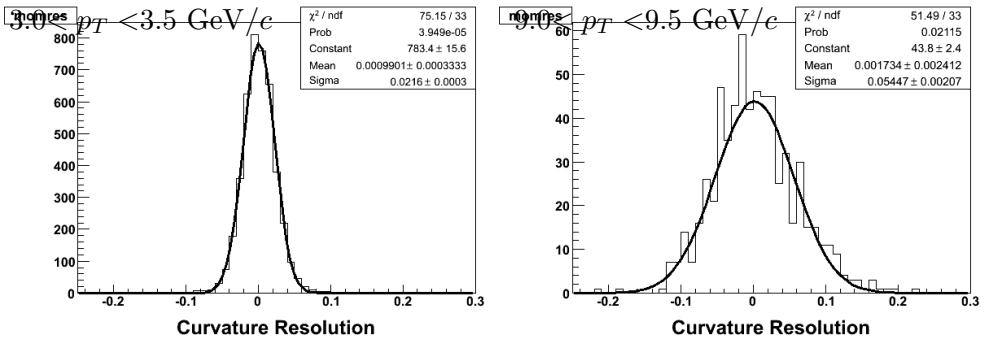

Figure 5.13: The distributions of $\frac{p_T(MC)}{p_T(Real)}$ - 1 for primary pion at $3.0 < p_T < 3.5$ GeV/c (left) and $9.0 < p_T < 9.5$ GeV/c(right), and fitted by Gaussian function.

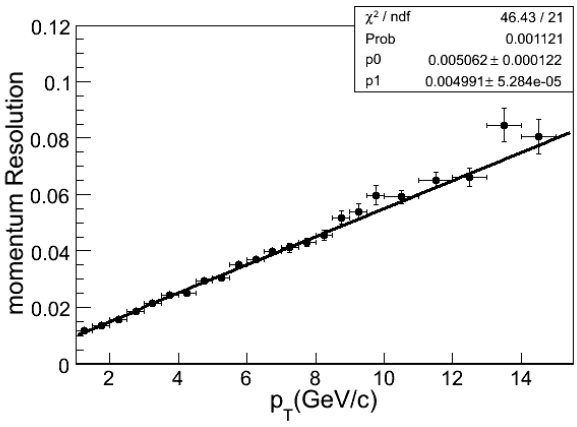

Figure 5.14: Momentum resolution for primary tracks versus p_T in p+p collisions.

To obtain the K^0_S momentum resolution, we simulate the process of K^0_S kinetic decay to two pions, and convolute the daughters' momentum resolution to K^0_S momentum step by step. Firstly, K^0_S distribution as function of p_T are generated for input in the decay process. K^0_S p_T spectra in minimum bias events (published) and high tower triggered events are combined and fitted with Levy function:

$$\frac{1}{2\pi p_T}\frac{d^2N}{dydp_T} = \frac{dN}{dy} \times \frac{(n-1)\times(n-2)}{2\pi nT(nT+m_0(n-2))} \times (1+\frac{\sqrt{p_T^2+m_0^2}-m_0}{nT})^{-n}, \qquad (5.10)$$

where m_0 is the K^0_S mass. This fit function is taken as input of K^0_S distribution in simulation, and is shown in Fig. 5.16.

Secondly, given one decayed pion, its momentum can be smeared according the Gaussian distribution shown in the right panel of Fig. 5.15. Then, K^0_S can be reconstructed by the decayed two pions in simulation. The momentum of reconstructed K^0_S may be shifted due to pions momentum resolution, which is so-called K^0_S momentum resolution. This may change the shape of K^0_S pt distribution. Left panel in Fig. 5.17 shows K^0_S p_T resolution in HT1, HT2 and minimum bias events in simulation. The momentum resolution results in the difference of K^0_S yields between reconstructed and input K^0_S p_T spectra, which is shown in the right panel in Fig. 5.17. This differences are treated as systematic uncertainties in our analysis later.

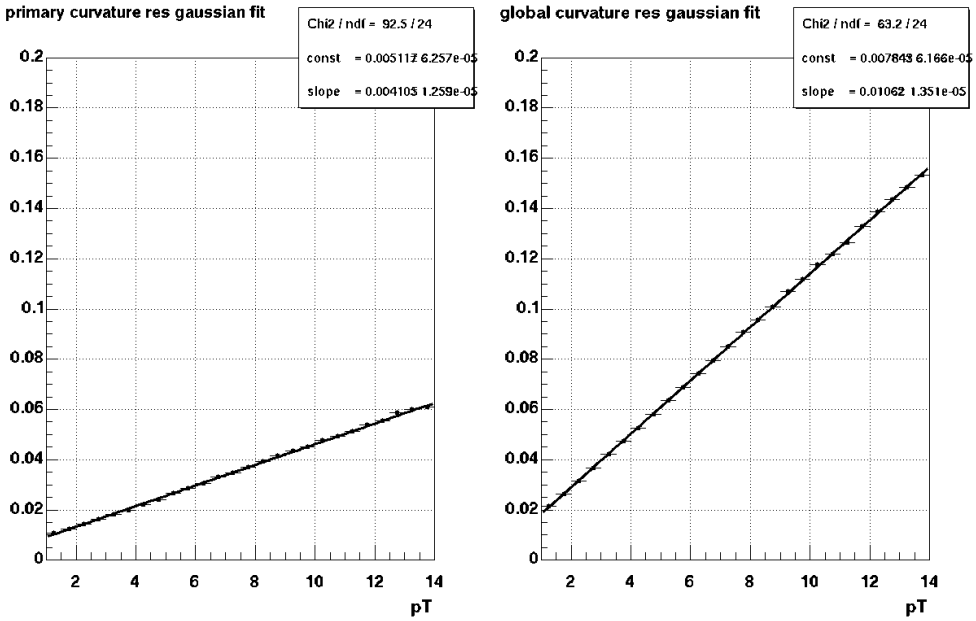

Figure 5.15: Left: Momentum resolution for primary tracks in Au+Au collisions; Right: Momentum resolution for global tracks in Au+Au collisions.

Table 5.3: Sources and countributions of uncertainties.

Background subtraction	1.4%
V0 cuts	5.4%
Trigger bias	9.7%
Efficiency determination	5%
Momentum resolution	-0.0064 + 0.0015×p_T+0.0010×p_T^2

In summary, Tab. 5.3 shows the each source contributions to K^0_S cross-section: background subtraction, V0 cuts, trigger bias, efficiency determination and momentum resolution.

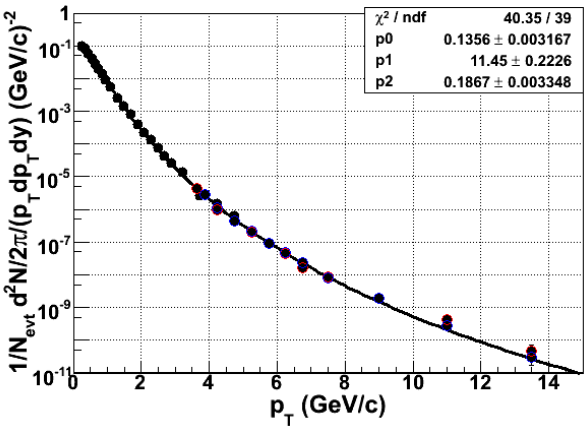

Figure 5.16: pion momentum resolution in p+p collisions.

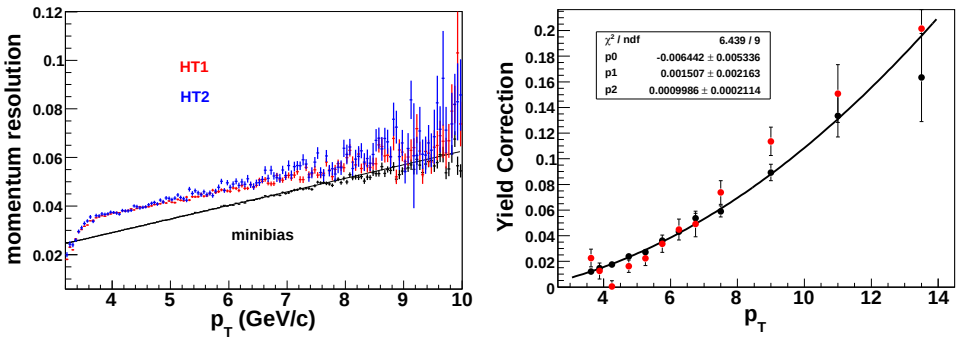

Figure 5.17: Left: K^0_S resolution versus p_T distribution in p+p collisions; Right: K^0_S yield correction versus p_T distribution in p+p collisions.

CHAPTER 6

Results and Discussion

In this chapter, measurements on charged hadrons ($\pi^{\pm}$, $K^{\pm}$, p and $\overline{p}$) and neutral kaon are shown both in p+p and Au+Au collisions. Comparisons of results between p+p and Au+Au systems are discussed through ratios and nuclear modification factors.

6.1 dE/dx Re-calibration method

With enhanced electron identification by the BEMC, pure pions decayed from K^0_S and protons decayed from Λ, dE/dx positions and widths of different charged particles are determined precisely. Their deviations relative to theoretical values versus $\beta\gamma$ and $p_T$mass are well described by the function

$$f(x) = A + \frac{B}{C + x^2}. \tag{6.1}$$

With this method, dE/dx positions of charged particles are re-calibrated to be better than 0.1 σ. The particle identification of charged hadrons can be improved, and uncertainty can be reduced significantly. In addition, we have developed a method to use the ratio e^-/e^+ to correct for and to assess the systematic momentum shift in the negative and positive charged hadrons affected by space charge distortion in the TPC. These are important steps toward fulfilling the physics goals of the STAR experiment at RHIC in the future, and other frontier experiments.

6.2 Spectra in p+p and Au+Au collisions

The invariant yields is defined by:

$$\frac{1}{N_{evt}}\frac{d^2N}{2\pi p_T dp_T dy}, \tag{6.2}$$

where N_{evt} is the number of events, and N is the raw yields of signal corrected for triggered enhancement factor and acceptance tracking efficiency in TPC.

The invariant yields of charged hadrons ($\pi^{\pm}$, $K^{\pm}$, p and $\overline{p}$) are extended up to 15 GeV/c and neutral kaons are extended up to 12 GeV/c at mid-rapidity ($|\eta|$ <0.5) in $\sqrt{s_{NN}}$ = 200 GeV in p+p collisions using the EMC triggered events. Figure 6.1 shows these particle p_T spectra. On the left panel, we show positive particle spectra and K^0_S and ρ spectra in p+p collisions. Meanwhile, we show the negative particle spectra in p+p collisions, and neutral and charged kaon and rho in Au+Au central collisions on the right panel. To compare with pQCD NLO calculations, AKK and DSS [1] calculations are also plotted on the Figure 6.1.

From this figure, our measured $\pi^{\pm}$, $K^{\pm}$, p and $\overline{p}$ spectra are consistent with the published results in minimum bias triggered events. In addition, consistency of charged and neutral kaons with different methods and in different triggered events proves that our measurements are credible. When we compared our spectra with pQCD NLO calculations, we found the spectra for pions can be described by both AKK 2008 and DSS, which provide a convince for the pQCD again. However, kaon and proton spectra can not be described very well by these pQCD NLO calculations at high p_T, especially anti-proton in AKK 2008, which is under-predicted anti-proton production, and is un-physical at high p_T (p_T > 8GeV/c), because the theorist included BRAMTH $\overline{p}/p$ ratio at low p_T and forward rapidity, so our measurements can provide more constraint to fragmentation function in pQCD calculations.

In Au+Au collisions, pion and proton spectra have been published at [Abe06]. Here,

[1] Models of NLO pQCD can be found in Appendix.

we use the re-calibration way to identify pion and proton again for cross-checking previous published results and reducing systematic uncertainties due to dE/dx uncertainties. When we compare our measured pions with published pions, less than 5% difference between them can be found in Figure 6.2. However, it's more difficult to identify kaons, protons and anti-protons in Au+Au collisions than in p+p collisions, because the width for each particle is $\sim 1.06\ \sigma$ in Au+Au collisions, while in p+p collisions, it is about 0.87. This results in more dE/dx uncertainties in Au+Au collisions relative to p+p. We just present p_T spectra for charged kaon at $p_T > 6$ GeV/c in Figure 6.1, because they are separated clearly at this p_T range.

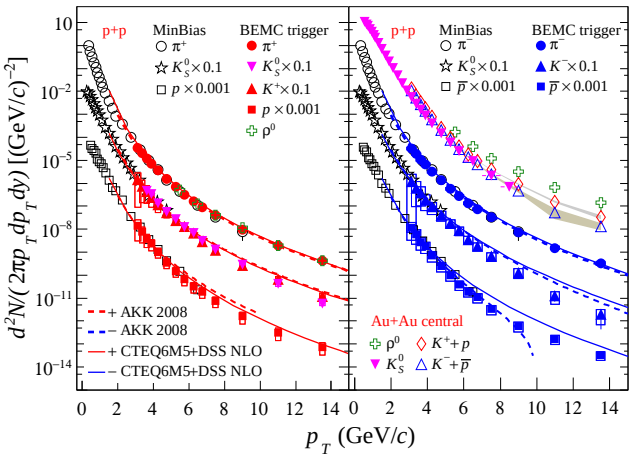

Figure 6.1: On the left panel, the invariant yields $d^2N/(2\pi p_T dp_T dy)$ of positive particle, π^+, K^+, p, and neutral particles, K^0_S and ρ^0 from p+p collisions. On the right panel, the invariant yields of negative particles, π^-, K^-, $\overline{p}$ from p+p collisions and also the spectra of K^0_S, $K^{\pm}$ and ρ^0 in central Au+Au collisions. All the dashed lines on these two panels are from AKK 2008 calculations, and solid lines are calculated from DSS. The bars and boxes represent statistical and systematic uncertainties. **(This figure and related physics discussion are now updated with final version [Aga11] from SQM09 version [Xu10])**

6.3 Ratios in p+p and Au+Au collisions

Particle ratios, π^-/π^+, p/π^+, $\overline{p}/\pi^-$ and $\overline{p}/p$ in mid-rapidity at $\sqrt{s_{NN}} = 200$ GeV in p+p collisions are obtained from the spectra and presented in Figure 6.3, which shows π^-/π^+ on panel (a), $\overline{p}/p$ on panel (b), p/π^+ on (c), and $\overline{p}/\pi^-$ on (d); Our measured ratios

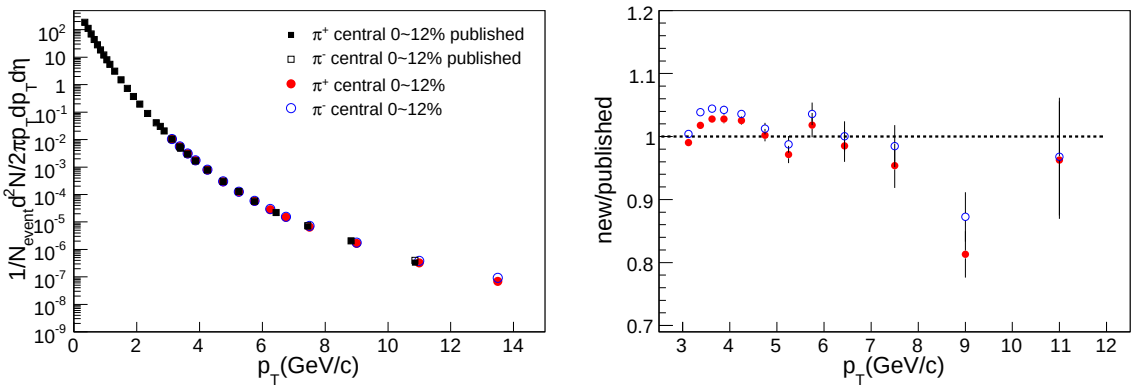

Figure 6.2: On the left panel, pion spectra from published results are shown as black squares and our data points are presented by color circles. On the right panel, the ratios of π^+ and π^- in the new to the old are presented as solid and open circles, respectively.

shown as red stars, while previous results shown as black squares are on the same figure for comparison. In addition, DSS calculation and PYTHIA simulation are plotted as dashed lines and green solid lines, respectively, and the shaded bands and lines represent systematic and statistic uncertainties respectively.

As mentioned before, the statistic uncertainties are reduced at high p_T with the EMC triggered events compared to the previous results using minimum bias events and the systematic errors are also reduced using this re-calibration method. When we compare our measurements to the published results [Ada06b], the consistence between them in the overlapping range provides a good evidence to our new measurements in the BEMC triggered events using the new re-calibration method. The extension of p_T range (up to 15 GeV/c) provides good experimental data to model fit for comparison. With good precision, it shows for the first time at RHIC energy, that π^-/π^+ and $\overline{p}/p$ decrease with increasing p_T in p+p collisions at mid-rapidity. This indicates a significant valence quark contribution to pions and protons production. p/π^+ and $\overline{p}/\pi^-$ reach highest values at $p_T \sim 2$ GeV/c, decrease at intermediate p_T range and approach almost constant values of 0.2 and 0.1 at high $p_T > 6$ GeV/c, respectively. Interestingly, leading order pQCD calculation PYTHIA (version 6.01) can generally reproduce particle ratios, but show significant deviation from spectra with an overall normalization. The NLO pQCD [FSS07] calculations lead to better agreement with measured spectra, but over-predict anti-proton

productions and deviate from ratios of $\overline{p}/p$ and $\overline{p}/\pi^-$. This indicates that light flavor separated and gluon *Fragmentation Functions* used in NLO pQCD calculations, need improvement. This is one of our goals.

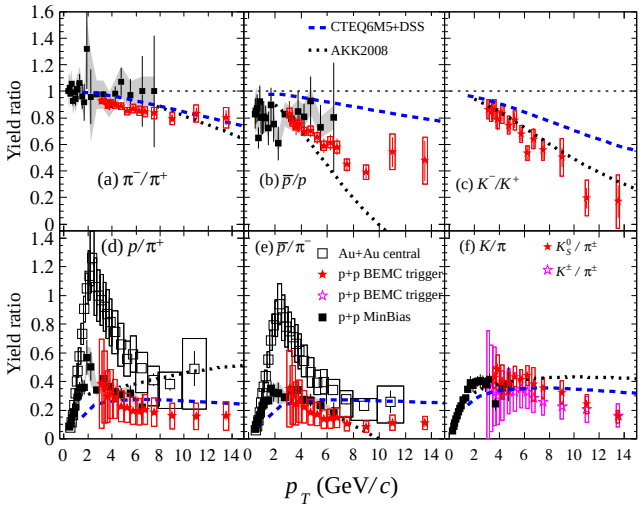

Figure 6.3: Ratios of π^-/π^+ (a), $\overline{p}/p$ (b), p/π^+ (c) and $\overline{p}/p$ (d) as a function of p_T in p+p collisions. The red stars are our new results, and the black squares represent published results from minimum bias events. DSS NLO calculations and PYTHIA simulations are presented as blue dashed line and green solid line respectively. The bars and boxes represent statistical and systematic uncertainties. **(This figure and related physics discussion are now updated with final version [Aga11] from SQM09 version [Xu10])**

In addition, $K^\pm/\pi^\pm$ (shown as open circles) ratios in JP2 and K^0_S/π ratios (shown as solid circles for published results from minimum bias events and red stars for the new results from BEMC triggered events) in HTs trigger are presented on Fig. 6.3. K/π ratios from AKK and DSS calculations are shown as lines on the same figure. From this figure, consistence between K^0_S/π in High Tower triggered events and $K^\pm/\pi^\pm$ in JP2 triggered events provides the credibility of our measurements. K^0_S/π ratios in minimum bias events and the JP2 trigger events are also consistent. The measured K/π is about half of the pQCD value, but similar to that of PYTHIA simulation. Therefore, our measurements provide better constraint to pQCD calculations in the future. **The discussion shown in the brackets is the thesis version and we refer the final discussion to our publication [Aga11] according to Figure 6.5 [Together with kaon production in Au+Au collisions, K^0_S/π and $K^\pm/\pi^\pm$ ratios at high-p_T in Au+Au collisions**

at 200 GeV are obtained and presented first time on the upper panel of Figure 6.5. By comparing the K/π ratios in p+p collisions, we observe significant enhancements for K/π in Au+Au central collisions. This indicates that suppression for kaon is less than for pion in the Quark-Gluon Plasma, or jet flavor changes assuming fragmentation functions do not change from p+p and central Au+Au collisions. On the other hand, jet chemistry can change due to parton splitting in medium even if the flavor does convert.]

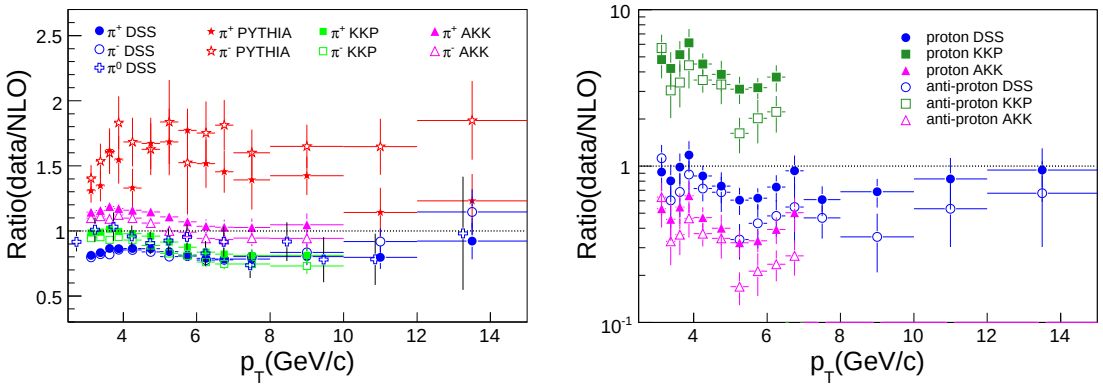

Figure 6.4: The comparisons of data to NLO pQCD calculations and PYTHIA simulations for pion (shown on left plot) and (anti-) proton (shown on the right plot).

6.4 Nuclear modification factors

To further understand Quark Matter Plasma created in Au+Au collisions, as a reference, measurements in p+p collisions are compared with results in Au+Au collisions in this section.

In order to compare particle productions in different system directly, we define a variable, nuclear modification factor (R_{AA}),

$$R_{AA} = \frac{d^2N/(2\pi p_T dp_T dy)}{T_{AA} \times d^2\sigma^{pp}_{inel}/(2\pi p_T dp_T dy)}, \tag{6.3}$$

where $T_{AA} = < N_{bin} > /\sigma^{pp}_{inel}$ describe the nuclear geometry, and $d^2\sigma^{pp}_{inel}/(2\pi p_T dp_T dy)$ is the cross section for p+p collisions and is derived from the measured p+p Non-Single-

Diffractive (NSD) cross section (σ_{NSD}). In STAR, the σ_{NSD}^{pp} is measured as 30 mb, while total cross section (σ_{inel}) is about 42 mb in theory actually, so the R_{AA} in our analysis can be written as:

$$R_{AA} = \frac{42 \times d^2N/(2\pi p_T dp_T dy)_{AuAu}}{30\times < N_{bin} > \times d^2N/(2\pi p_T dp_T dy)_{pp}}, \tag{6.4}$$

The difference between NSD and inelastic differential cross section at mid-rapidity, as estimated from PYTHIA [Rua05], is $\sim 5\%$ at low p_T and negligible at $p_T > 1.0$ GeV/c. **The discussion shown in the brackets is the thesis version and we refer the final discussion to our publication [Aga11] .[Figure 6.5 shows the nuclear modification factor, R_{AA} for $\pi^+ + \pi^-$ (open triangles), $K^+ + K^-$ (blue solid stars), p + $\overline{p}$ (open circles), K_S^0 (red solid stars) and ρ (open triangles) as function of p_T in Au+Au central collisions on the lower panel. On this plot, we can see that R_{AA} for pion, kaon, proton and rho rise at low p_T, and reach the highest at $p_T\sim$ 2 GeV/c, and decrease with increasing p_T at $p_T>$ 2 GeV/c. At high p_T range ($p_T>$ 6 GeV/), where fragmentation processes are dominant, R_{AA} (p + $\overline{p}$) with large errors is larger than R_{AA}($K^+ + K^-$, K_S^0), which is larger than R_{AA}($\pi^+ + \pi^-$). This phenomena are in contradiction to the prediction from flavor-dependent energy loss [Wan98] only. The $R_{AA}(\pi^+ + \pi^-)$ is similar to $R_{AA}(\rho)$, which indicates they have same parton source, and R_{AA} has no relationship with mass of particles. $R_{AA}(K^+ + K^-, K_S^0)$ is consistent with the prediction with jet conversion in the hot medium, as shown by dashed line on Figure 6.5. This indicates possibility of jet conversion contribution to the R_{AA}. The same factor, scaling the lowest-order QCD jet conversion rate, is applied to predict R_{AA} for pion and proton [Xu] in jet conversion scenario, and R_{AA}(p + $\overline{p}$) is similar to R_{AA}($\pi^+ + \pi^-$) in their prediction [LF08b].**

Recently, it was argued that higher twisted effect, enhanced parton splitting alone, can also lead to significant changes in the jet hadron chemical composition [SW08]. In this model, heavier hadrons become more abundant.

For an E_{jet} = 50 GeV jet, the kaon to pion ratio increases by a factor $\sim$ 50% and the proton to pion ratio by a factor $\sim$ 100%. However, the model alone is not consistent with our observations that $R_{AA}(\pi) \simeq R_{AA}(\rho)$. This together with jet conversion mechanism might be able to explain our observations, however requires quantitative modeling and calculations in which 3D-hydro expanding medium, and proper light flavor separated quark and gluon fragmentation functions should be considered.

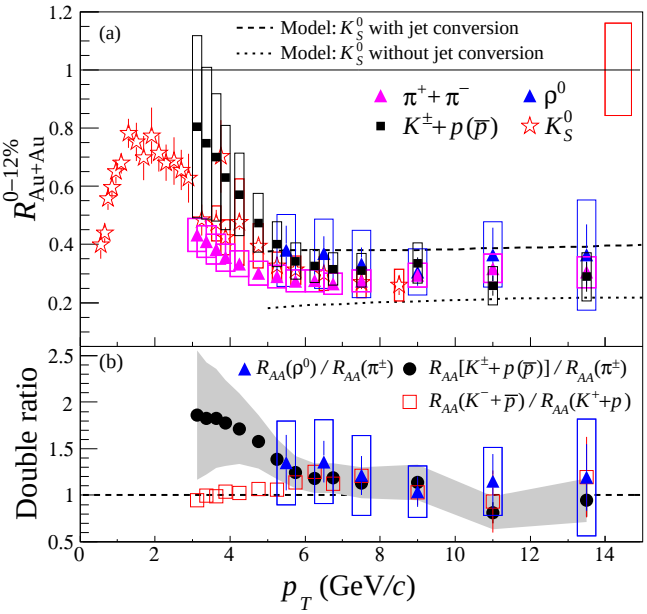

Figure 6.5: On the upper panel, $K^0_S(K^\pm)/\pi$ ratios as function of p_T both in p+p and Au+Au central collisions. One the lower panel, Nuclear modification factors of pion, kaon, proton (anti-proton) and ρ^0 in Au+Au collisions and $K^\pm(K^0_S)/\pi^\pm$ ratios as function of p_T. The bars and boxes represent statistical and systematic uncertainties. **(This figure and related physics discussion are now updated with final version [Aga11] from SQM09 version [Xu10])**

In order to understand more about the jet chemistry change in the QGP, we can study the centrality dependence of K^0_S R_{AA}. Due to limit of statistics, we integrate the R_{AA} at $p_T >$ 5.5 GeV/c, where mechanism of particle production may be dominated by hard processes. The integral R_{AA} and their errors for pion and kaon are integral at each centrality for comparison with following

function:

$$R_{AA}(> 5.5GeV/c) = \frac{\sum(R^i_{AA}/(eR^i_{AA})^2)}{\sum(1/(eR^i_{AA})^2)} \tag{6.5}$$

$$eR_{AA}(> 5.5) = \sqrt{\frac{1}{\sum(eR^i_{AA})^2}} \tag{6.6}$$

The Figure 6.6 shows the R_{AA} versus centrality distribution for pion and K^0_S. Both kaon and pion production are suppressed in central collisions, R_{AA} for kaon is about a factor of 2 larger than R_{AA} for pion, even in peripheral collisions. This let people consider: whether parton flavor conversions are prevalent, even in the smaller systems? whether there is some other soft A+A production mechanism contributing in this p_T range for all centralities, besides jet fragmentation?] To address this, more statistics are needed in the future at RHIC.

6.5 Summary

In summary, we report charged hadrons ($\pi^{\pm}$, $K^{\pm}$, $p(\bar{p})$) transverse momentum (p_T) spectra at mid-rapidity ($\mid y \mid < 0.5$) up to 15 GeV/c, and neutral Kaon (K^0_S) p_T spectra up to 12 GeV/c using events triggered by the Barrel Electro-Magnetic Calorimeter from p+p collisions at $\sqrt{s_{NN}}$ = 200 GeV. With central triggered Au+Au collisions, $K^{\pm}$ spectra should be measured up to 15 GeV/c. In p+p collisions, the $\pi^{\pm}$ spectra are in good agreement with the calculations from the next-to-leading order perturbative QCD models, which fail to reproduce the $K^{\pm}$, K^0_S and $p(\bar{p})$ spectra at high p_T. π^-/π^+ and $\bar{p}/p$ decrease with increasing p_T, which indicates an experimental signature of significant valence quark jet contribution to pion and proton production. However, this is also indicative that anti-proton is from gluon jet. p/π^+ and $\bar{p}/\pi^-$ approach 0.2 and 0.1 respectively at $p_T >$ 6 GeV/c. **The discussion shown in the brackets is the thesis version and we**

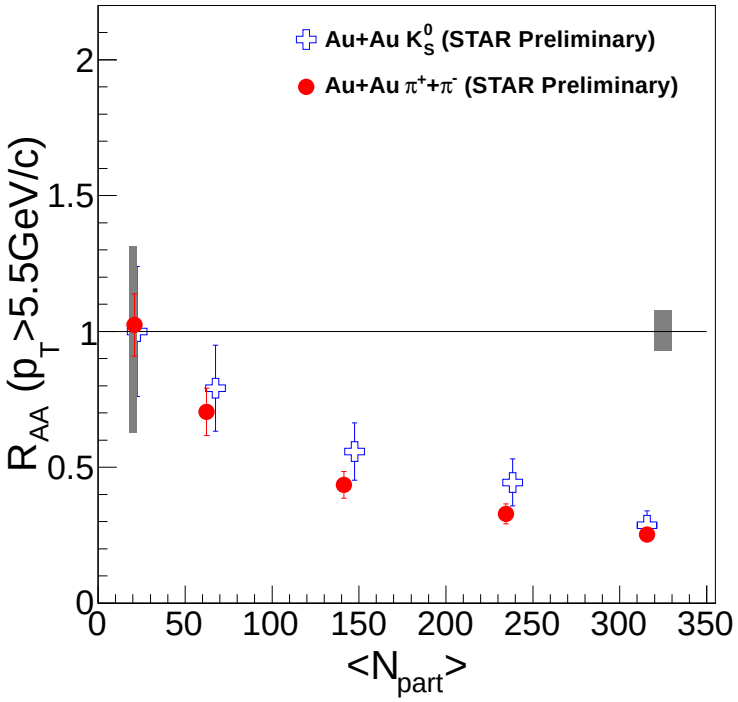

Figure 6.6: Integral R_{AA} at $p_T > 5.5$ GeV/c for pion (red circles) and kaon (blue crosses) versus centrality. The bars represent systematic uncertainties due to centrality. **(This figure and related physics discussion are now updated with final version [Aga11] from SQM09 version [Xu10])**

refer the final discussion to our publication [Aga11]. [At the same p_T range, $R_{AA}(p+\bar{p}) \gtrsim R_{AA}(K^0_S, K^{\pm}) > R_{AA}(\pi^+ + \pi^-)$, and $R_{AA}(\pi^+ + \pi^-)$ is similar to $R_{AA}(\rho^0)$. Our results indicate the change of final jet hadron chemistry from p+p to Au+Au collisions, consistent with jet conversion mechanism and/or modified enhanced parton splitting in the medium.]

CHAPTER 7

Outlook

7.1 dE/dx Re-calibration

The dE/dx re-calibration method has been successfully applied in particle identification in p+p and Au+Au collisions. It can be used to other systems at different energies at STAR, for example, d+Au, Cu+Cu collisions, etc. It also provides a possible tool to identify charged particles at other experiments using the TPC.

The method is also very important to reconstruct resonances at STAR. With the precise dE/dx, residual backgrounds due to mid-identification can be reduced and then the significance of signal can be enhanced. For example, Fig. 7.1 shows the three Gaussian distributions labeled "1", "2" and "3", which have same width (1), and different amplitudes and peak positions. Each one represents one particle distribution, and the amplitude of "1" is a factor 5 higher than "2" and "3". By comparing "2" with "3", 0.5σ difference between them can result in $< 3\%$ contributions from one to another. However, "1" with abundant yields can contribute much more to "2" ($\sim 23\%$) than "3" contributions, although there are 2σ difference between them. Similarly, charged pion can contaminate kaon and proton significantly at STAR. We have found there is 0.4σ deviation of experimental data from theoretical expectation for charged pion. This small deviation can contribute about a factor of two more contaminations to kaons. Therefore, the re-calibration method can reduce mis-identified backgrounds for resonance reconstruction at STAR, such as $K^{\star}$, D^0, ϕ, ρ and so on.

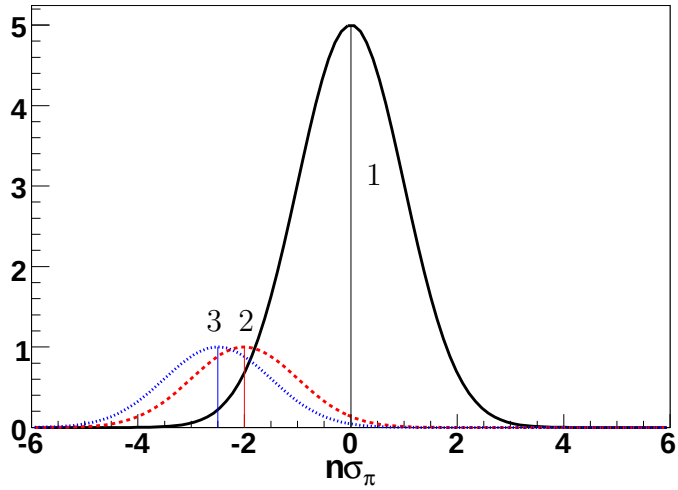

Figure 7.1: Three Gaussian distributions with mean value -2 (blue dot-line), -0.5 (red dash-line), and 0 (black solid-line).

7.2 Other resonances with one triggered daughter

To further study the particle interactions with the medium created in the heavy ion collisions, more kinds of particles are needed to be measured at high p_T. K^0_S has been reconstructed with one daughter triggered by the BEMC and extended up to high p_T 15 GeV/c using the BEMC triggered events, where the BEMC detector is taken as hadronic trigger. The extension measurements in p+p collisions also provide more constraints to NLO pQCD calculations in the future and baseline for heavier ion collisions. The technique can also be applied to reconstruct other particles at high p_T at STAR and other experiments. With the same data sample, we observed clear $\overline{\Lambda}$ signal.

7.2.1 Λ and $\overline{\Lambda}$ reconstruction

Λ and $\overline{\Lambda}$ can be reconstructed through $\Lambda \rightarrow p+\pi^-$ and $\overline{\Lambda} \rightarrow \overline{p}+\pi^+$ channels respectively using the HT1 and HT2 triggered events in p+p collisions collected in year 2005. With the same way for K^0_S reconstruction, one daughter particle triggered by the BEMC can be selected by following cuts of $|\Delta\phi| < 0.075\ rad$, $|\Delta\eta| < 0.075$ and the ratio of energy to momentum ($2.0 < E/p < 1.5 \times p_T$). The V0 cuts for Λ and $\overline{\Lambda}$ are also from previous study using minimum bias p+p events in year 2002 [Abe07c]. The details of cuts for Λ and

Table 7.1: Topological cuts for Λ and $\overline{\Lambda}$.

dcaV02pV	dcaDaughters	decayLength	dcaPos(neg)2Vtx
$< 0.6\ cm$	$< 0.9\ cm$	$> 2.0\ cm$	$> 0.8\ cm$

$\overline{\Lambda}$ are listed in following Tab. 7.1:

The $\overline{\Lambda}$ can be reconstructed with p and π^- passing above cuts and its invariant mass distribution at p_T from 7.0 GeV/c to 8.0 GeV/c is shown in the Fig. 7.2. Indeed, clear $\overline{\Lambda}$ signal has been observed at 10 GeV/c. However, we can not observe Λ signal with this method. This phenomenon is easy to explain. Anti-proton is easier to be triggered by the BEMC with respect to proton, since anti-proton can annihilate with proton in the BEMC and deposit much more energy in the tower (at least 2 GeV). Previous study found that $\sim$40% anti-protons can be triggered, but $< 3\%$ for proton.

Then, raw yields of $\overline{\Lambda}$ can be derived from the (p,π) invariant mass distribution as we did for K^0_S, and corrected by trigger, tracking and V0 cuts efficiency *etc.*.

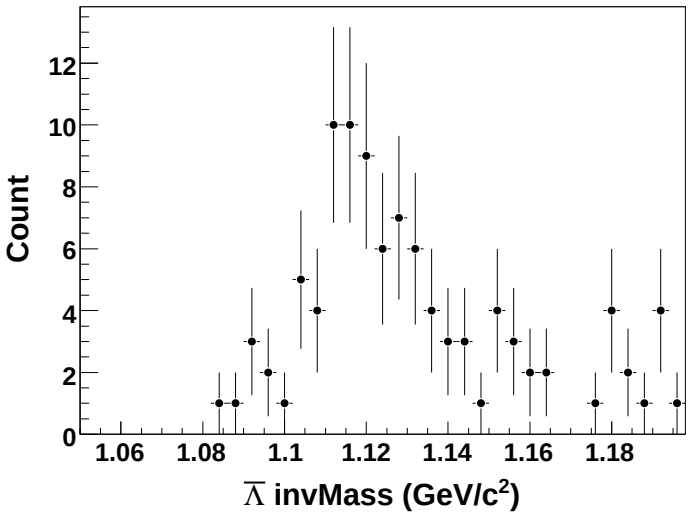

Figure 7.2: Invariant mass of $\overline{\Lambda}$ in $7.0 < p_T < 8.0$ GeV/c. (be changed in each p_T)

7.2.2 ρ reconstruction and other resonances

ρ mesons in p+p collisions are measured up to 11GeV/c using the jet patch triggered events and shown on the Fig. 7.3 [Fac08]. With the one pion triggered by the BEMC tower, ρ mesons can be reconstructed through decay mode $\rho^0 \rightarrow \pi^+ + \pi^-$ using high tower trigger events, which will be compared with previous results for double-checks. Besides, $K^\star$, ϕ, D^0 can be in both p+p collisions and Au+Au collisions.

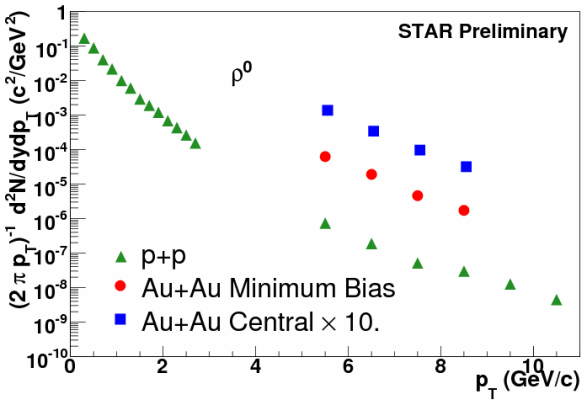

Figure 7.3: ρ meson p_T spectra in p+p minimum bias events, Au+Au minimum bias and Au+Au central collisions.

7.3 Detector Upgrades

More related studies can be developed after some STAR detector upgrades in the future, Data Acquisition (DAQ1000), Time-Of-Flight (TOF), Heavy Flavor Tracker (HFT), etc.

7.3.1 DAQ1000

First of all, DAQ for the TPC has been upgraded this year with rate larger than 100 Hz, which was 100 Hz in the past. As we known, the TPC is the slowest detector in the STAR, and almost all of other detectors in the STAR have DAQ rate $>$ 1000 Hz. This prevent us from taking advantage of the increasing high luminosity of RHIC. With the same luminosity, PHENIX can take about two orders of magnitude events more than

STAR.

With high luminosity, decreased dead time of DAQ1000 enable STAR collect much more events in both p+p and Au+Au collisions. Further more, the DAQ 1000 may also improve the dE/dx resolution, thus help the identified particle spectra measurement at high p_T future.

7.3.2 Time-Of-Flight

The first tray of Time-Of-Flight (TOF) based on Multi-gap Resistive Plate Chamber (MRPC) technology [Rua05], first developed by CERN, was installed at outer of the TPC in year 2003, and covered -1 $< \eta <$ 0 and $\pi/30$ in ϕ. The resolution achieved by that TOF prototype was ∼85 ps with efficiency of more than 95% in Au+Au collisions at 200 GeV. The TOF detector can extend the capability of PID for K/π separation from $\sim$ 0.6 GeV/c up to $\sim$ 1.7 GeV/c, and proton separation from pions and kaons from $\sim$ 1.0 GeV/c up to $\sim$ 3.0 GeV/c approximately. Fig. 7.4 shows the PID in TPC by energy loss (dE/dx) on upper panel and in TOF by the inverse velocity ($1/\beta$) on lower panel.

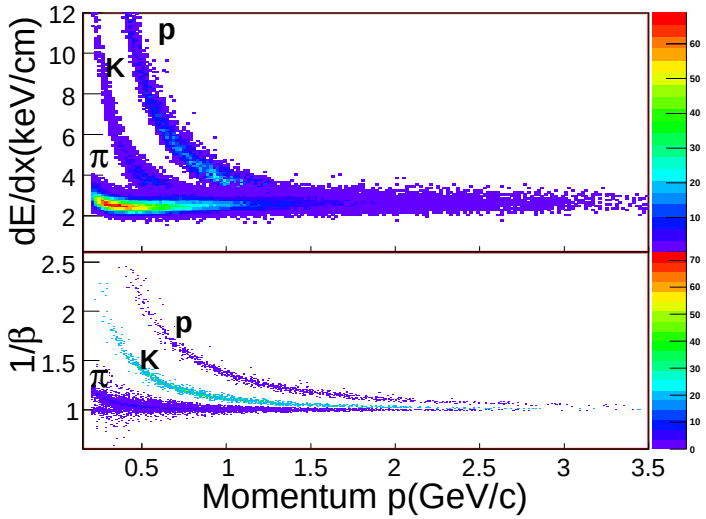

Figure 7.4: Upper panel is the ionization energy loss (dE/dx) in the TPC, while lower panel is the inverse velocity of particles from the TOF.

With the extended PID range, we can reduce the residual background for resonance reconstruction, and extend our measurements to higher p_T. For example, phi and $K^{0\star}$ are re-

constructed through mode: $\phi \rightarrow K^{+}+K^{-}$ and $K^{0\star} \rightarrow K^{\pm}+\pi^{\mp}$. Due to small coverage, it's difficult to reconstruct ϕ and $K^{0\star}$ with their daughters both selected from the TOF. Therefore, with TOF information, ϕ and $K^{0\star}$ are reconstructed by only one daughter track triggered by TOF with the other random track from the TPC, named "TOF+TPC" method, comparing "TPC+TPC" method with two daughter tracks both from TPC. Fig. 7.5 shows ϕ invariant mass distribution with "TOF+TPC" and "TPC+TPC" methods. Clearer signal at ϕ mass position is shown from "TOF+TPC" method than "TPC+TPC".

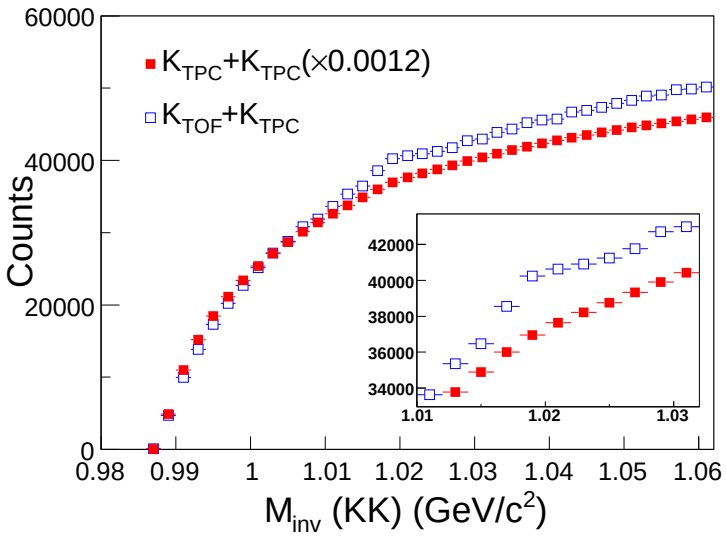

Figure 7.5: Invariant mass distribution for ϕ with two method, "TOF+TPC" and "TPC+TPC". The small panel in the figure is the zoomed distribution.

To further investigate the PID capability of TOF, the signal to background ratios for ϕ-meson and $K^{0\star}$ are taken at low p_T and mid-p_T region, and shown on the Fig. 7.6. Ratios for phi on the left panel show significant enhancement in mid-p_T using "TOF+TPC" method, while $K^{0\star}$ ratios on the right panel show similar enhancement factor in each p_T range.

When we compare enhancement factor for the S/(S+B) ratios in "TOF+TPC" by "TPC+TPC" with that in TOF simulation in proposal at each p_T bin, our measurements are consistent with estimated values from TOF proposal very well. Listed in Tab. 7.2 are from TOF proposal [col], the reduction factors of the integrated luminosity for achieving the same signal quality merit using full TOF simulation, which is equivalent to the

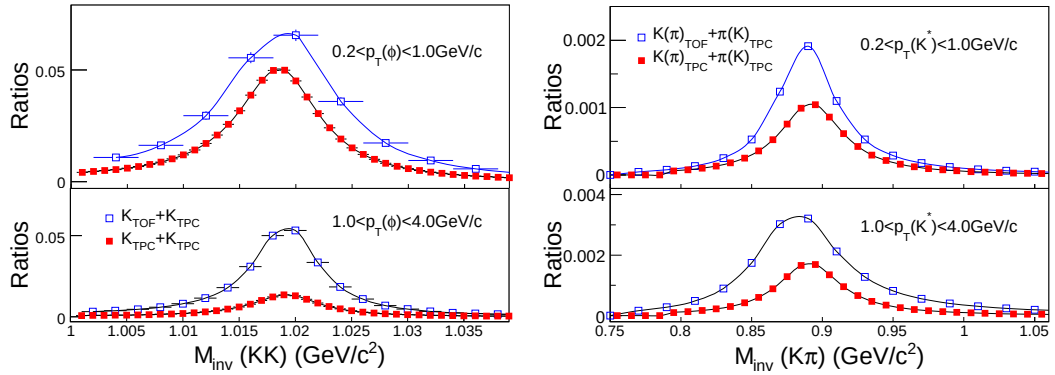

Figure 7.6: The ϕ and $K^{0\star}$ ratio of signal-to-background, S/(S+B), distribution for "TOF+TPC" (open squares) and "TPC+TPC" (solid squares) scenarios in two different p_T ranges.

Table 7.2: Reduction factors of $K^{*0}(\overline{K^{*0}})$ and ϕ mesons of integrated luminosity with both daughters selected by full TOF from TOF proposal [col], which is equivalent to improvement factor $S/\sqrt{(S+B)}$. [al08]

Resonance	Parent p_T(GeV/c)	Reduction factor
K^*	0.0-1.0	2.0
K^*	1.0-2.0	1.85
K^*	3.0-5.0	1.39
ϕ	0.0-2.0	5.0
ϕ	2.0-5.0	3.42

improvement factor of $S/\sqrt{(S+B)}$ as their two decay tracks are identified by TOF. To have a comparison we list in Tab. 7.3 the improvement factors as one charged track is identified by TOF and the other one by TPC from the analysis of experimental data of Au+Au collisions. The results from simulation and data are consistent with each other.

From above studies, we can see how much improvement for reconstructed resonances at intermediate p_T with one track identified by the TOF. The proposed TOF will be upgraded to cover full barrel of TPC in the year 2010, and cover -1 $<\eta<$ 1 and $\sim 2\pi$ in azimuthal angle. With its large acceptance and good PID capability, the full TOF system can help to reduce the combinatorial background greatly by identifying the charged tracks, and suppress the particle misidentification background efficiently. Therefore, the resonance yields can be measured with much higher precision statistics up to the moderately higher

Table 7.3: Enhanced factor of signal-to-background ratio of $K^{*0}(\overline{K^{*0}})$ and ϕ mesons with one daughter identified with TOF.

Resonance	Parent p_T(GeV/c)	Enhanced factor
K^*	0.4-1.5	1.9
K^*	1.5-2.5	2.67
K^*	2.5-5.0	1.40
ϕ	1.0-2.0	4.77
ϕ	2.0-3.0	3.31

$p_T(\sim 4$ GeV/$c)$ region, and more exciting physics are expected after this upgrades.

7.4 R_{AA} discussions

R_{AA} as a probe to measure properties of QGP are discussed above and shown in Fig. 6.5. Our measurements show suppressions of particles in heavy ion collisions, which indicates existence of QGP matter. Then, consistence with jet flavor conversion give us a clue how jet parton interact with the new phase matter.

With the development of experimental results, theorist also make great progress on theory for explaining measurements, such energy loss [Wan98], jet flavor conversion. Uncertainties for STAR results at high p_T will be reduced with more statistics, and more particle species can be reconstructed, then more comparisons of experiments and theory will accelerate revealing the truth in the future.

In addition, another theory, increasing parton splitting is provided to predict the enhancement of K/π and p/π ratios in medium relative to vacuum in LHC energy [SW08]. Therefore, more results from different experiments will provide more evidences of QGP.

APPENDIX A

Models of NLO pQCD

There are popular NLO pQCD calculations by convolution of PDF from CTEQ collaboration [CTE], cross-section and fragmentation functions (FF) with name denoted by authors: Binnewies-Kniehl-Kramer (BKK) [BKK], Kniehl-Kramer-Potter (KKP) [KKP01, KKP], Albino-Kniehl-Kramer (AKK) [AKK05], Kretzer [Kre00] and de Florian-Sassot-Stratmann (DSS) [FSS07].

In general, they all have in common that they have similar PDF and analyze hadron data mostly from e^+e^- in LEP and other experiments, to get the fragmentation functions. The aim of them is that they can describe mechanism of parton fragmentation in an universal rule, and predict other cross sections in the future. The dominant difference is their FFs which are different in form and parameters by fitting different experimental data.

Firstly, BKK, KKP and Kretzer are older models, while AKK and DSS are developed recently. Both Kretzer and KKP generated from BKK used the mostly simple function form as input distribution.

$$D_i^H(z, \mu_0^2) = N_i z^{\alpha_i^h} (1-z)^{\beta_i^h}, \tag{A.1}$$

where

$$z \equiv 2E_h/Q = 2P_h \cdot q/Q^2, \tag{A.2}$$

[Kre00] is the energy of the observed hadron scaled to the beam energy, with the positron/electron beam momentum $P_{e^\pm} = (Q/2, 0, 0, \pm Q/2)$ and $q = P_{e^+} + P_{e^-}$, and i represents g, light quarks (u, d, s) and heavy quarks (b and c) and corresponding

anti-quarks. It fitted e^+e^- data to parameterize the D_i^H at some initial scale μ_0 for the Q^2-evolution. For light partons, the input scale is low $\mu_0^2 = 0.26\ GeV^2$ in the recent NLO revisions [GRV98] of radiative parton model [GRV90, GRV92], while $\mu_0^2 = m_{b,c}^2$ for heavy parton with the partonic threshold $Q^2 > 4m_i^2$. Kretzer considered charge-sign of pions, and gave π^+ and π^- functions separately. KKP didn't separate charges, and only gave the averages over the charges, such as $(\pi^+ + \pi^-)/2$. The other difference between the two was that Kretzer's gluon→pion fragmentation function was quite a bit smaller than KKP's. However, e^+e^- data has rather little sensitivity to the gluon fragmentation function, because in e^+e^- collisions produce primarily quarks and anti-quarks, but not gluons so much.

Then, the AKK came out recently, which adopted KKP set, because it seemed that a larger gluon fragmentation function was important, and the KKP set worked better than the Kretzer, when the RHIC data came. At the beginning, they added some data sets, such as Λ , p, n and so on, but still didn't distinguish between π^+ and π^- for example. Then, $\sim$ 2008, it can describe charged hadron spectra by separating quark flavors and adding data sample from p+p collisions at $\sqrt{s}$ = 200 GeV from the BRAHMS [Ars07], PHENIX [Adl03c] and STAR [Ada06b, Ada06a, Abe07c], such as π^0 and K_S^0 in STAR are required to constrain $\pi^\pm$ both in STAR and BRAHMS and $K^\pm$ in BRAHMS only by following equations:

$$D_i^{\pi^0}(z,\mu^2) = 1/2 D_i^{\pi^\pm}(z,\mu_f^2) \tag{A.3}$$

and

$$D_i^{K_S^0}(z,\mu^2) = 1/2 D_j^{K^\pm}(z,\mu^2) \tag{A.4}$$

where $j = u$, d if $i = d$, u, otherwise $i = j$, which follow from the highly reliable assumptin of SU(2) isospin symmetry between u and d quarks. Also Λ and $\overline{\Lambda}$from STAR are used in AKK 2008, although they are too inaccurate for a reasonable fit of valence quark FFs for $\Lambda/\overline{\Lambda}$ due to the limits of measured p_T range. Besides, $p/\overline{p}$ both in STAR and BRAHMS are added in this global fit. In addition, PDF in AKK 2008 use the updated CTEQ6.5S0 instead of CTEQ5 in previous AKK. However, $\overline{p}$ in this calculation under-predict the

measured production in STAR experiment [Xu], which may be due to the small $\overline{p}/p$ ratios at forward rapidity in BRAHMS.

Finally, DSS determine for the first time individual FFs for quarks and anti-quarks for all flavors as well as gluons from data, and their input distribution is shown below:

$$D_i^H(z,\mu_0) = \frac{N_i z^{\alpha_i}(1-z)^{\beta_i}[1+\gamma_i(1-z)^{\delta_i}]}{B[2+\alpha_i,\beta_i+1]+\gamma_i B[2+\alpha_i,\beta_i+\delta_i+1]}, \tag{A.5}$$

where $B[a,b]$ represents the Euler beta function and N_i is normalized such as to represent the contribution of D_i^H to the sum rule, $\sum \int_0^1 dz z D_i^H(z,Q^2) = 1$. Initial parametrization, $\gamma_i = 0$ would introduce artificial correlations between the behavior of FFs in different regions of z obscuring also the assessment of uncertainties. The extra term $\sim (1-z)_i^\delta$ considerably improves the quality of the global fit, closely related to the fact that the analysis of FFs is restricted to medium-to-large z. The initial scale $\mu_0 = 1$ GeV is taken for the Q^2-evolution in this analysis. Data sample for global fit are from SIA in TPC at $\sqrt{s} = 29$ GeV, SLD, ALEPH, DELPH1 and OPAL at $\sqrt{s} = M_z$, TASSO at $\sqrt{s} = 33$ and 44 GeV. Also data from RHIC experiments, STAR, PHENIX and BRAHMS are included, except the most forward bin, $< \eta > = 4.0$ at the STAR, $\eta = 3.3$ at the BRAHMS, as they have large uncertainties due to the small p_T values probed. In addition, data with $p_T < 1$ GeV/c from the single-inclusive hadron production are excluded from the global fit. Flavor separation make it distinguish between π^+ and π^-, and similar requests for K_S^0 and π^0 are used for parameter constraint in the DSS as well as in AKK described in Eq. A.3 and Eq. A.4. It can describe our charged pions very well, but over-predict measurements of anti-proton and charged kaons from STAR [Xu, Xu09].

References

[Abe06] B. I. Abelev et al. "Identified baryon and meson distributions at large transverse momenta from Au + Au collisions at s(NN)**(1/2) = 200-GeV." *Phys. Rev. Lett.*, **97**:152301, 2006.

[Abe07a] B. I. Abelev et al. "Energy dependence of $\pi^{\pm}$, p and $\bar{p}$ transverse momentum spectrafor Au+Au collisions at $\sqrt{s_{\rm NN}}$ = 62.4 and 200 GeV." *Phys. Lett.*, **B655**:104–113, 2007.

[Abe07b] B. I. Abelev et al. "Partonic flow and Phi-meson production in Au + Au collisions at s(NN)**(1/2) = 200-GeV." *Phys. Rev. Lett.*, **99**:112301, 2007.

[Abe07c] B. I. Abelev et al. "Strange particle production in p + p collisions at s**(1/2) = 200-GeV." *Phys. Rev.*, **C75**:064901, 2007.

[Abe07d] B. I. Abelev et al. "Transverse momentum and centrality dependence of high-pt non-photonic electron suppression in Au+Au collisions at $\sqrt{s_{NN}}$ = 200 GeV." *Phys. Rev. Lett.*, **98**:192301, 2007.

[Abe08] B. I. Abelev et al. "Charmed hadron production at low transverse momentum in Au+Au collisions at RHIC." 2008.

[Abe09] B. I. Abelev et al. "Systematic Measurements of Identified Particle Spectra in pp, d^{+} Au and Au+Au Collisions from STAR." *Phys. Rev.*, **C79**:034909, 2009.

[Abr98] P. Abreu et al. "pi+-, K+-, p and anti-p production in Z0 →q + $\overline{q}$, Z0 → b + $\overline{b}$, Z0 → u + $\overline{u}$, d + $\overline{d}$, s + $\overline{s}$." *Eur. Phys. J.*, **C5**:585–620, 1998.

[Ada03] John Adams et al. "Evidence from d + Au measurements for final-state suppression of high p(T) hadrons in Au + Au collisions at RHIC." *Phys. Rev. Lett.*, **91**:072304, 2003.

[Ada04a] John Adams et al. "Azimuthal anisotropy and correlations at large transverse momenta in p + p and Au + Au collisions at s(NN)**(1/2) = 200-GeV." *Phys. Rev. Lett.*, **93**:252301, 2004.

[Ada04b] John Adams et al. "Particle dependence of azimuthal anisotropy and nuclear modification of particle production at moderate p(T) in Au + Au collisions at s(NN)**(1/2) = 200-GeV." *Phys. Rev. Lett.*, **92**:052302, 2004.

[Ada05a] John Adams et al. "Experimental and theoretical challenges in the search for the quark gluon plasma: The STAR collaboration's critical assessment of the evidence from RHIC collisions." *Nucl. Phys.*, **A757**:102–183, 2005.

[Ada05b] John Adams et al. "K*(892) resonance production in Au + Au and p + p collisions at s(NN)**(1/2) = 200-GeV at STAR." *Phys. Rev.*, **C71**:064902, 2005.

[Ada05c] John Adams et al. "Open charm yields in d + Au collisions at s(NN)**(1/2) = 200-GeV." *Phys. Rev. Lett.*, **94**:062301, 2005.

[Ada05d] John Adams et al. "Phi meson production in Au + Au and p + p collisions at s**(1/2) = 200-GeV." *Phys. Lett.*, **B612**:181–189, 2005.

[Ada05e] John Adams et al. "Pion, kaon, proton and anti-proton transverse momentum distributions from p + p and d + Au collisions at s(NN)**1/2 = 200-GeV." *Phys. Lett.*, **B616**:8–16, 2005.

[Ada06a] John Adams et al. "Forward neutral pion production in p+p and d+Au collisions at s(NN)**(1/2) = 200-GeV." *Phys. Rev. Lett.*, **97**:152302, 2006.

[Ada06b] John Adams et al. "Identified hadron spectra at large transverse momentum in p + p and d + Au collisions at s(NN)**(1/2) = 200-GeV." *Phys. Lett.*, **B637**:161–169, 2006.

[Adl02a] C. Adler et al. "Centrality dependence of high p_T hadron suppression in Au+Au collisions at $\sqrt{s}_{NN}$ = 130-GeV." *Phys. Rev. Lett.*, **89**:202301, 2002.

[Adl02b] C. Adler et al. "K*(892)0 production in relativistic heavy ion collisions at S(NN)**(1/2) = 130-GeV." *Phys. Rev.*, **C66**:061901, 2002.

[Adl03a] Stephen Scott Adler et al. "Absence of suppression in particle production at large transverse momentum in s(NN)**(1/2) = 200-GeV d + Au collisions." *Phys. Rev. Lett.*, **91**:072303, 2003.

[Adl03b] Stephen Scott Adler et al. "Elliptic flow of identified hadrons in Au + Au collisions at s(NN)**(1/2) = 200-GeV." *Phys. Rev. Lett.*, **91**:182301, 2003.

[Adl03c] Stephen Scott Adler et al. "Mid-rapidity neutral pion production in proton proton collisions at $\sqrt{s}$ = 200-GeV." *Phys. Rev. Lett.*, **91**:241803, 2003.

[Aga11] G. Agakishiev et al. "Identified hadron compositions in p+p and Au+Au collisions at high transverse momenta at $\sqrt{s_{NN}}$ = 200 GeV." 2011. * Temporary entry *.

[AGI83] Bo Andersson, G. Gustafson, G. Ingelman, and T. Sjostrand. "Parton Fragmentation and String Dynamics." *Phys. Rept.*, **97**:31–145, 1983.

[Ago03] S. Agostinelli et al. "GEANT4: A simulation toolkit." *Nucl. Instrum. Meth.*, **A506**:250–303, 2003.

[AKK05] S. Albino, B. A. Kniehl, and G. Kramer. "Fragmentation functions for light charged hadrons with complete quark flavour separation." *Nucl. Phys.*, **B725**:181–206, 2005.

[al79] D. Antreasyan et al. *Phys. Rev. D*, **19**, 1979.

[al02] K. Adcox et al. *Phys. Rev. Lett.*, **88**:192303, 2002.

[al04a] J. Adams et al. *Phys. Rev. Lett.*, **92**:112301, 2004.

[al04b] J. Adams et al. *Phys. Rev. Lett.*, **92**:052302, 2004.

[al04c] J. Castilllo et al. *J. Phys. G*, **30**:S1207, 2004.

[al05] J. Adams et al. "Phi meson production in Au+Au and p+p collisions at 200 GeV." *Phys. Lett. B*, **612**:181–189, 2005.

[al08] Yichun Xu et al. "Improvement of resonance reconstruction with time-of-flight detector at STAR experiment." *Nuclear Instruments and Methods in Physics Research A*, **596**:186, 2008.

[All03] C. E. Allgower et al. "The STAR endcap electromagnetic calorimeter." *Nucl. Instrum. Meth.*, **A499**:740–750, 2003.

[All06] John Allison et al. "Geant4 developments and applications." *IEEE Trans. Nucl. Sci.*, **53**:270, 2006.

[ALQ00] W. M. Alberico, A. Lavagno, and P. Quarati. "Non-extensive statistics, fluctuations and correlations in high energy nuclear collisions." *Eur. Phys. J.*, **C12**:499–506, 2000.

[Ams08] C. Amsler et al. "Review of particle physics." *Phys. Lett.*, **B667**:1, 2008.

[And03a] M. Anderson et al. "A readout system for the STAR time projection chamber." *Nucl. Instrum. Meth.*, **A499**:679–691, 2003.

[And03b] M. Anderson et al. "The STAR time projection chamber: A unique tool for studying high multiplicity events at RHIC." *Nucl. Instrum. Meth.*, **A499**:659–678, 2003.

[Ars03] I. Arsene et al. "Transverse momentum spectra in Au + Au and d + Au collisions at s(NN)**(1/2) = 200-GeV and the pseudorapidity dependence of high p(T) suppression." *Phys. Rev. Lett.*, **91**:072305, 2003.

[Ars07] I. Arsene et al. "Production of Mesons and Baryons at High Rapidity and High Pt in Proton-Proton Collisions at sqrt(s) = 200 GeV." *Phys. Rev. Lett.*, **98**:252001, 2007.

[Ash88] J. Ashman et al. "A measurement of the spin asymmetry and determination of the structure function g(1) in deep inelastic muon proton scattering." *Phys. Lett.*, **B206**:364, 1988.

[Bac03] B. B. Back et al. "Centrality dependence of charged hadron transverse momentum spectra in d + Au collisions at s(NN)**(1/2) = 200-GeV." *Phys. Rev. Lett.*, **91**:072302, 2003.

[Bar04] Olga Barannikova. "Probing collision dynamics at RHIC." 2004.

[Bas09] Steven D. Bass. "The proton spin puzzle: where are we today ?" *Mod. Phys. Lett.*, **A24**:1087–1101, 2009.

[Bed03] M. Beddo et al. "The STAR barrel electromagnetic calorimeter." *Nucl. Instrum. Meth.*, **A499**:725–739, 2003.

[Bic06] H. Bichsel. "A method to improve tracking and particle identification in TPCs and silicon detectors." *Nucl. Instrum. Meth.*, **A562**:154–197, 2006.

[Bjo83] J. D. Bjorken. *Phys. Rev. D*, **27**:140, 1983.

[BKK]

[BRB09] Wojciech Broniowski, Maciej Rybczynski, and Piotr Bozek. "GLISSANDO: GLauber Initial-State Simulation AND mOre." *Comput. Phys. Commun.*, **180**:69–83, 2009.

[col] STAR collaboration. "proposal for alarge area time of flight system for STAR.".

[CPR02] T. M. Cormier, A. I. Pavlinov, M. V. Rykov, V. L. Rykov, and K. E. Shestermanov. "STAR Barrel Electromagnetic Calorimeter absolute calibration using 'minimum ionizing particles' from collisions at RHIC." *Nucl. Instrum. Meth.*, **A483**:734–746, 2002.

[CTE]

[Das09] Debasish Das. "Recent results from STAR experiment in Au+Au collisions at $\sqrt{s_{NN}} = 9.2$ GeV." 2009.

[DBS07] Bhaskar De, S. Bhattacharyya, Goutam Sau, and S. K. Biswas. "Non-extensive thermodynamics, heavy ion collisions and particle production at RHIC energies." *Int. J. Mod. Phys.*, **E16**:1687–1700, 2007.

[DES04] X. Dong, S. Esumi, P. Sorensen, N. Xu, and Z. Xu. "Resonance decay effects on anisotropy parameters." *Phys. Lett.*, **B597**:328–332, 2004.

[Don] Xin Dong. "Single Electron Transverse Momentum and Azimuthal Anisotropy Distributions: Charm Hadron Production at RHIC.".

[Don06] Xin Dong. "The time-Of-flight detector for RHIC / STAR and the related physics." *AIP Conf. Proc.*, **865**:332–337, 2006.

[DOP02] H. J. Drescher, S. Ostapchenko, T. Pierog, and K. Werner. "Initial condition for QGP evolution from NEXUS." *Phys. Rev.*, **C65**:054902, 2002.

[Fac08] P. Fachini. "Production at High p_T in Central Au+Au and $p + p$ collisions at $\sqrt{s_{NN}} = 200$ GeV in STAR." *J. Phys.*, **G35**:104063, 2008.

[FG72] Harald Fritzsch and Murray Gell-Mann. "Current algebra: Quarks and what else?" *eConf*, **C720906V2**:135–165, 1972.

[FMN03] R. J. Fries, Berndt Muller, C. Nonaka, and S. A. Bass. "Hadron production in heavy ion collisions: Fragmentation and recombination from a dense parton phase." *Phys. Rev.*, **C68**:044902, 2003.

[FP00] E. Laermann F. Karsch and A. Peikert. *Phys. Lett. B*, **478**:447, 2000.

[FR01] A. Keranen E. Suhonen F. Becattini, J. Cleymans and K. Redlich. "Features of particle multiplicities and strangeness production in central heavy ion collisions between 1.7A and 158 A GeV/c." *Phys. Rev. C*, **64**:024901, 2001.

[FSS07] Daniel de Florian, Rodolfo Sassot, and Marco Stratmann Stratmann. "Global analysis of fragmentation functions for pions and kaons and their uncertainties." *Phys. Rev.*, **D75**:114010, 2007.

[GK04] V. Greco and C. M. Ko. "Effect of resonance decays on hadron elliptic flows." *Phys. Rev.*, **C70**:024901, 2004.

[GRV90] M. Gluck, E. Reya, and A. Vogt. "Radiatively generated parton distributions for high-energy collisions." *Z. Phys.*, **C48**:471–482, 1990.

[GRV92] M. Gluck, E. Reya, and A. Vogt. "Parton distributions for high-energy collisions." *Z. Phys.*, **C53**:127–134, 1992.

[GRV98] M. Gluck, E. Reya, and A. Vogt. "Dynamical parton distributions revisited." *Eur. Phys. J.*, **C5**:461–470, 1998.

[Gup98] R. Gupta. "Introduction to Lattice QCD." 1998.

[Hei] Mark T. Heinz. "Neutral strange particle production in p+p collisions at sqrts=200 GeV and pentaquark searches with STAR at RHIC.".

[HLO03] M. Harrison, T. Ludlam, and S. Ozaki. "RHIC project overview." *Nucl. Instrum. Meth.*, **A499**:235–244, 2003.

[HY04] Rudolph C. Hwa and C. B. Yang. "Recombination of shower partons at high p(T) in heavy-ion collisions." *Phys. Rev.*, **C70**:024905, 2004.

[JA04] et al. J.Adam. "Multistrange Baryon Production in Au-Au Collisions at sqrtsNN = 130 GeV." *Phys. Rev. L*, **92**:182301, 2004.

[Kar02a] Frithjof Karsch. "Lattice QCD at high temperature and density." *Lect. Notes Phys.*, **583**:209–249, 2002.

[Kar02b] Frithjof Karsch. "Lattice results on QCD thermodynamics." *Nucl. Phys.*, **A698**:199–208, 2002.

[KH] P.F. Kolb and U. Heinz. "Hydrodynamic description of ultrarelativistic heavy-ion collisions." SUNY-NTG-03/06.

[KKP]

[KKP01] Bernd A. Kniehl, G. Kramer, and B. Potter. "Testing the universality of fragmentation functions." *Nucl. Phys.*, **B597**:337–369, 2001.

[Kre00] S. Kretzer. "Fragmentation functions from flavour-inclusive and flavour-tagged e+ e- annihilations." *Phys. Rev.*, **D62**:054001, 2000.

[LF08a] W. Liu and R. J Fries. "Elliptic Flow of Rare High-Momentum Probes in Nuclear Collisions." 2008.

[LF08b] W. Liu and R. J Fries. "Probing Nuclear Matter with Jet Conversions." *Phys. Rev.*, **C77**:054902, 2008.

[LK02] Zi-wei Lin and C. M. Ko. "Flavor ordering of elliptic flows at high transverse momentum." *Phys. Rev. Lett.*, **89**:202302, 2002.

[LKZ07] W. Liu, C. M. Ko, and B. W. Zhang. "Jet conversions in a quark-gluon plasma." *Phys. Rev.*, **C75**:051901, 2007.

[Llo05] W. J. Llope. "The large-area time-of-flight upgrade for STAR." *Nucl. Instrum. Meth.*, **B241**:306–310, 2005.

[Lon] Hui Long. "Midrapidity lambda and antilambda production in Au+Au collisions at the Relativistic Heavy Ion Collider." UMI-30-63922.

[Mik] Xin-Nian Wang Ben-Wei Zhang Miklos Gyulassy, Ivan Vitev. "Jet Quenching and Radiative Energy Loss in Dense Nuclear Matter.".

[MMS08] Ananta P. Mishra, Ranjita K. Mohapatra, P. S. Saumia, and Ajit M. Srivastava. "Super-horizon fluctuations and acoustic oscillations in relativistic heavy-ion collisions." *Phys. Rev.*, **C77**:064902, 2008.

[MV03] Denes Molnar and Sergei A. Voloshin. "Elliptic flow at large transverse momenta from quark coalescence." *Phys. Rev. Lett.*, **91**:092301, 2003.

[PS99] I. Heppe P. Braun-Munzinger and J. Stachel. "Chemical Equilibration in Pb+Pb at the SPS." *Phys. Lett. B*, **465**:15, 1999.

[Rua05] Li-juan Ruan. "Pion, kaon, proton and antiproton spectra in d + Au and p + p collisions at s(NN)**(1/2) = 200-GeV at the Relativistic Heavy Ion Collider." 2005.

[Rua08] Lijuan Ruan. "Prototype Performance of Novel Muon Telescope Detector at STAR." 2008.

[Rua09] L. Ruan et al. "Perspectives of a Midrapidity Dimuon Program at RHIC: A Novel and Compact Muon Telescope Detector." *J. Phys.*, **G36**:095001, 2009.

[Sha06a] M. Shao et al. "Extensive particle identification with TPC and TOF at the STAR experiment." *Nucl. Instrum. Meth.*, **A558**:419–429, 2006.

[Sha06b] M. Shao et al. "Extensive particle identification with TPC and TOF at the STAR experiment." *Nucl. Instrum. Meth.*, **A558**:419–429, 2006.

[Sha07] A. Shabetai. "The HFT, a Heavy Flavor Tracker for STAR." *Eur. Phys. J.*, **C49**:169–175, 2007.

[Sim08] F. Simon et al. "The Forward GEM Tracker of STAR at RHIC." 2008.

[Sor] P.R. Sorensen. "Kaon and Lambda Production at Intermediate p_T.".

[SS05] T. Sjostrand and P. Z. Skands. "Transverse-momentum-ordered showers and interleaved multiple interactions." *Eur. Phys. J.*, **C39**:129–154, 2005.

[SSH93] Ekkard Schnedermann, Josef Sollfrank, and Ulrich W. Heinz. "Thermal phenomenology of hadrons from 200-A/GeV S+S collisions." *Phys. Rev.*, **C48**:2462–2475, 1993.

[STA]

[Sto04] R. Stock. *J. Phys. G*, **30**:S633, 2004.

[Sun08] Y. J. Sun et al. "New Prototype Multi-gap Resistive Plate Chambers with Long Strips." *Nucl. Instrum. Meth.*, **A593**:307–313, 2008.

[SW08] Sebastian Sapeta and Urs Achim Wiedemann. "Jet hadrochemistry as a characteristics of jet quenching." *Eur. Phys. J.*, **C55**:293–302, 2008.

[Tan09] Zebo Tang et al. "Spectra and radial flow at RHIC with Tsallis statistics in a Blast-Wave description." *Phys. Rev.*, **C79**:051901, 2009.

[Van06] G. Van Buren et al. "Correcting for distortions due to ionization in the STAR TPC." *Nucl. Instrum. Meth.*, **A566**:22–25, 2006.

[Wan97] Xin-Nian Wang. "pQCD based approach to parton production and equilibration in high-energy nuclear collisions." *Phys. Rept.*, **280**:287–371, 1997.

[Wan98] Xin-Nian Wang. "Effect of jet quenching on high p_T hadron spectra in high-energy nuclear collisions." *Phys. Rev.*, **C58**:2321, 1998.

[Wan04] Fuqiang Wang. "Measurement of jet modification at RHIC." *J. Phys.*, **G30**:S1299–S1304, 2004.

[WW09] Grzegorz Wilk and Zbigniew Wlodarczyk. "Power laws in elementary and heavy-ion collisions: A Story of fluctuations and nonextensivity?" *Eur. Phys. J.*, **A40**:299–312, 2009.

[Xu] Yichun Xu. "Measurements of neutral and charged kaon production at high pT up to 15 GeV/c at STAR.".

[Xu08] Yi-chun Xu et al. "Calibration of ionization energy loss at relativistic rise with STAR Time Projection Chamber." 2008.

[Xu09] Yichun Xu. "Identified hadron production at high transverse momenta in p+p collisions at sqrt(NN) = 200 GeV in STAR." *Eur. Phys. J.*, **C62**:187–190, 2009.

[Xu10] Yichun Xu. "Identified Hadrons and Jet Chemistry for p+p and Au+Au Collisions at RHIC." *J.Phys.G*, **G37**:094059, 2010.

Acknowledgements

This thesis reminds me many people who introduced me into this field and gave me encouragement and valuable help. No their help and support, no this thesis.

Firstly, I would thank Prof. Ziping Zhang for guiding me into high energy physics field, which I had never touched when I began my graduated study. I also appreciate Prof. Hongfang Chen for her support and many constructive suggestions which corrected my faults in time. She also show me an example as a religious scientist and encourage me to walk further in the scientific way. I would like to thank Dr. Timothy Hallman and Prof. Zhangbu Xu for offering the opportunity to work at BNL, the wonderful place for relativistic heavy-ion physics research. I am grateful to my co-adviser, Zhangbu Xu, for guiding me all the analysis in detail throughout the thesis and patient instruction of physics research. I am deeply impressed by his enormous physics knowledge, enthusiasm on the research and numerous exotic ideas.

My special thanks goes to Prof. Ming Shao who instructed me first analysis in simulation. My special thanks also goes to Dr. Xin Dong for his guidance on data analysis. I would like to express my gratitude to Lijuan Ruan and Shengli Huang for their help on my study and living when I was in BNL. I also would thank my classmate Zebo Tang for his help on abundant helpful discussion and living and encouragements. I also thank Dr. Jing Liu, Dr. Jianhang Zhou and Dr. Hua Pei for their help.

I appreciate many assistances from spectra working group and the STAR group at BNL, especially Dr. Nu Xu, Dr. Bedanga Mohanty, Dr. Olga Barannikova, Dr. Jun Takahashi, Dr. Pawan Netrakanti, Dr. Gene Van Buren, Dr. Aihong Tang and Cora Feliciano. I also appreciate many assistances from the High Energy Physics Group at USTC, especially Prof. Zizong Xu, Prof. Xiaolian Wang, Prof. Zhengguo Zhao, Prof. Qun Wang, Prof. Cheng Li, Mr. Hui Zeng, Dr. Yongjie Sun, Dr. Yifei Zhang, Dr. Yan'e Zhao, Mr. Yi Zhou.

I also would like to thank all my friends for their continuous supports and encour-

agements. I would like to thank all the physicists who discussed with me face-to-face or through email. With them, my life becomes more colorful and meaningful.

Finally, I would like to dedicate my gratitude to my family. I'll never forget tens of years of unceasing self-giving sacrifices from my parents and continuous support and understanding from my sister and brother.

APPENDIX B

Presentations and Publication List

Presentations

- *High p_T particle identification in p+p collisions*

  2007 Annual Meeting of the Division of Nuclear Physics of the American Physical Society, Oct. 12, 2007-Nuewport News, Virginia, USA.

- *Re-calibration of dE/dx and identified particle spectra at high-p_T in p+p collisions at 200 GeV*

  RHIC and AGS Annual User's Meeting, May 27th, 2008 - Brookhaven National Laboratory, Upton, 11973, USA.

- *Measurements of neutral and charged kaon production at high p_T up to 15 GeV/c at STAR*

  21th International Conference on Ultra-relativistic Nucleus-Nucleus Collisions (Quark Matter 2009), March 30-April 4, Knoxville, TN, USA.

- *Significant change of the identified hadron compositions relevant to jet chemistry from p+p to Au+Au collisions at RHIC*

  International conference on Strangeness in Quark Matter 2009 (SQM09), Sep. 27 - Oct. 2, 2009, Rio de Janeiro, Brazil.

- *High-p_T identified particle spectra in p+p collisions at 200 GeV*

  Hot Quarks 2008, August 18-23, 2008, Aspen Lodge at Estes Park, Colorado, USA

Publication List

- *Measurements of neutral and charged kaon production at high p_T up to 15-GeV/c at STAR.*

  Yichun Xu (for STAR Collaboration), Nucl. Phys. A830: 701c-704c, 2009.

- *Identified hadron production at high transverse momenta in p+p collisions at $\sqrt{S_{NN}}$= 200 GeV in STAR*

  Yichun Xu (for STAR Collaboration), Eur. Phys. J. C (2009) 62: 187 - 190.

- *Improvement of resonance reconstruction with time-of-flight detector at STAR experiment*

  Yichun Xu, Xin Dong, Ziping Zhang, Zebo Tang and Ming Shao, Nucl. Instr. & Meth. **A596** (2008) 186-189.

- *Simulation Study on the Splitting Effects of Transverse Mass Spectra in p+p Collisions at $\sqrt{s_{NN}}$ =200GeV using PYTHIA*

  Yichun Xu, Ming Shao and Ziping Zhang, Chinese Physics C (High Energy Physics and Nuclear Physics), 2007 31 (06): 538—542

- *Spectra and radial flow at RHIC with Tsallis statistics in a Blast-Wave description*

  Z. Tang, Y. Xu, L. Ruan, G. van Buren, F. Wang and Z. Xu, Phys. Rev. **C79**, 051901 (2009) [arXiv:0812.1609 [nucl-ex]].

- *Calibration of ionization energy loss at relativistic rise with STAR Time Projection Chamber*

  Yichun Xu, Olga Barannikova, Hans Bichsel, Xin Dong, Patricia Fachini, Yuri Fisyak, Adam Kocolosky, Bedanga Mohanty, Pawan Netrakanti, Lijuan Ruan, Maria Cristina Suarez, Zebo Tang, Gene van Buren, Zhangbu Xu, arXiv:0807.4304 (submitted to Nucl. Instr. & Meth.)

- *Upgrade of the calibration procedure for a STAR time-of-flight detector with new electronics*

Ming Shao, Xin Dong, Zebo Tang, Yichun Xu, Min Huang, Cheng Li, Hongfang Chen, Yan Lv and Yifei Zhang, Meas. Sci. Technol. **20** (2009) 025102

- *Beam-Energy and System-Size Dependence of Dynamical Net Charge Fluctuations* B.I. Abelev et al., (STAR Collaboration), Phys.Rev.**C79**:024906 (2009), e-Print: arXiv:0807.3269

- *Indications of Conical Emission of Charged Hadrons at RHIC* B.I. Abelev et al., (STAR Collaboration), Phys.Rev.Lett.**102**:052302 (2009), e-Print: arXiv:0805.0622

- *Neutral Pion Production in Au+Au Collisions at s(NN)**(1/2) = 200-GeV* B.I. Abelev et al., (STAR Collaboration), Phys.Rev.**C80**: 024905,2009. e-Print: arXiv:0907.2721

- *K/pi Fluctuations at Relativistic Energies* B.I. Abelev et al.,(STAR Collaboration), Phys.Rev.Lett.**103**:092301,2009. e-Print: arXiv:0901.1795.

- *Measurement of D* Mesons in Jets from p+p Collisions at s**(1/2) = 200-GeV*, B.I. Abelev et al.(STAR Collaboration) Phys.Rev.**D79**:112006,2009. e-Print: arXiv:0901.0740